



Università degli Studi di Torino

SCUOLA DI SCIENZE DELLA NATURA

Corso di Laurea Magistrale in Fisica

TESI DI LAUREA MAGISTRALE

Study of radiation effects on prototypes of the \bar{P} ANDA Micro Vertex Detector

Candidato:

Ilaria Balossino

Relatore:

Prof.ssa Michela Greco

Co-Relatore:

Dott.ssa Daniela Calvo

Contro-Relatore:

Prof.ssa Maria Pia Bussa

Abstract

PaNDa (AntiProton ANnihilation at DArmstadt) is a fixed target sub-nuclear experiment. It is under construction at the GSI laboratory at Darmstadt, Germany. It will be one of the main projects of FAIR (Facility for Antiproton and Ion Research). The study of the radiation effects on prototypes of the readout architecture part for the Micro Vertex Detector has been performed in this work. In the first part, the experiment is described with its physics aims and with the experimental setup. It is followed by the presentation of the Micro Vertex Detector with its requirements and mechanical setup. Then Single Event Upset effects are described. The subsequent chapter presents the tests on the ToPix and GBLD prototypes together with the SEU rate estimation in the PaNDa environment. At the end, the tests with the prototypes of ToPix 3.0 irradiated with neutrons with a focus on the leakage current circuit are presented. This thesis has been developed in collaboration with the Electronic Laboratory of the INFN, section of Turin. The SEU test has been performed at the SIRAD (Silicon RAdiation Damage) irradiation facility, at the INFN National Laboratory of Legnaro (Padova). The neutron irradiation was performed at the LENA laboratory, Pavia.

Contents

1	PANDA Experiment	4
1.1	Scientific Program	4
1.2	FAIR	7
1.3	Experimental Setup	8
1.3.1	Target Spectrometer	9
1.3.2	Forward Spectrometer	15
2	Micro Vertex Detector	19
2.1	Requirements	19
2.2	Layout	21
2.3	Silicon Sensors	22
2.3.1	Hybrid Pixel Detectors	24
2.3.2	Double-Sided Silicon Microstrip Detector	26
3	Single Event Upset	29
3.1	Particle interaction with the matter	30
4	Heavy Ion Irradiation	41
4.1	SIRAD Facility	41
4.2	Prototypes	45
4.2.1	ToPix 3.0	45
4.2.2	ToPix 2.0	48
4.2.3	GBLD v4	48
4.2.4	GBLD v5	50
4.2.5	SEU tolerance architecture	51
4.3	Data Acquisition	53
4.3.1	Dosimetry	54
4.3.2	ToPix	54
4.3.3	GBLD	57
4.3.4	SRIM (Stopping and Range of Ions in Materials)	58
4.4	Analysis	60

<i>CONTENTS</i>	3
-----------------	---

4.4.1 Energy deposition	60
4.4.2 Dosimetry	60
4.4.3 SEU	61
4.4.4 Conclusions	72
4.5 SEU rate in the \bar{P} ANDA enviroment	74
4.5.1 SEU by hadrons	74
4.5.2 SEU by leptons	78
5 Neutron Irradiation	80
5.1 Radiation Damage in Silicon	80
5.1.1 Basic processes	80
5.1.2 NIEL hypotesis	80
5.1.3 Effects on detector's properties	81
5.2 Displacement Damage Analysis	82
5.2.1 Baseline calibration	83
5.2.2 Leakage currents	88
5.3 Conclusions	89
6 Conclusions	90

Chapter 1

‐PANDA Experiment

The ‐PANDA [1][2], Antiprotons Annihilation at Darmstadt, experiment is one of the projects of the Facility for Antiproton and Ion Research, FAIR [3], at GSI Gesellschaft fur Schwerionenforschung, the Heavy Ion Research Lab. FAIR is already under construction at GSI. The existing complex will be used as injector for FAIR. This facility will deliver primary proton and ion beams and secondary beams of antiprotons or radioactive ions, all with high energy, intensity and quality. The ‐PANDA Collaboration, with 450 scientists from 17 countries, aims to make a significant progress in the understanding of hadron structure and of Quantum ChromoDynamics spectrum, in the energy range between the non perturbative and perturbative regime. This improvement will be done studying antiproton-proton annihilation and reaction of antiprotons with nucleons in fixed heavy nuclear targets. Research in this facility allows the experiment to be an unique tool to improve both statistics and precision of existing data and to further explore the physics case.

1.1 Scientific Program

Quantum ChromoDynamics is the theory of the strong interaction describing quarks interacting with each other by gluons exchange.

To understand it well, at short distance scales the perturbation theory is applied to describe the behavior of quarks and gluons in close analogy with the Quantum Electron-Dynamics.

In the energy regime of interest for this experiment, the distance among quarks becomes comparable to the size of the nucleons. Under this condition, the self-interactions of gluons start to be significant. As a consequence, quarks have never been observed as free particles and are confined within hadrons.

To understand the nature of the strong interaction and of hadronic matter these are the phenomena to study:

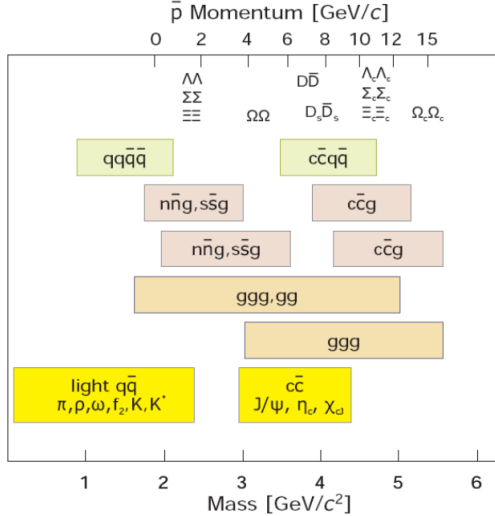


Figure 1.1: Mass range of hadrons accessible to $\bar{\text{P}}\text{ANDA}$

- the confinement of quarks;
- the existence of hadronic systems consisting only of gluons or of bound systems of quark-antiquark pairs and gluons;
- the origin of the mass of strongly interacting particles;
- the breaking of chiral symmetry.

In this experiment, through antiproton-proton annihilation, particles with gluonic degrees of freedom as well as particle-antiparticle pairs are copiously produced. Besides, a beam of unprecedented intensity and quality in the energy range 1 – 15 GeV will allow spectroscopic studies with high statistics and precision and it will be an excellent tool to address fundamental questions.

In the following sections there will be a brief description of the $\bar{\text{P}}\text{ANDA}$ physics program [4].

Charmonium Spectroscopy The system of charm and anti-charm quark, or charmonium system, offers a lot of advantages for understanding the strong interaction and quarkonia. Indeed, the low density of states and their narrowness reduces mixing among them as long as they are below the corresponding open charm threshold at 3868 MeV. With these high intensity and quality antiproton beams the charmonium states of all quantum numbers could be formed directly. These states will be studied with a scan of their shapeline. In this way the measurements of masses, widths, decay branches ratio will allow to collect lots of information on the quark confining potential.

Gluonic Excitations In the QCD spectrum we find both quarks and gluons. These last can mediate the strong force between quarks and can also theoretically act as principal components of new types of hadrons: the “Gluonic Hadrons”.

They are divided into two categories:

- *glueballs*, excited states of glue;
- *hybrids*, resonances consisting of a quark, an antiquark and an excited glue.

Antiprotons-proton annihilation provide a favourable environment where to look for gluonic hadrons. The additional degrees of freedom carried by gluons allow glueballs and hybrids to have spin exotic quantum numbers that are forbidden for normal mesons and other fermion-antifermion systems. Exotic quantum numbers are the easiest way to distinguish gluonic hadrons from $q\bar{q}$ states, but even non-exotic glueballs and hybrids can be identified by measuring an overpopulation of the experimental meson spectrum and by comparing their properties. Since the properties of glueballs and hybrids are determined by the long distance QCD features, their study will yield fundamental insights into the structure of QCD vacuum.

Hadrons in Nuclear Matter The study of hadrons in hadronic matter aims to understand the origin of hadron masses in the context of spontaneous chiral symmetry breaking and its partial restoration in an hadronic environment. Particular emphasis is placed on mesons with open and hidden charm, well obtained with the high intensity antiproton beam up to 15 GeV. As masses of charmonia are dominated by the large mass of the charm quark pair, only little sensitivity to changes in the quark condensate is expected for charmonium states. Consequently, the in-medium mass of these states would be affected primarily by a modification of the gluon condensate. Investigating the interaction of $c\bar{c}$ mesons with nucleons and nuclei is therefore a way to explore fundamental aspects of gluon dynamics in QCD.

Open Charm Spectroscopy The study of the D mesons have a significant part in the charmed meson spectroscopy program thanks to the well defined production kinematics. Indeed, in the production process, for example, there are no asymmetries expected, the D meson offers to know the quantum number of the other one (\bar{D}) produced in a charge symmetric environment and flavour mixing and CP violation can be searched for in analogy to methods in the B -system. All these studies in this experiment are expected to be done thanks to the full luminosity and the available antiproton momenta larger than 6.4 GeV/c.

Hypernuclear Physics Hypernuclei are systems in which one or more nucleons are replaced by hyperons: in the nucleus is introduced a new quantum number, *strangeness*

(s), instead of light quarks (u,d).

In this experiment the beam allows the production of hypernuclei and double hypernuclei, which are the basis to study the nuclear structure and the forces between hyperons and nucleons.

Electromagnetic Processes Electromagnetic processes like the Deep Virtual Compton Scattering or the process $p\bar{p} \rightarrow e^+e^-$ make $\bar{\text{P}}\text{ANDA}$ able to investigate the structure of the nucleon and the determination of the electromagnetic form factors of the proton in the timelike region over an extended q^2 region. Moreover the Drell Yan production of muons will give access to the transverse nucleon structure.

1.2 FAIR

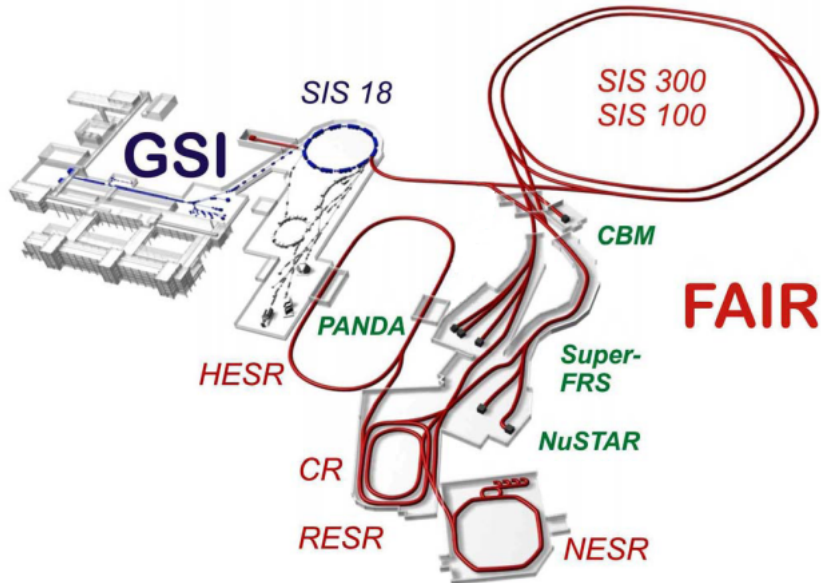


Figure 1.2: Layout of FAIR [5]

FAIR will extend the GSI structure (Fig.1.2, red lines). It will host two main experiments with antiprotons: FLAIR, Facility for Low Energy Antiproton and Ion Research, and $\bar{\text{P}}\text{ANDA}$ with high energetic antiprotons. Both these experiments will have a storage ring, NESR and HESR for low and high momentum domain, respectively.

The protons will be accelerated at 70 MeV by the Linear Accelerator LINAC. The synchrotron SIS18 will accelerate $5 \cdot 10^2$ protons per machine cycle, with a repetition rate of 4 Hz, up to 2 GeV. Subsequently, in the SIS100, $4 \cdot 10^{13}$ protons will be accumulated in bunches of 25 ns time width, with an energy of 29 GeV. Then the protons will collide with the nickel target producing antiprotons. This cycle is repeated every 10 s in order to have 10^7 antiprotons produced every second. After the production, the antiprotons will

be separated from the other particles with a pulsed magnet. Then they will be collected in the Collector Ring with a beam momentum of 3.8 GeV/c and a momentum spread of $\sigma_p/p = 3 \cdot 10^{-3}$. Finally the antiproton beam will be transferred at the High Energy Storage Ring (Fig. 1.3) to the $\bar{\text{P}}\text{ANDA}$ experiment situated in the straight section of the structure. The antiprotons in this ring will be accelerated or decelerated in the momentum range from 1.5 GeV/c to 15 GeV/c using Radio Frequency cavities.

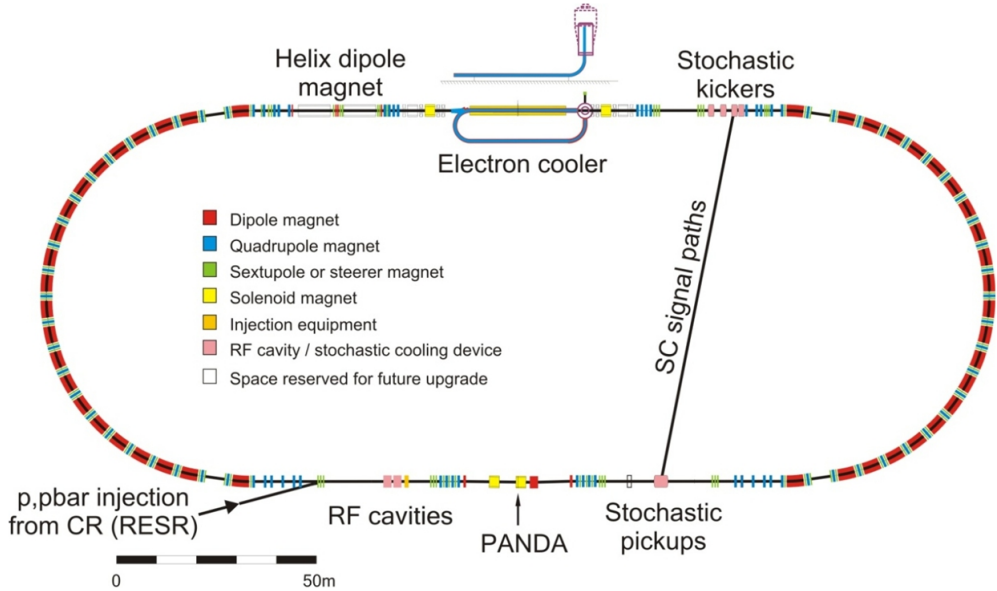


Figure 1.3: Layout of HESR [5]

There are two different operating modes:

- *High Luminosity*: designed peak luminosity up to $2 \cdot 10^{32} \text{ cm}^{-2}\text{s}^{-1}$ and momentum resolution of $\sigma_p/p = 10^{-4}$. Full momentum, $10^{11} \bar{p}$ beam.
- *High Resolution*: momentum resolution of $\sigma_p/p = 10^{-5}$, designed peak luminosity up to $10^{31} \text{ cm}^{-2} \text{ s}^{-1}$, momentum range from 1.5 to 9 GeV/c, $10^{10} \bar{p}$ beam.

Powerful electron and stochastic cooling systems are necessary to meet the cited experimental requirements.

1.3 Experimental Setup

The main objectives of $\bar{\text{P}}\text{ANDA}$ are:

- full angular coverage and good angular resolution for both charged and neutral particles ($\sim 4\pi$);
- particle identification in a large range of particles (γ, e, μ, K, p) and energies (from few MeV/c up to 15 GeV/c);

- high resolution for tracking (moment resolution of $\sim 1\%$ and spatial resolution of some tens of μm);
- high rate capability ($2 \cdot 10^7 \bar{p}p$ interactions/s);
- triggerless readout.

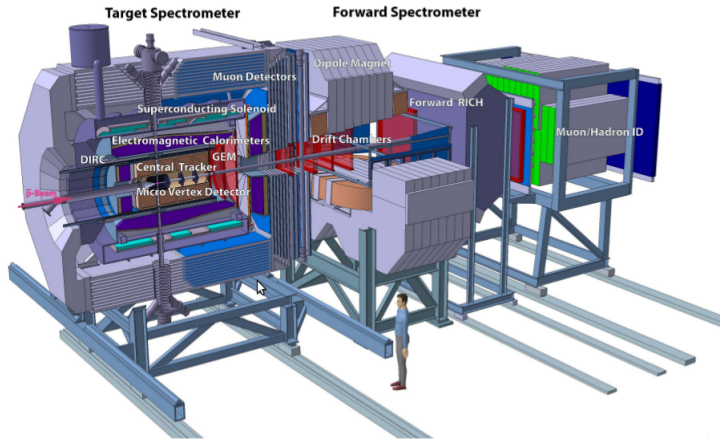


Figure 1.4: Layout of $\bar{\text{P}}\text{ANDA}$ [5]

$\bar{\text{P}}\text{ANDA}$, as a fixed target experiment, consists of two spectrometers: the *Target Spectrometer* surrounds the interaction region with a superconducting solenoid and the *Forward Spectrometer* with a dipole, for small angle tracks (Fig. 1.4). There will be the possibility to exchange individual parts in order to make hypernuclear experiments. The detector structure is composed by modular subsystems: tracking detectors (MVD, STT, GEM), electromagnetic calorimeters (EMC), a muon system, Cherenkov detectors (DIRC, RICH) and a Time-of-Flight system (TOF).

1.3.1 Target Spectrometer

It will surround the interaction point in a highly homogeneous solenoidal field with a onion shell structure of different detectors (Fig.1.5). The pipes for the injection of the target material will have to cross this spectrometer perpendicularly to the beam pipe. It will detect particles emitted with different laboratory angles :

- greater than 5° and 10° in the vertical and horizontal planes in the forward direction thanks to the forward end cap;
- between 22° and 140° , covered by the barrels;
- between 145° and 170° with the backward end cap.

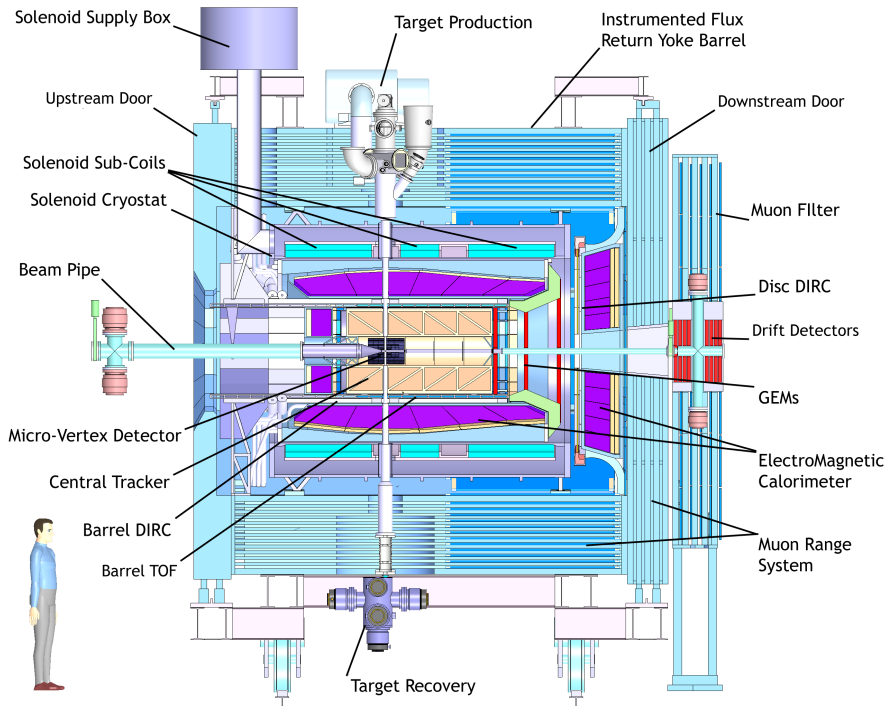


Figure 1.5: Layout of the *Target Spectrometer* [5]

Beam-Target System

This system will include the apparatus for the target production and the vacuum system for the interaction region. The target material will be injected from the top in the target pipe. In here, the vacuum system will be regulated by a pump placed outside this structure. The pipe will have wall thicknesses of $200\ \mu\text{m}$ and an inner diameter close to the interaction point of around 20 mm. To answer to all the physics requests, different types of target are investigated: cluster jet, pellet target and solid target. This is because they exhibit different properties concerning their effect on the beam quality and the definition of the interaction point.

Cluster jet The target production will be made by pressurised cooled gas injected into vacuum. This ejected gas will be immediately condensated and form a narrow supersonic jet of molecule clusters. In this way, the cluster jet target will be provided an homogeneous and adjustable density. It will have a target density of about $1.6 \cdot 10^{15}$ hydrogen atoms per square centimeter. This kind of target will assure constant luminosity during HESR cycle. The gases that can be used are: $H_2, D_2, O_2, N_2, Ne, Ar, Kr, Xe$.

Pellet target It will provide a stream of frozen molecule droplets, which drip with a fixed frequency off from a fine nozzle into vacuum. This kind of target will allow to reach higher target densities ($\sim 10^{16}$) and to have an uncertainty on the reconstruction of the interaction point of $\pm 1\ \text{mm}$. This kind of pellet can be made of N, Ar, D or heavy

noble gases. [6]

Solid target They are foreseen for hypernuclear studies and for antiprotons-nuclear interaction. They could be, for example, made of C, Au, Pb.

Solenoid Magnet

The superconducting coil has a length of 2.8 m and an inner diameter of 0.90 m. It uses a laminated iron yoke for the flux return. This magnet (Fig. 1.6), surrounding the interaction point detectors, will deliver a very homogeneous field of 2T with fluctuations of less than 2%. The magnetic field, in this way, results in a circular transverse motion of charged particles with non zero transverse momentum. Their momentum can be extracted by the determination of the bending radius.

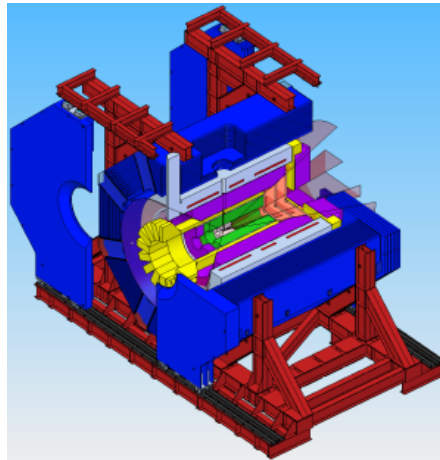


Figure 1.6: View of the *Solenoid Magnet* [6]

Tracking Detector

The tracks of the particles emitted as reaction products from the interaction point will be detected and reconstructed by three different detectors.

MicroVertex Detector This detector is the closest to the interaction point. It is based on silicon pixel and strip detectors for the inner and outer part respectively. It will have a maximum length of 40 cm and a maximum radius of 15 cm and foresees four barrels around the interaction point and six forward disks. This structure is optimised for the detection of secondary vertices from charmed and strange hadrons and for having the maximum acceptance close to the interaction point. It will improve the transverse momentum resolution up to $\sigma_p/p = 2.6\%$.

Straw Tube Tracker It is the second detector from the interaction point to the outside. It is made by aluminised Mylar tubes with a diameter of 10 mm (straw tube). They will be arranged around the MVD, mounted in a hexagonal shape (Fig.1.7). There will be 27 layers for 4636 straws at radial distances between 15 cm and 41.8 cm. The gas that will be used is a mixture of 90% Ar and 10% CO_2 . These straws will be stiffened by operating them at an overpressure of 1 bar which makes them self-supporting. The prototype has a spatial resolution of about $150 \mu m$ and of 1 mm in z direction. [6]

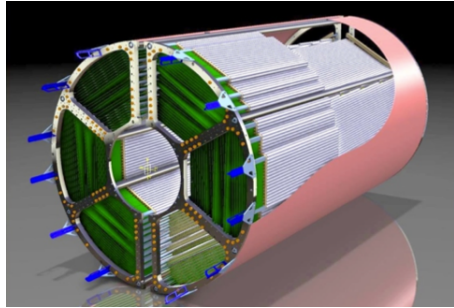


Figure 1.7: Layout of the *STT* detector [5]

Gas Electron Multiplier It will be used to identify the particles emitted at angles below 22° due to the relativistic boost or the small angle of the elastic scattering of $p\bar{p}$. Depending on the length of the central tracker, there will be three or four sequential stations as shown in the Fig.1.8. Each one has a double-sided readout pad plane for the particle track position measurement. [6]

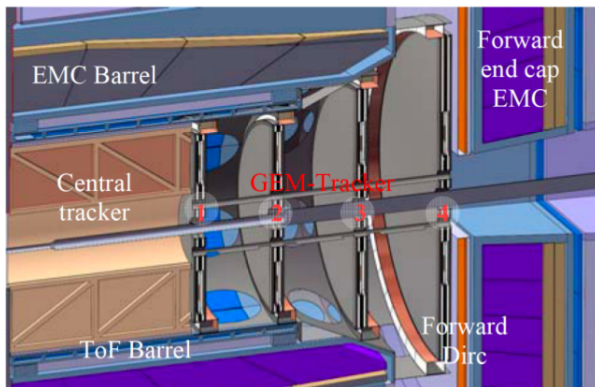


Figure 1.8: Layout of the *GEM* Trackers [6]

Particle Identification

The particle identification is mainly made by the combination of information from many detectors: TOF system, MVD , DIRC, EMC and Muon Detectors.

Time-Of-Flight Stop counter It will give a time signal in order to know the time a charged particle (with velocity β) has used to travel a certain distance, l . The time of flight is then defined as $t_{TOF} = l/\beta c$. This information with the momentum given by $p_{tr} \vec{r} = 0.3B\rho$ can be used to identify the particle mass. It will be composed in the barrel part by 5760 scintillator tiles of $28.5 \times 28.5 \text{ mm}^2$ individually read out by two Silicon Photomultipliers per tile. These tiles are positioned just outside the Barrel DIRC and can be augmented by approximately 1000 tiles in forward direction just in front of the endcap disc DIRC

Detection of Internally Reflected Cherenkov light Charged particles in a medium with index of refraction n , propagating with velocity $\beta c < 1/n$, emit radiation at an angle $\theta = \arccos(1/\beta n)$. This kind of the detector is specific to detect particles with a momentum spectrum between 800 MeV/c and 5 GeV/c. They will be placed in the barrel and in the forward endcap (Fig. 1.9). The first one will detect emitted particles in the angles between 22° and 140° . Fused silica slabs with $n = 1.47$, 1.7 cm thick, will surround the beam line (radial distance of 45 cm - 54 cm). The second one will cover angles between 5° and 22° . The disk, 2 cm thick, 110 cm large will be placed upstream of the forward end cap calorimeter. From both, light will be imaged onto Microchannel Plate Photomultiplier Tubes, insensitive to the magnetic field. In this way the detector is expected to read out two spatial coordinates and the propagation time.

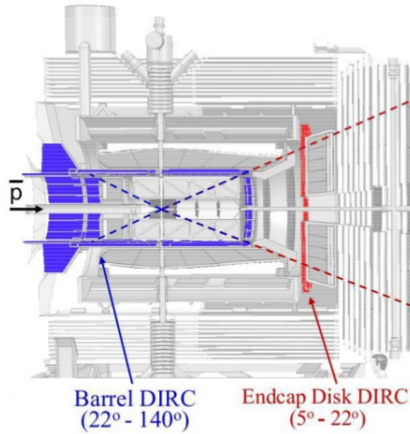


Figure 1.9: Layout of the *DIRC* detector

ElectroMagnetic Calorimeter The scintillator material of the EMC will be composed by a barrel, a forward and a backward end cap around the DIRC (Fig. 1.10). It will have short radiation length and a short Moliere radius. The material chosen is lead tungsten, $PbWO_4$: it will have sufficient energy and time resolution for photon and electron detection, ready for the high count rates and the geometrically compact design. The

crystals will have $22 X_0$ (20 cm long), to achieve an energy resolution below 2% at 1 GeV. The EMC will allow to achieve an e/π ratio of 10^3 for momenta above 0.5 GeV/c.[7]

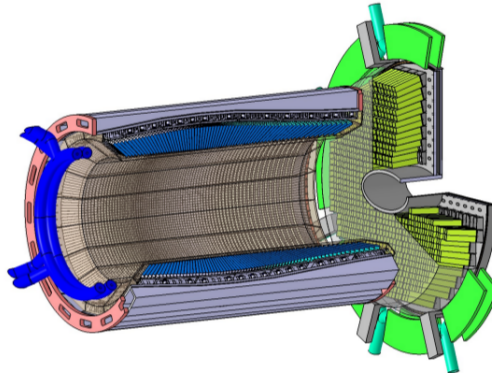


Figure 1.10: Layout of the Barrel *EMC* and the Forward *EMC* [6]

Muon Detector The Muon Detector is in the iron yoke of the spectrometer. It will be built of plastic scintillator counter: 13 sensitive layers, each 3 cm thick (layer "zero" is a double-layer) alternate with 3 cm thick iron absorber layers (first and last iron layers are 6 cm thick). 72 rectangular aluminum Mini Drift Tubes (MDT) are placed between the absorber layers featuring 16 cm wide, 2 cm thick and 2.5 m long. This configuration will be able to distinguish the energy loss processes of muons and pions. This also has the ability to divide the primary muons and the background.

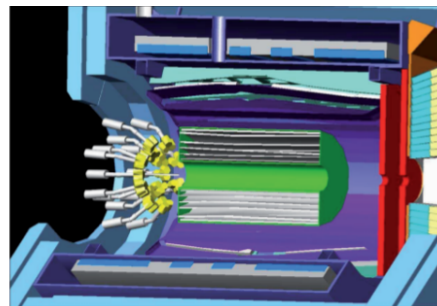


Figure 1.11: Layout of the *Hypernuclear Detector* [8]

Hypernuclear Detector Hypernuclear studies will require additional components: a dedicated target system and a γ detector (Fig. 1.11). In this case the backward end cap calorimeter and the MVD will be removed. The antiprotons at momentum of 3 GeV/c will interact with the new target system producing $\Xi\bar{\Xi}$. The $\bar{\Xi}$ decay provide an easy identification evidence for these processes. The secondary hypernuclear target, which has an active part of silicon strip sensor ($41 \times 0.3 \times 41$ mm 3 in a pitch of 150μ m), is intended to track and stop the produced cascade hyperons and their decay products. The slowing

down of the Ξ proceeds through a sequence of nuclear elastic scattering events, inside the residual nucleus in which the annihilation has occurred, and by energy loss during the passage through an active absorber. If decelerated to rest before decaying, the particle can be captured inside a nucleus, eventually releasing two Λ hyperons and forming a hypernuclei pair. The geometry of the target is essentially determined by the lifetime of the hyperons and their stopping time in solid material.

1.3.2 Forward Spectrometer

It is the downstream part of the detector (Fig. 1.12) analysing the emitted particles below 5° and 10° in vertical and horizontal direction respectively.

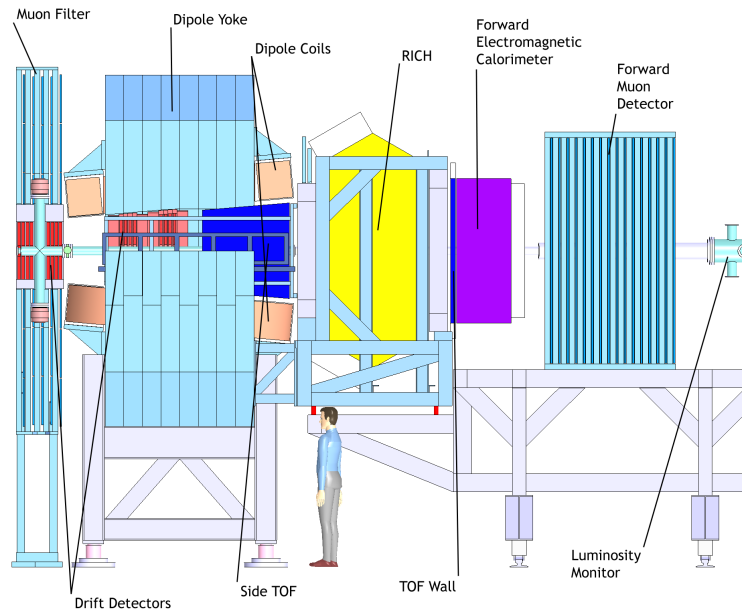


Figure 1.12: Layout of the *Forward Spectrometer*[5]

Dipole Magnet

A 2 Tm dipole magnet with a window frame, a 1 m gap, and more than 2 m aperture will be used for the momentum analysis of charged particles (Fig. 1.13). It will be placed in the space around 3.3 m and 5.8 m downstream the target. The resulting deflection for the antiproton beam at maximum momentum (15 GeV/c) is 2.2° . This will be compensated by other two or three correcting dipole magnets placed around the detection system. The expected momentum resolution for particles of about 3 GeV/c will be $\sigma_p/p = 0.2\%$.

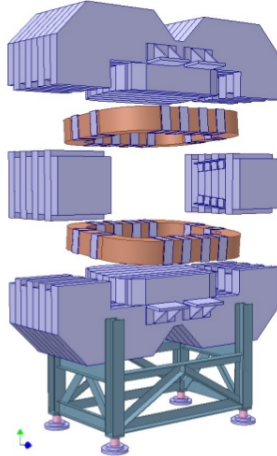


Figure 1.13: View of the *Dipole Magnet* [6]

Tracking Detectors

In order to reconstruct the particle track in the forward region there will be a set of straw detectors: two in front and two behind the dipole magnet and other two inside the magnet gap. The system will be able to track particles both with high or low momenta. Moreover the configuration of this system will allow to separate tracks in order to be able to deal with multi-track events. The expected momentum resolution for 3 GeV/c protons is $\sigma_p/p = 0.2\%$.

Particle Identification

As in the Target Spectrometer there will be a Time of Flight Stop Detector, a RICH, Ring Imaging Cherenkov Counter together with Calorimeter and Muon Detection, in order to identify particles.

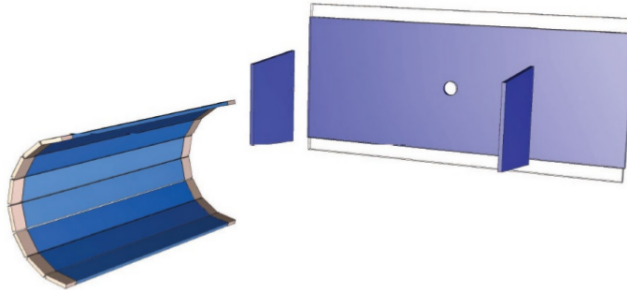


Figure 1.14: Layout of the *TOF* detector in the Target and Forward Spectrometer [6]

Time-Of-Flight It will be placed as a wall at both ends of the Forward Spectrometer (Fig. 1.14). With a time resolution of about $\sigma = 50$ ps , π/K and K/p separation on a

3σ level will be possible up to momenta of 2.8 GeV/c and 4.7 GeV/c respectively.

Ring Imaging Cherenkov Counter It is proposed in order to separate π/K and K/p in the momentum range between 2 and 15 GeV/c. The Aerogel Cherenkov Counters will be composed of two radiators: Silica Aerogel ($n = 1.0304$) and Freon Gas ($n = 1.0013$). In Fig. 1.15 there is a scheme of the detector position.

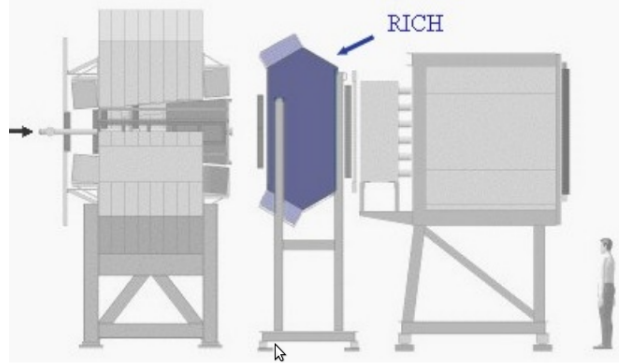


Figure 1.15: Layout of the *RICH* detector

Calorimeter It is composed of a Shashlyk-type calorimeter, for photons and electrons detection with high resolution and efficiency. It will be made of 351 modules of $110 \times 100 \times 680 \text{ mm}^3$ ($20 X_0$). It will be placed at 7.5 m from the target for an active area of about 4 m^2 with a resolution of $4\%/\sqrt{E}$.

Muon Detector It will be placed at 9 m from the interaction point. It will be composed of interleaved absorber layers and rectangular aluminium drift-tubes. It will allow the discrimination of pions from muons, detection of pion decays and energy determination of neutrons and anti-neutrons.

Luminosity Monitor

The luminosity monitor will consist of four planes of High Voltage Monolithic Active Pixel Sensors (HV-MAPS) (Fig. 1.16). It will be located between the forward muon system and the HESR dipole (necessary to redirect the antiproton beam into the direction of HESR straight stretch) and really close to the beam axis. This set up will be placed in order to reconstruct the direction of elastically scattered antiprotons with polar angle between 3 and 8 mrad with respect to the beam axis, and have online information on the instantaneous luminosity.

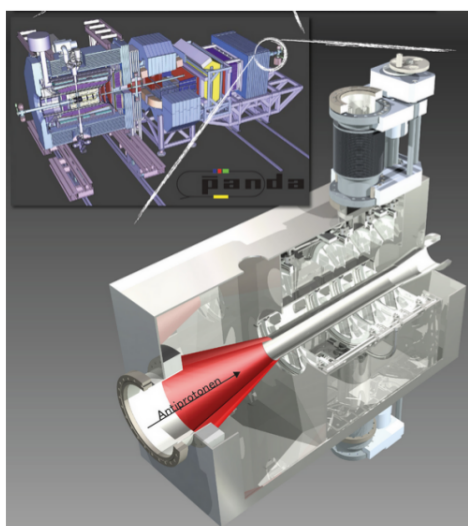


Figure 1.16: Schematic view of the *Luminosity Monitor* [9]

Chapter 2

Micro Vertex Detector

The Micro Vertex is the closest detector to the interaction point. It is located inside the solenoid magnet of the Target Spectrometer and is the first detector of the Central Traking System.

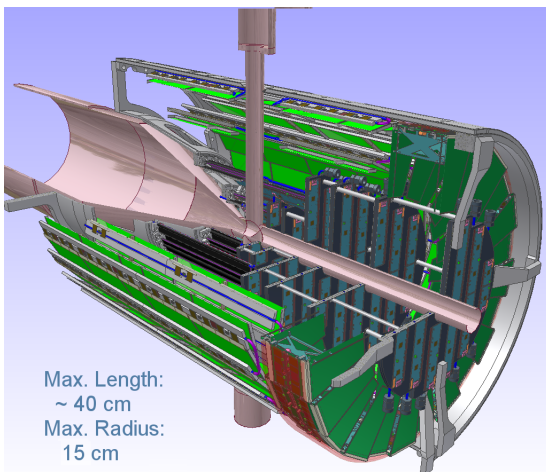


Figure 2.1: MicroVertex Detector [5]

It provides charged particle track point measurements with very high precision in space and time as well as energy loss measurement. The main goal is to measure the first track point of a charged particle as close to the interaction point as possible, which is essential for the reconstruction of decay vertices. It is able to give 3D information of the particle hits, with a spatial resolution less than hundreds of μm , and a hit time resolution better than 20 ns, in order to group hits belonging to the same event. In addition, it can help particle identification.

2.1 Requirements

To answer to the physics program, the MVD has to match some requirements:

- *spatial resolution* It has to be of the same order of magnitude of the decay length of mesons to reconstruct the secondary vertices. It will be better than $100\text{ }\mu\text{m}$ along the beam direction and few tens of μm in $r\phi$ direction;
- *time resolution* Being the system triggerless, the detector has to deal with an estimated rate of $2 \cdot 10^7$ events/s. The time resolution will be around 6.4 ns for 155.5 MHz clock;
- *radiation hardness* Since it is close to the interaction point, all the components need to be radiation hard. For antiproton-proton annihilations at 15 GeV/c, the expected radiation level for 10 years (50% duty cycle) of data taking is about $10^{14}n_{1MeV eq}/\text{cm}^{-2}$.
- *material budget* In order to reduce loss of energy and multiple scattering the design has to be optimized: $1\% X/X_0$ per layer. The expected particle distribution is shown in Fig. 2.2. In the antiproton-proton collisions there is a Lorentz boost of particles in forward direction for high beam momenta. The low momentum particles (from 100 up to 500 MeV/c) are uniformly distributed over the full polar angles and can be more affected by multiple scatterings. At polar angles below 80° there is an enhanced emission of slow recoil protons for the elastic scattering. In antiproton-nucleon reactions the Lorentz forward boost is less distinct and vanishes with increasing atomic number.

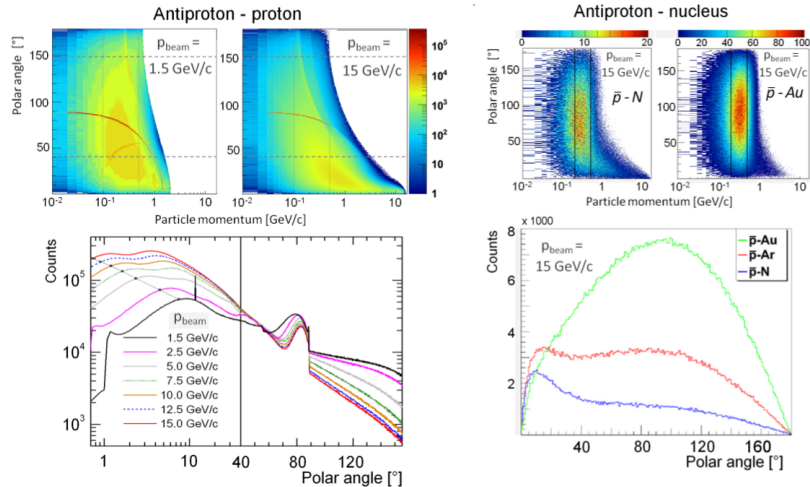


Figure 2.2: Expected particle distribution for both the interactions. Top: Particle distribution with respect to polar angle and particle momentum. Bottom: 1D profile projected onto the polar angle. [5]

- *particle identification* It has to measure the energy lost to contribute to the particle identification up to momentum of 500 MeV/c (for kaons) or to 1 GeV/c (for protons)(see Fig.2.3).

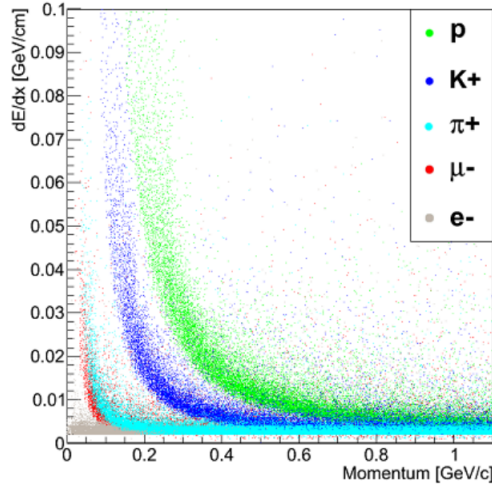


Figure 2.3: Energy loss distribution in the MVD with respect to the momentum. [5]

2.2 Layout

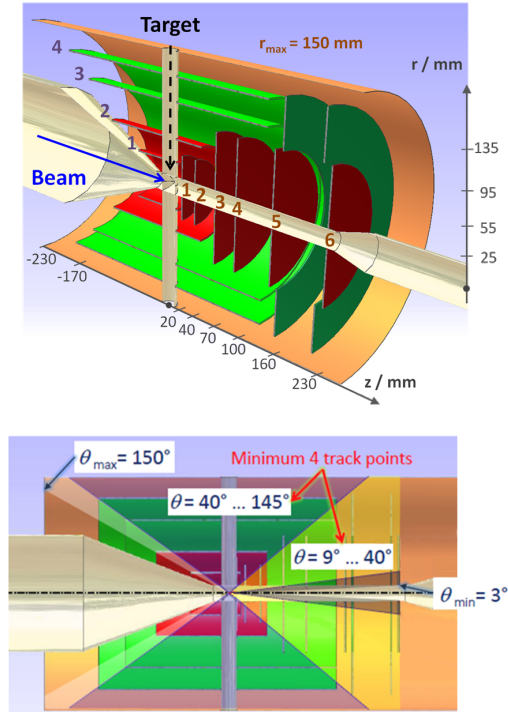


Figure 2.4: Layout of the *MVD*. Red: hybrid pixel silicon detectors. Green: double-sided silicon microstrip detectors. [5]

The MVD structure is composed of a barrel around the interaction point coaxial to the beam line and of a forward part with transverse disks to the z -direction. It has a maximum radius of 15 cm and an extension along the beam of $z \simeq 40$ cm with respect to the nominal interaction point.

It is composed of four barrels and six forward disks in order to have a detector coverage with a minimum of four track points in a polar angle interval from 9° to 145° :

- the *barrel part* covers polar angles between 40° and 150° . The upstream extension of all barrel layers is studied to fit with the opening cone of the beam pipe. Its radius range will be between 2.5 cm and 13.5 cm;
- the *disk layers* will cover polar angles between 3° and 40° . The first two layers will be located starting from $z = 2$ cm with respect to the nominal interaction point and at 2 cm far from this layer. The other four will be put forward downstream, two of them inside the strip barrel layers and the others with a larger radii outside them.

The two inner layers and the disks will be composed of hybrid pixel silicon detectors for a total of $10.3 \cdot 10^6$ readout channels. The other two barrel and the radial complements in the last two disks will be made of double-sided silicon microstrip detectors with $2 \cdot 10^5$ readout channels.

These kinds of silicon detectors have lots of favorable characteristics: fast response, low material budget, high degree of miniaturisation and good reproducibility. The hybrid pixel sensor will be the best choice for the inner layers because it can give discrete 2D information with high granularity that will allow to sustain the high rate of particle and precise space point measurements. The double-sided silicon microstrip detector will be the best choice in the outer layers because it needs less readout channels, and, accordingly, less material budget. Conversely, they could not be used in the inner part because of the probability of multiple hits which can lead to ambiguities.

2.3 Silicon Sensors

The sensor is the part where the interaction of radiation with matter takes place. It will act as a *pn junction in reverse-bias*. A pn junction is an interface between two types of semiconductor material inside a crystal of semiconductor. They have useful properties in modern electronics. A **n-type semiconductor** is defined as an extrinsic semiconductor with a larger electron than hole concentration. In this material the majority carriers are the electrons. A **p-type semiconductor** is conversely an extrinsic with more holes than electrons. *Holes* are the majority carriers. Both of them are created by doping an intrinsic semiconductor. For the *n*-type the impurities are called donors, for the *p*-type are acceptors. When the *pnjunction* is made, there is a movement of charge. From the *n* region, near the interface, the electrons diffuse into the *p* region leaving positively charged ions. From the other side, the holes diffuse towards the *n* region leaving fixed ions with negative charge. The region nearby the interface is not neutral anymore: it is a depletion region where there is an electric field generated by the space charge. The field is in

contrast with the diffusion until the equilibrium is reached. Without any applied voltage there is a balance between the components and there is a potential difference across the junction defined *built-in potential* V_{bi} . Reverse-bias is created applying negative voltages on the *p*-type region and positive on the *n* side. Depending on this reverse-bias there is a variation of the electric field in the depletion region. The *electric field* $E(x)$, the *built-in potential* V_{bi} and the *depletion region* W can be calculated as follows:

$$E(x) = \begin{cases} -eN_A(d_p + x), & -d_p < x < 0 \\ -eN_D(d_n - x), & 0 < x < d_n \end{cases}$$

$$V_{bi} = \frac{e}{2\epsilon}(N_A d_p^2 + N_D d_n^2)$$

$$W = d_p + d_n = \sqrt{\frac{2\epsilon V_{bi}}{e} \left(\frac{1}{N_A} + \frac{1}{N_D} \right)}$$

where N_A and N_D are the density of acceptors and donors respectively with the relative space charge boundaries d_p and d_n .

In Fig.2.5 are shown: the pn junction with zero bias voltage applied, the plot of the charge density, the electric field and the voltage.

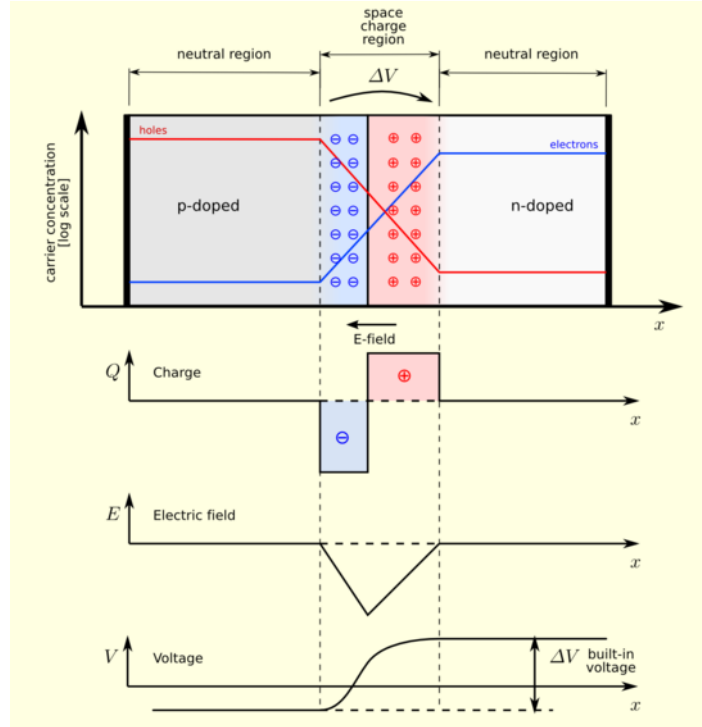


Figure 2.5: p-n junction with zero-bias voltage applied. The plots report the charge density, the electric field and the voltage with respect to the x coordinate

The depletion region can be also derived as function of the applied external voltage

(reverse-bias V_a) and of the resistivity (ρ) and the mobility (μ):

$$W \approx d_n = \sqrt{2\mu\rho(V_{bi} - V_a)}$$

The depletion region is the sensitive part of the particle detector. The applied voltage is increased until the entire region is empty in order to have full efficiency. The corresponding voltage is V_{dep} :

$$V_{dep} = \frac{l^2 e N_D}{2\epsilon} = \frac{l^2}{2\epsilon\mu\rho}$$

where l is the sensor thickness.

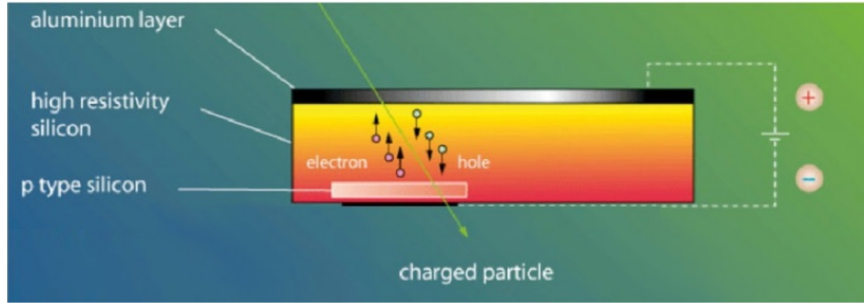


Figure 2.6: Electron-hole pairs generation in a high resistivity silicon. [5]

When a free energy particle enters the depletion region, it loses part of its energy generating electron-hole pairs (Fig.2.6). They are then removed by the electric field creating a current. This signal is the one that will be detected by the electronics. Also in absence of radiation there is always some noise represented by a steady dark current.

2.3.1 Hybrid Pixel Detectors

The general scheme of the hybrid pixel sensor will answer to all the requirements for the vertex reconstruction: spatial resolution, timing precision and radiation hardness.

It has two fundamental parts: the pixel sensor and the front-end ASICs (Application-Specific Integrated Circuit).

Pixel Sensor It consists of a two dimensional matrix of reverse biased silicon diodes. The sensor is made of a n type epitaxial silicon wafer with high resistivity (some $k\Omega\text{cm}$). It is obtained by growing on a silicon n^+ Czochralski substrate (CZ) with low resistivity ($0.01 - 0.02 \Omega\text{cm}$) which is removed in a second time. In order to have a good signal-to-noise ratio for particle identification studies and a good radiation tolerance, its thickness is $\sim 100 \mu\text{m}$. The pixel size is $100 \mu\text{m} \times 100 \mu\text{m}$ except for the ones on the boundaries ($300 \mu\text{m} \times 100 \mu\text{m}$). The size of the first kind allows to have an intrinsic spatial resolution of $\sigma_{pos} = 29 \mu\text{m}$.

Front-End ASIC It is the readout system, called ToPix, developed in $0.13\text{ }\mu\text{m}$ CMOS technology. In order to match the pixel sensor cells, the readout cell size is $100\text{ }\mu\text{m} \times 100\text{ }\mu\text{m}$. They are all arranged in a rectangular matrix of 110×116 pixels.

This system is self-trigger and needs to have a continuous data transmission of the events above a fixed voltage threshold.

As shown in Fig.2.7, the pixel sensor is bonded to the front-end by Sn-Pb bumps of $20\text{ }\mu\text{m}$ size. To improve the heat dissipation, the assembly is glued to a carbon foam layer that surrounds the cooling pipe.

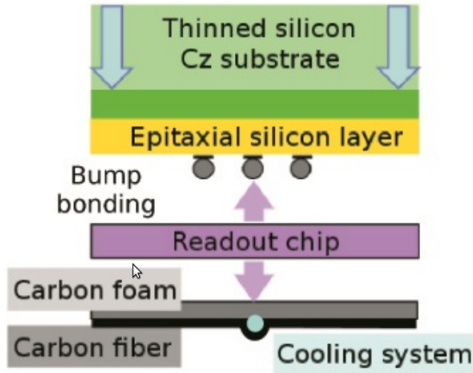


Figure 2.7: Hybrid pixels assembly for the $\bar{P}ANDA$ experiment. [5]

The readout size is studied to optimize the coverage. There are four different assemblies, as shown in the Fig.2.8.

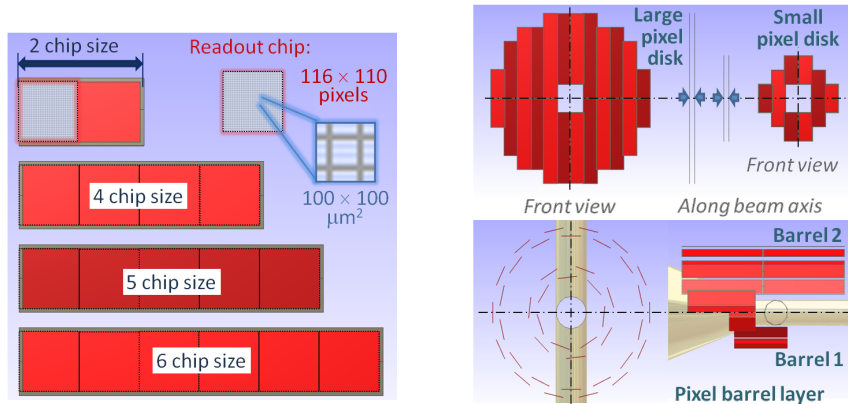


Figure 2.8: Scheme of the pixel sensor geometry. Top: main types. Bottom: arrangement in several detector layers. [5]

The disks around the beam pipe are divided vertically in two parts. The pixel barrel consists of two cylindrical layers. The first has 8 staves made of 4 sensors and 6 staves made of 2 modules. The second layer has 6 staves of 5 modules and 22 staves of 6 sensor.

The readout chips are wire-bounded to the hybrid. It is glued on the top of the sensor. The module is connected to a service board, GigaBit Transceiver system (Fig. 2.9), which performs the multiplexing and the electrical-to-optical conversion as close as possible to the detector in order to send the big amount of data by optical fibres (Versatile Link project). This link can be used in both directions: to receive data from the detector and to send the clock and load parameters to the front-end.

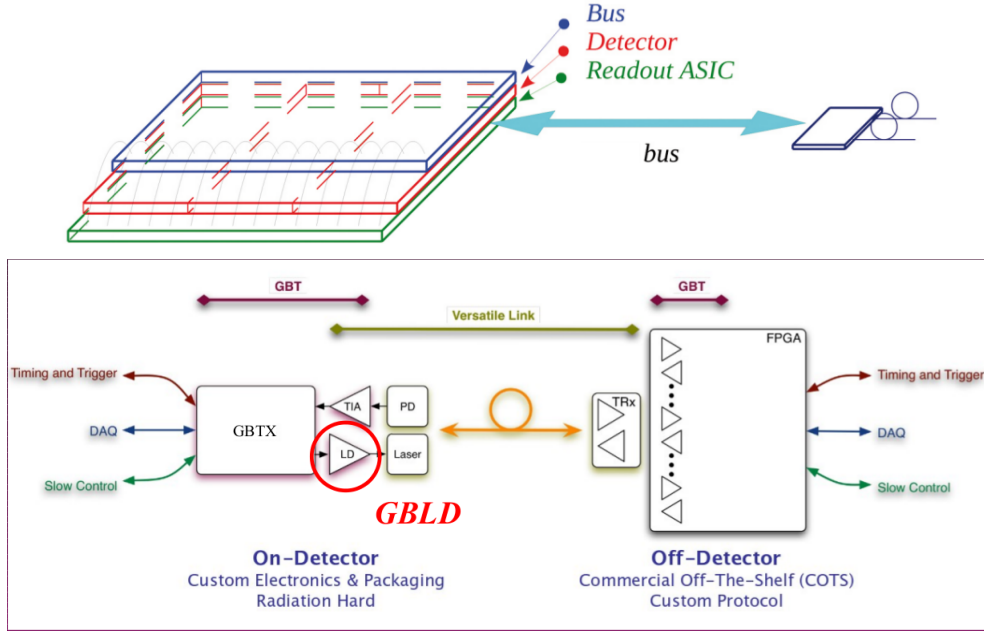


Figure 2.9: Top:Pixel readout scheme [5]; Bottom: GBT and VL scheme.

One half of the GBT system is close to the detector and still in a radiation hard environment. It needs custom electronics. The second half, to the other side of the optical fibres, is free from radiation. The "on-detector" part is composed of:

- GBTX It provides the interface to the detector front-end electronics;
- GBTIA It receives the 4.8 Gb/s serial input data;
- GBLD It is a laser-driver ASIC to modulate the serial data on a laser.
- GBT-SCA It provides the slow-controls interface.

2.3.2 Double-Sided Silicon Microstrip Detector

Silicon strip detectors have some advantages for application in nuclear and particle physics. They show good spatial resolution, low material budget and good radiation tolerance.

The strips are realised in p^+ type silicon on the front side and in n^- type silicon in the back side and the substrate on bulk is n -type (Fig.2.10).

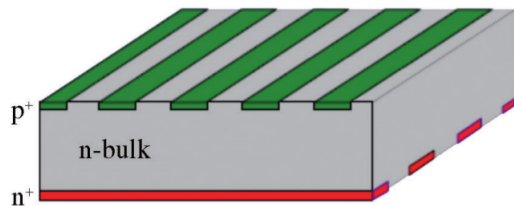


Figure 2.10: Layout of the DSSD.[5]

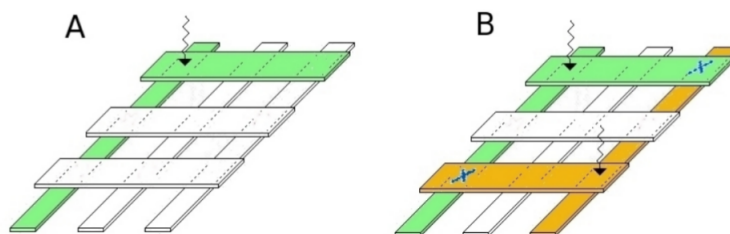


Figure 2.11: Ghost hit problem (blue crosses)

They are arranged respectively in rows and columns and they foresee a two dimensional information. Their limit is given by the method employed for the hit identification and by the management of multiple hits. When a charged particle hits the detector, its position is given by the intersection of the strip from the row and the column. When the particles that hit the detector at the same time are more than one, a ghost particle can be detected by all the possible combinations between upper and lower layers (Fig. 2.11). This kind of detector is used in the outer part where the density particle is lower.

In the structure of the MVD there are three different types of strip modules (Fig. 2.12): rectangular and squared for the barrel part and trapezoidal for the disks. The first has a stereo angle between p -side and n -side of 90° and a pitch of $65 \mu\text{m}$. The trapezoidal one, instead, has a stereo angle of 15° and a pitch of $67.5 \mu\text{m}$ to compensate the worsening of the spatial resolution.

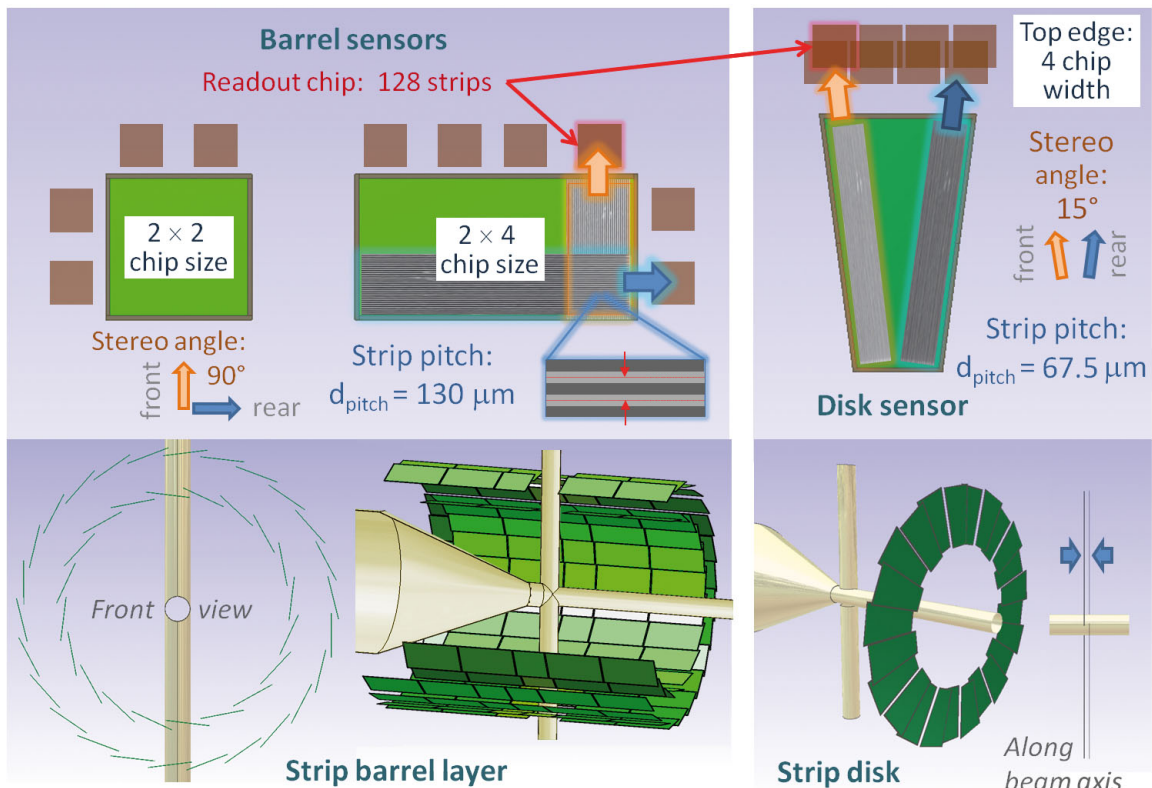


Figure 2.12: Scheme of the strip sensor geometry. Top: main types. Bottom: arrangement in different detector layer.[5]

Chapter 3

Single Event Upset

Single Event Effects are one of the main problems facing semiconductor electronic components. They are induced by the interaction of an high energy ionizing radiation. As a single ionizing high-energy particle penetrates a circuit, it leaves behind a dense plasma track in the form of electron-hole pairs. A circuit error, or even a circuit failure, will occur if sufficient charge from the plasma track is collected at a sensitive circuit node. There are different kinds of Single Event Effects:

- **Single Event Upset (SEU).** It is a change of state induced by ionizing radiation striking a sensitive node of a logical element. It causes mistakes in the output of the device.

It is not considered a permanent damage.

- **Single Event Latchup (SEL).** It can occur in chips with a parasitic $p-n-p$ or $n-p-n$ structure. The particles interfere with the correct functionality of the device by starting regeneration action crossing the base-emitter ($n-p-n$ type) or the emitter-base ($p-n-p$ type) junction and by leading excessive power supply that makes it unusable.

It may cause a permanent damage to the device. If there is not a permanent damage, a power cycle (off and on) of the device is necessary to restore normal operation.

- **Single Event Snapback.** Similar to SEL, it is a regenerative current mechanism. It can occur in absence of a $p-n-p$ structure.
It may cause the destruction of the device.

- **Single Event Burnout.** The passage of a single heavy ion in a power MOSFETs can bias the substrate under the source region. This increase the drain-source voltage until is higher than the breakdown voltage.

The high current and the overheating can destroy the device.

- **Single Event Gate Rapture.** It occurs when a heavy ion hits the gate region of

a power MOSFETs while a high voltage is applied.

It causes overheat and a local destruction of the gate region.

SEU errors are a bit, logic or memory, flip. The energy deposition in the volume of the electronic chip causes an increase of the current level or an excess of charge collected near a sensitive part of the circuit. They are non-destructive events. They cause the lost of the information stored in the bit at the moment of the upset. At the next logic cycle or memory write operation the circuit becomes functional again.

My work foresees the determination of Single Event Upsets for two different devices of the Micro Vertex Detector: ToPix (in his third version *v3*) and GBLD, GigaBit Laser Driver (fourth and fifth version). The SEU can induce two main problems in the prototypes:

- loss of the detector functions' control;
- corruption of a fraction of data stored in the memory.

The most sensitive regions are the reversed biased *p-n* junctions where the electric field collects the charges by drift [14]. The SEU occurrence depends on two main parameters:

- **Sensitive Volume (SV):** it is the volume where the ionization causes the charges collection on the node;
- **Energy Threshold:** it is the minimum energy deposition in the sensitive volume that can trigger an upset.

3.1 Particle interaction with the matter

The particles that can interact with the matter can be divided in three categories:

- Photons. They interact in three different ways:
 - *photoelectric effect* ($E < 50$ keV). The interaction produces the emission of an electron which has absorbed completely the photon energy.
 - *Compton scattering* ($50 \text{ keV} \leq E \leq 20 \text{ MeV}$). A portion of the incident photon energy is used to create an energetic Compton electron, while the lower energetic photon continues the travel through the material.
 - *pairs production* ($E > 20 \text{ MeV}$). The photon is completely absorbed producing a positron-electron pairs.
- Charged particles. They interact primarily by *Rutherford scattering*, but they can also have *nuclear interactions*. They can cause excitation and ionization of atomic electrons and, additionally, with enough energy, can produce the displacement of an atom from its lattice site.

- Neutrons. Their interactions with the target are only nuclear reactions:
 - *elastic scattering*. With imparted energy above ~ 25 eV, the neutron transfers the energy to an atom of the target material which is removed from its lattice position. This atom, subsequently, will lose energy to ionization and could also displace other atoms.
 - *inelastic scattering*. The incident neutron is captured with the emission of another particle with lower energy. The kinetic energy lost in this process can leave the target in an excited state. The return to the original state is done with the emission of a γ ray.
 - *transmutation reactions*. This process provides the capture of the incident particle and the emission of another one. The remaining atom is converted from an element to another.

In order to foresee the radiation effects on electronic devices, the attention in this chapter is focused mainly on the interactions that can trigger SEU in the PANDA environment.

In the following paragraphs the processes described are:

- *energy loss*, through ionization and bremsstrahlung;
- *elastic scattering*, by Coulomb interaction;
- *nuclear reactions* by studying their cross section in silicon.

Energy loss

Ionization It corresponds to the generation of electron-hole pairs. An energetic particle that impacts on the matter excites an electron. It loses a small fraction of the total kinetic energy but it is still significant because there are several collisions for unit path length. The electron goes in the conduction band and it leaves a hole in the valence one. This electron-hole pair is free to diffuse and to drift until a recombination occurs in the material or until the pairs are collected at an electrode. In the semiconductor junction regions, the main problem is that the present electric field causes the charge separation and its collection on a node. If the charges are greater than the ones carrying the elementary pieces of information, a single event upset can occur.

The analysis of this process can be made with the average energy loss. It is also called *stopping power* or dE/dx or *Linear Energy Transfer (LET)*. The latter in particular is the energy deposited in the matter per unit length. It is given in $\text{MeV} \times \text{cm}^2/\text{mg}$.

This energy loss is expressed by the **Bethe-Bloch** formula:

$$-\frac{dE}{dx} = 2\pi N_A r_e^2 m_e c^2 \rho \frac{Z}{A} \frac{z^2}{\beta^2} \left[\ln \left(\frac{2m_e c^2 \gamma^2 \beta^2 W_{max}}{I^2} \right) - 2\beta^2 - \delta - 2\frac{C}{Z} \right]$$

It is the relativistic calculation that parameterizes the energy transfer as a function of the momentum transferred with:

- | | |
|---|---|
| - r_e electronic radius; | - m_e electronic mass; |
| - N_A Avogadro's number; | - I mean excitation potential; |
| - Z absorbing material atomic number; | - z incident particle charge; |
| - A absorbing material atomic weight; | - $\beta = \frac{v}{c}$ of incident particle; |
| - ρ absorbing material density; | - $\gamma = 1/\sqrt{1 - \beta^2}$; |
| - δ density correction; | - C shell correction; |
- $-W_{max} = \frac{2m_e c^2 \beta^2 \gamma^2}{1 + 2\frac{m_e}{M} \sqrt{1 + \beta^2 \gamma^2} + \frac{m_e^2}{M^2}}$ maximum energy transfer produced by a knock-on collision for a incident particle of mass M.

In particular the corrections are:

- the density correction δ . It is important at high energy. It is correlated to the possible polarization of the atom caused by the electric field generated along the path by the particle.
- the shell correction C . It is important for slow incident particles, when the particle velocity is comparable with the orbital velocity of a bound electron. In this case the electron cannot be considered stationary and the Bethe-Bloch formula breaks down.
- other corrections can be due to: radiation effects at ultra-relativistic velocities, kinematic effects due to the infinite mass assumption, higher-order QED processes, higher-order terms in the scattering cross section, corrections connected to the internal structure of the particle, spin effects, electron capture at very slow velocity. These corrections are of the order of $\sim 1\%$ and are usually negligible.

Moreover, using this formula for the process e^- (projectile) e^- (target), it is necessary consider that:

- the electron mass is too small to make valid the assumption that the incident particle remains undeflected during the collision process;

- the particles in the interaction can be identical, so the calculation have to take into account their indistinguishability.

An example of the trend of the Bethe-Bloch formula in different materials and for different particles is shown in Fig. 3.1

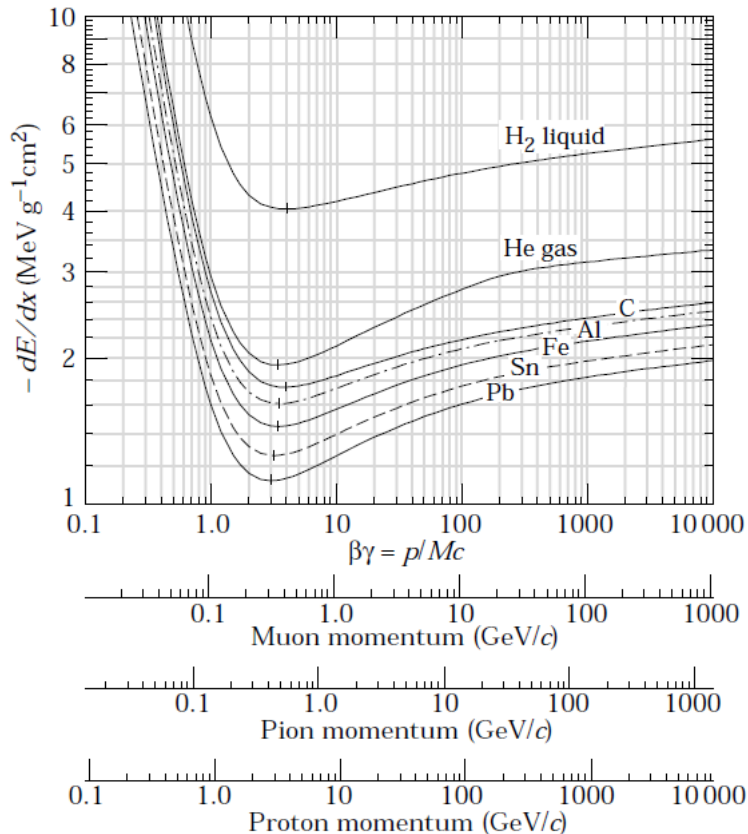


Figure 3.1: Energy loss rate in liquid, hydrogen, gaseous helium, carbon and other materials by different particles[10]

The dE/dx curve has four characteristic zones (Fig. 3.2):

- A: a rapid decrease ($\propto \frac{1}{\beta^2}$);
- B: the minimum of the energy loss;
- C: a slow increase ($\propto \ln \gamma$);
- D: a constant loss of energy.

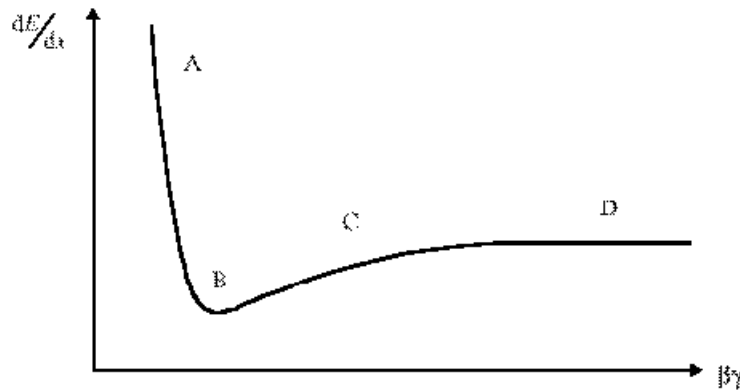


Figure 3.2: Trend of stopping power

According to the Bethe-Bloch formula, the specific energy loss increases when the energy falls. The plot of the specific energy loss along the track of a charged particle is reported in Fig. 3.3 and is called *Bragg Curve*.

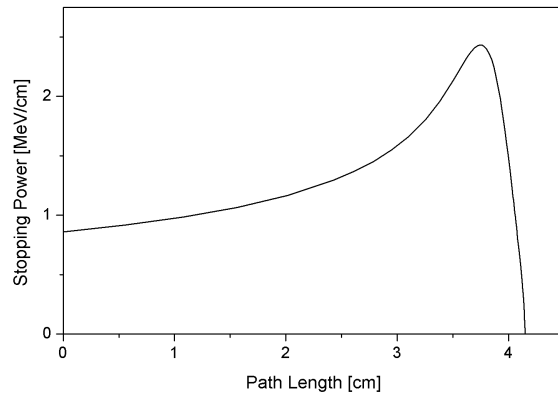


Figure 3.3: Bragg Curve. Energy loss of Alphas of 5.49 MeV in air. [12]

In particular, this plot shows how LET increases with recoil energy until it reaches the maximum, *Bragg peak*, and then decreases quickly to rest. LET depends on the energy, on the incident particle and also on the material through which the particle passes. The distance in which the particle stops in the material is called *range*. Because this interaction nature is statistical, not all the particles at the same energy will stop at the same distance or will have the same number of collisions. This variation in the range is called *straggling*. Fig. 4.5 shows the number of transmitted particles over the thickness of the material in which the particles are stopped.

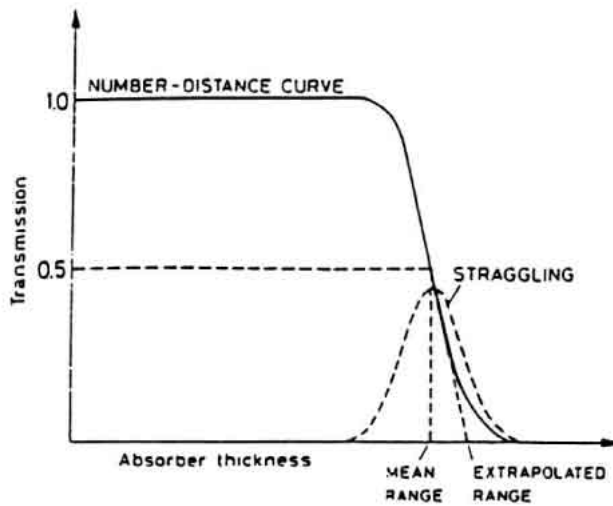


Figure 3.4: Outgoing particles and incident particles ratio with respect to the absorber thickness

Bremsstrahlung It is the electromagnetic radiation that occurs when a charged particle causes the deflection and the deceleration (or acceleration) of another particle. The particle that has been moved loses, in this way, kinetic energy which is converted, for energy conservation, into a photon. This kind of process happens at energies above few tens of MeV. It is a negligible process for massive particles.

The energy at which the energy loss for ionization and for bremsstrahlung becomes comparable is defined *critical energy* and depends on the material (Fig. 3.5):

$$E_C = \frac{800 \text{ MeV}}{Z + 1.2}$$

(For silicon $E_C = 52.63 \text{ MeV}$.)

For SEU analyses it is considered a volume of $1 \times 1 \times 1 \mu\text{m}^3$, chosen by the authors of [14] as a realistic estimate of the sensitive volume. The deposited energy by protons and electrons in $1 \mu\text{m}$ of silicon layer is plotted in Fig. 3.6.

A 1 GeV proton and electron lose 419 eV and 10.88 keV respectively, not sufficient to trigger an upset. Instead a heavy ion can play an important role as shown in the *Nuclear Reaction* paragraph.

Elastic Scattering

Coulomb Interaction In the case of elastic scattering, the incident particles need to have a minimum energy to remove a silicon atom from its position. It is calculated taking into

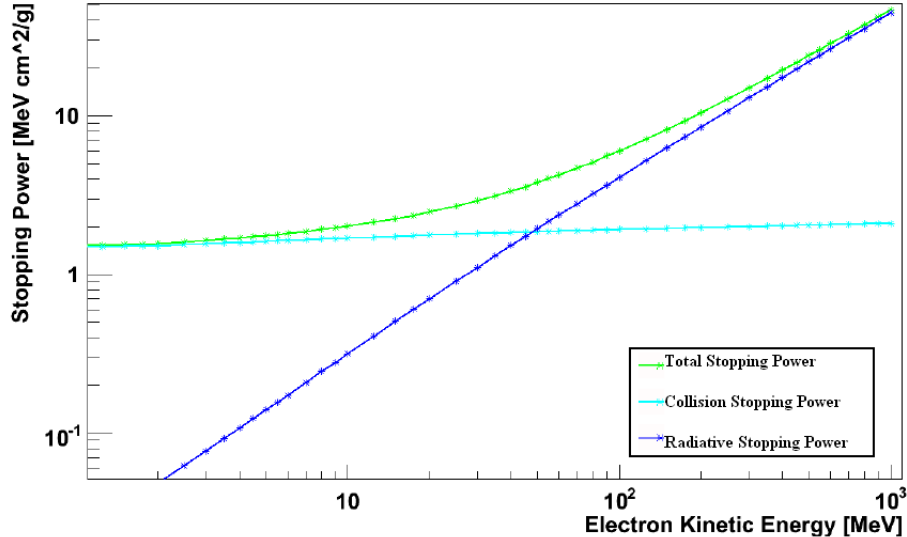


Figure 3.5: Comparison between radiation and collision loss vs electron kinetic energy in silicon [11]

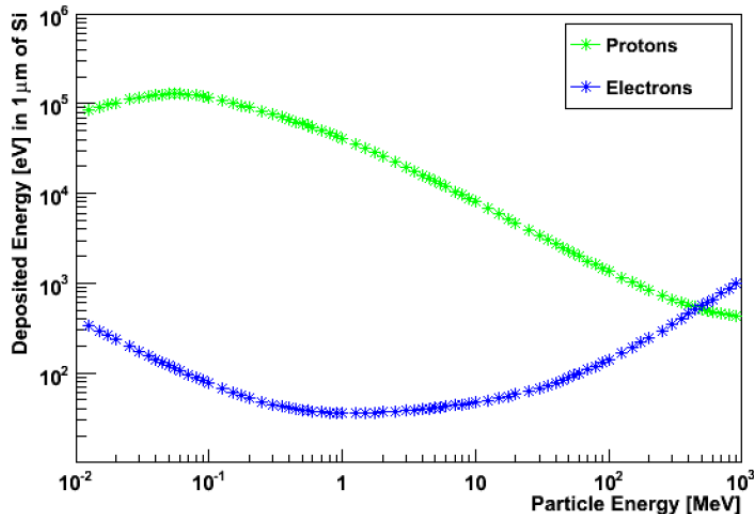


Figure 3.6: Deposited Energy of protons and electrons in $1 \mu\text{m}$ of silicon

account the kinetic formulas of the process of a two bodies collision.

$$E_{min} = 0.5 \left[E_{rec} + \sqrt{E_{rec}^2 + 4m_p^2 + 2E_{rec}M_{Si}} + \frac{2E_{rec}m_p^2}{M_{Si}} \right] - m_p$$

where:

E_{min} : minimum particle energy

m_p : particle mass [eV]

E_{rec} : recoil energy of Si atom

M_{Si} : silicon atom mass [eV]

The minimum recoil energy is ~ 25 eV. The minimum kinetic energy of the incident electrons

needs to be 256 keV, instead for protons 188 eV, because of the higher mass. In Fig.3.7 the recoil energy is calculated taking into account the 25 eV needed to remove the atom from the crystalline structure.

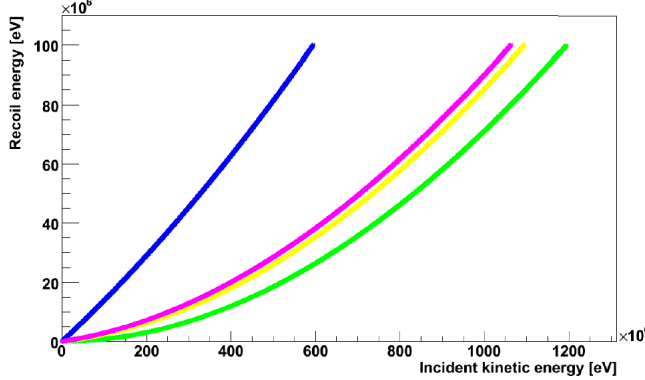


Figure 3.7: Silicon recoil energy with respect to different particle incident energy. In green the electron's energy, in blue proton's one, in yellow muon's energy and in violet the pion's one.

It shows that the silicon recoil energy allows to have an appreciable energy loss that can produce significative effects in the material. The kinematical analysis and the momenta of different particles that release the minimum recoil energy to trigger an upset are reported in Table 3.1.

	e^-	μ^-	π	p
Kinetic Energy	56.8 MeV	14.7 MeV	11.3 MeV	1.88 MeV
Momentum	57.3 MeV/c	57.3 MeV/c	57.4 MeV/c	59.2 MeV/c

Table 3.1: Minimum kinetic energy and momentum needed to release the minimum silicon recoil energy necessary to trigger an upset

A real interaction is considered using the relativistic Rutherford formula. The differential elastic cross section for electrons is calculated as:

$$\frac{d\sigma_R}{d\Omega} = Z^2 a_0^2 E_h^2 \frac{(E + mc^2)^2}{E^2 (E + 2mc^2)^2} \frac{1}{(1 - \cos \theta)^2}$$

where $E_h = 27.211$ eV is the Hartree energy and $a_0 = 52.918$ pm is the Bohr radius, considering a Dirac-Fock density and a point nucleus. It is reported in Fig.3.8 that it decreases as a function of the energy.

It is expected for electrons in the PANDA pixel detector an energy spectrum lower than 2 GeV, that is low probability to trigger an upset. Also elastic cross section of protons and neutrons can be calculated. Some values are reported in Table 3.2.

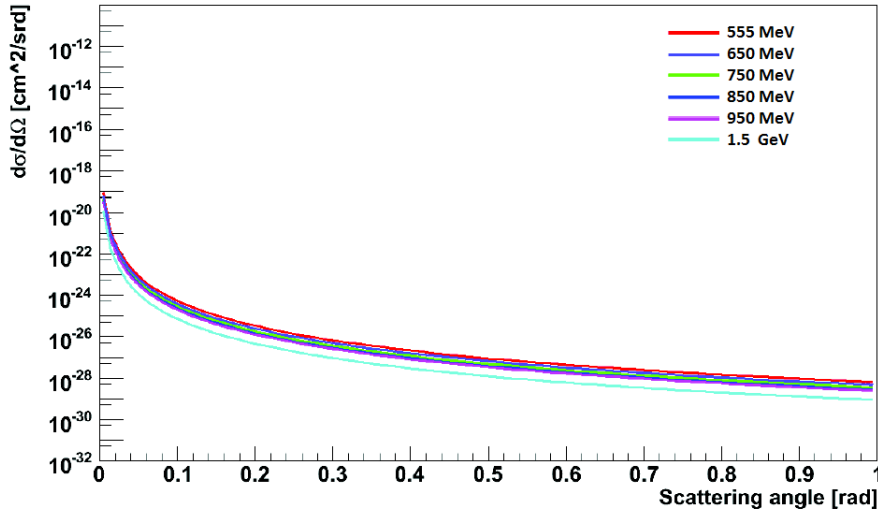


Figure 3.8: Differential elastic cross-section of electrons on silicon for different energies.

Angle	Particles	$d\sigma/d\Omega$ [barn/srd]
30°	e^-	10^{-1}
	p	10^{-1}
60°	e^-	10^{-3}
	p	10^{-3}

Table 3.2: Elastic $^{28}\text{Si}(e^-, e^-)$ and $^{28}\text{Si}(p, p)$ scattering at 100 MeV

In $p\bar{p}$ annihilation at 15 GeV/c, the ratio p/e^- on the first pixel disks is expected to be ~ 10 . Hence, in this experiment are expected mainly hadronic processes and therefore their contribution to SEU rate will not be negligible.

Nuclear Reaction

Cross Section in Silicon The typical nuclear reaction can be written as shown:

$$a + X \rightarrow Y + b$$

where:

a is the accelerated projectile, X is the target, Y and b are the reaction products.

Nuclear reactions can be classified:

- scattering processes: incident and outgoing particles and nuclei are the same. It is elastic if the products are in their ground state. Instead, if they are in the excited states, the scattering becomes inelastic.
- knock-out reactions. In the processes a and b are the same and a nucleon is ejected separately.

- transfer reactions. There is the transfer of one or two nucleons between projectile and target.

The conservation of total energy, linear and angular momentum can be used in order to know the properties of the outgoing particles.

The energy deposition of the nuclear recoils is useful to make a quantitative evaluation of reactions inside silicon that can create a SEU. In fact:

- a neutron does not lose energy by ionization because is a neutral particle;
- the small recoil energy from the collision can play a role in the ionization;
- (n,p) or (n,α) processes have greater cross sections than other reactions (Fig.3.9);

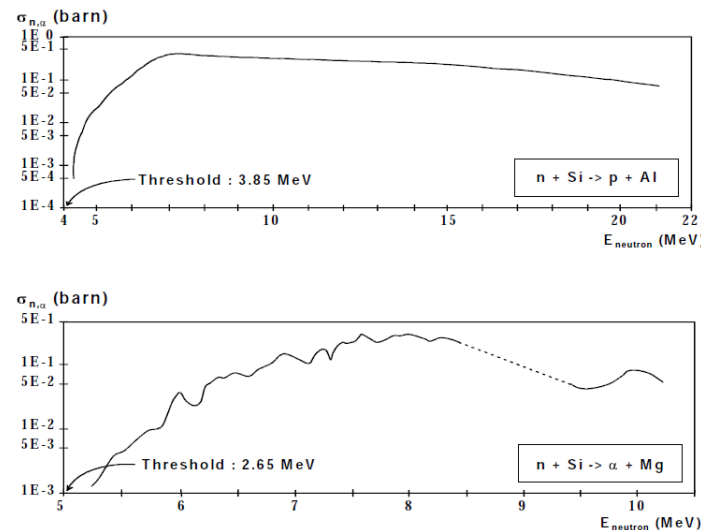


Figure 3.9: Cross Section of n-Si nuclear reaction [13].

In general the energy range for these processes is from few hundred keV to few MeV.

The heavy ions are the particles that better answer to all these features. According to the Bethe-Bloch formula, the energy loss is proportional to z^2 and therefore the deposit energy of the recoil is greater than the energy lost by high energy particles. In fact nuclear reaction needs more complex studies that can be only made by numerical simulations and codes as the authors of [14] show. In Fig. 3.10 are shown illustrative data of this situation taken from the SRIM (Stopping and Range of Ions in Materials) simulation code [15]. As explained in the next chapter, it is used to know the ions features.

The devices are then tested with heavy ions in order to know the SEU sensibility and their rate on the pixel part in $\bar{\text{P}}\text{ANDA}$. This is described in Cap.4.

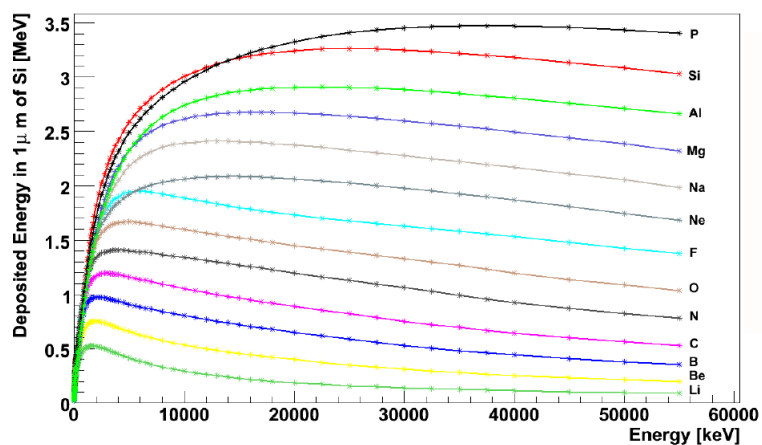


Figure 3.10: Deposited energy of different ions in silicon, with respect to recoil nuclei energies[15].

Chapter 4

Heavy Ion Irradiation

The SEU studies are a fundamental issue in high energy physics. They are necessary to understand the radiation effects on semiconductor devices. In this work, the radiation tolerance on SEU is studied for two prototypes of the circuits of the readout architecture part for the Micro Vertex Detector. ToPix and GBLD have been tested at the SIRAD (SIlicon RAdiation Damage) irradiation facility, located at the INFN National Laboratory of Legnaro (Padova). The facility is dedicated to studies of electronic devices and of bulk damage in semiconductor detectors for high energy physics and space applications. The tests have been performed in November 2012 and in February 2014.

4.1 SIRAD Facility

In the National Laboratory of Legnaro, INFN of Padova, there is the Tandem-XTU accelerator that is an electrostatic Van de Graaff type. In this structure there are two stripper stations in order to achieve high ion energies. The ion's energy, at the end of the Tandem can be calculated as:

$$E = E_{inj} + V_0 [1 + q_1 f + q_2(1 - f)]$$

- $E_{inj} = 0.18$ MeV : energy of the negative charge ion injected from the source into the Tandem;
- $V_0 = 11 \rightarrow 15$ MV : operation voltage;
- $f = 0.25$: distance of the stripper stations;
- q_1 : ion charge after the first stripper foil (unit of electron charge);
- q_2 : ion charge after the second stripper foil (unit of electron charge).

The available ions and the typical energies are listed in Tab.4.1.

After the Tandem, as shown in Fig.4.1, it is performed a magnetic momentum analysis to select one of the many possible ion charge states of the not monochromatic beam and, then, a switching magnet deviates the beam into the experimental channels. It serves 3 experimental halls and 10 beam lines.

Ion	Energy [MeV]	q_1	q_2
1H	28.18	1	1
7Li	56.18	3	3
^{11}B	80.68	4	5
^{12}C	94.68	5	6
^{16}O	108.68	6	7
^{19}F	122.68	7	8
^{28}Si	157.68	8	11
^{32}S	171.68	9	12
^{35}Cl	171.68	9	12
^{48}Ti	196.18	10	14
^{51}V	196.18	10	14
^{58}Ni	220.68	11	16
^{63}Cu	220.68	11	16
^{74}Ge	231.18	11	17
^{70}Br	241.68	11	18
^{107}Ag	266.18	12	20
^{127}I	276.68	12	21
^{197}Au	275.68	13	26

Table 4.1: Typical ion beams available at SIRAD with the Tandem at 14 MV

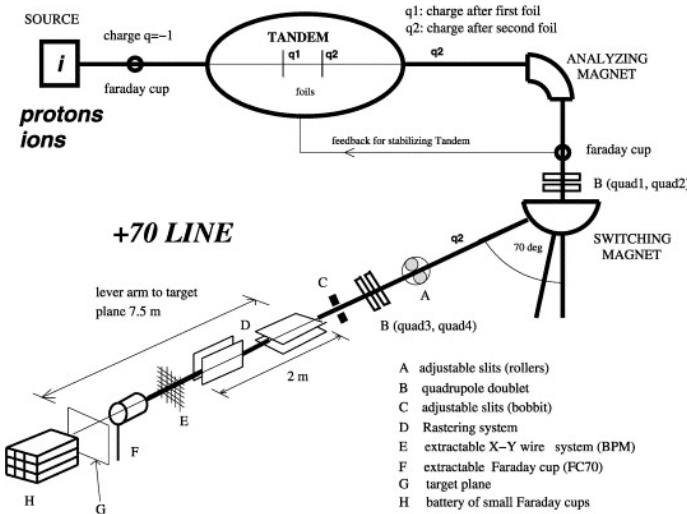


Figure 4.1: Schematics of the Tandem-XTU and of the SIRAD irradiation facility at the +70° beam line.

One of those lines, located in the hall 1, is SIRAD, dedicated to bulk damage and single event effect studies in semiconductor devices and electronic systems for high energy physics and space application [16].

The beam available in this facility is chosen with the energy value that refers to the most probable charge state obtained with the two stripper stations and with the Tandem operating at 14 MV and have a focus of 3-4 mm. A system of wires [E] and a Faraday cup [F] positioned in the di-

agnostic chamber located 80 cm upstream of the target plane allow to control the beam (Fig.4.1).

To take advantage of the full beam, the irradiation of the device under test is made in vacuum (better than $8 \cdot 10^{-6}$ mbar) into an irradiation chamber (Fig. 4.2) where there is a sample holder ($33 \times 10 \text{ cm}^2$ along vertical and horizontal axis respectively). On it, the device under test, a quartz and a diodes board are positioned. The sample holder is motor controlled in order to move under the beam the different devices without breaking the vacuum. The quartz is necessary to center the beam. The diodes, as explained in the following lines, are used to control the beam fluence.

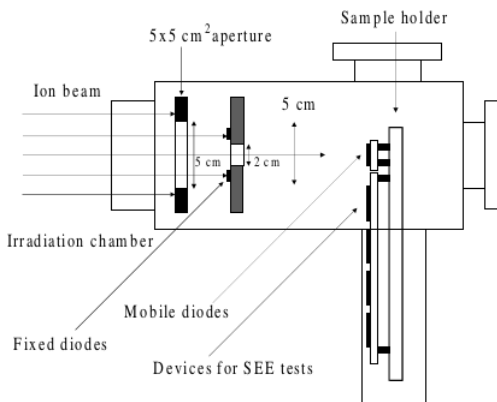


Figure 4.2: On-line beam monitoring sistem. Side view of the experimental set-up. It is shown the sample holder into the irradiation chamber.

For the SEU studies, low ion fluxes (from 10^2 to 10^5 ions/ $(\text{cm}^2 \text{ s})$) are necessary. Low beam currents and a defocused beam are the main features. The first is obtained by closing the machine collimators and the second is controlled by the quadrupole doublet. In order to control the ion fluxes, two batteries of four diodes intercept the ion beam (Fig.4.3a, Fig. 4.3b).

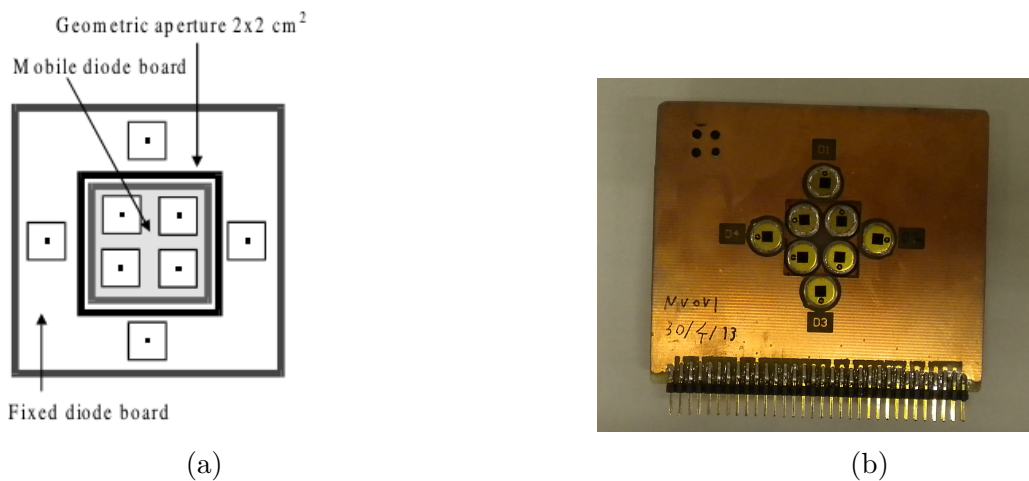


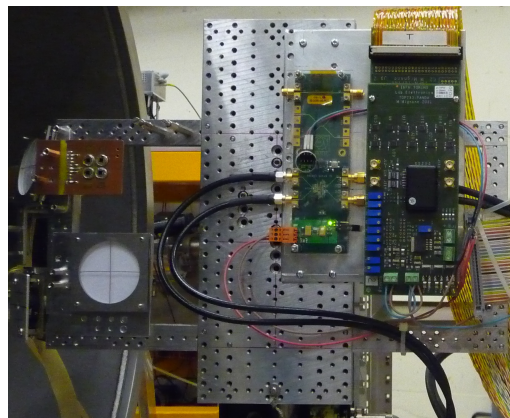
Figure 4.3: On-line beam monitoring system. (a): front view (transverse to the beam) of the fixed and mobile diodes boards. (b): real fixed and mobile boards together.

One battery is mounted on a fixed frame with a central aperture of $2 \times 2 \text{ cm}^2$ surrounding the device under test to monitor the shape of the defocused beam. The other one is mobile. It can exchange the position with the device. Before every run the beam set up procedure is made with all the eight diodes. The ratio between the fluxes on the fixed and mobile diodes allows to know the internal fluence to be considered in the dosimetry analysis of the device. During the run, instead, only the fixed diodes are used around the device to control the beam. The sensitive area of the diode is $0.5 \times 0.5 \text{ cm}^2$. During the test of the prototypes two multi-sources were used to decrease the time for beam setting:

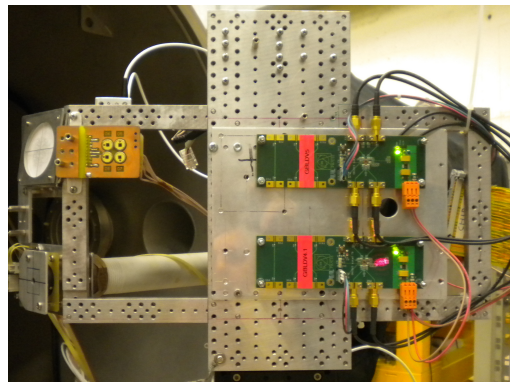
1 : O, Si, Ni, Ag;

2 : F, Cl, Br, I.

Moreover, the diodes that have been used have two different dimensions. During the November test they were $2.73 \times 2.73 \text{ mm}^2$. In February test, instead, the $5 \times 5 \text{ mm}^2$ were used. This difference will be considered in the dosimetry analysis. In Fig. 4.4a is shown the sample holder in the irradiation chamber during the November test. Together with the quartz and the mobile diodes, on the left there is the GBLD and ToPix_v3 on the right. In Fig. 4.4b there is the February test setup with the GBLD_v4 on the bottom part and the GBLD_v5 on the top.



(a)



(b)

Figure 4.4: The sample holder inside the irradiation chamber. (a): November test setup; (b): February test setup

4.2 Prototypes

4.2.1 ToPix 3.0

The MVD has to provide position, time and energy loss measurement for each hit. As presented in the Section of the Hybrid Pixel Detector, the pixel module has a three level structure: sensor, front-end chip and the hybrid. ToPix is the third pixel readout ASIC prototype for the pixel readout. It was designed at the INFN Electronic Laboratory of Turin.

Description ToPix is developed in a $0.13\text{ }\mu\text{m}$ CMOS technology for its high level of integration and the intrinsic radiation tolerance of deep submicron technologies [5]. It has metal and insulation layers placed as shown in Table 4.2. The prototype includes 640 cells arranged in 2×128 and 2×32 double columns. The die size is $4.5 \times 4\text{ mm}^2$. The 128 cell columns have been folded in order to have a better die form factor. Digital input and output are based on the Low Voltage Differential Signaling (SLVS), in order to be compatible with the single 1.2 V power supply. Each cell contains both analog and digital electronics needed to amplify the signal and to digitize the charge. The only pieces of information extracted from the readout cell are the digital ones. There are a configuration register control by a peripheral logic and two additional pixel registers where the data are stored.

Pixel Cell As mentioned before, the pixel cell contains both analogue and digital parts (Fig 4.5 and Fig 4.6 respectively).

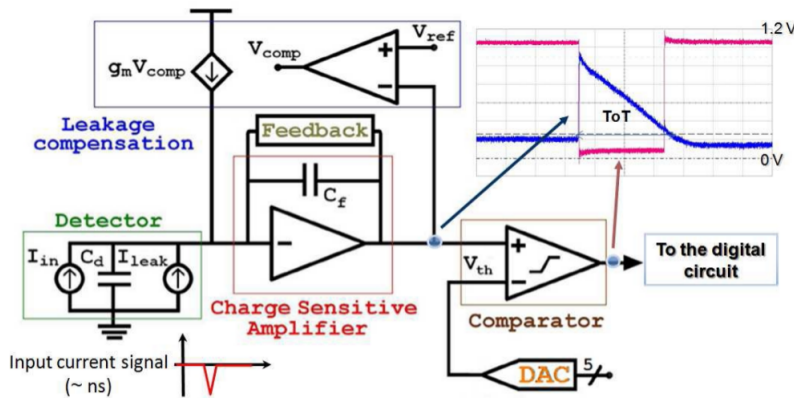


Figure 4.5: Analogue readout channel [5]

The analogue part is composed by a preamplifier and a comparator. The charge preamplifier is a low noise circuit. It has a feedback capacitor ($C_f = 12\text{ fF}$), a constant current discharge circuit (for the Time over Threshold technique implementation) and a leakage current compensation circuit. Each pixel can be enabled by the configuration register to receive a calibration signal (for example, for the baseline calibration). After the preamplifier there is the comparator. It is based on a folded cascode architecture. Its task is to compare the analog output of the preamplifier with a threshold voltage. This threshold voltage is set by global DAC, but it can

be fine adjusted with a 5-bit local DAC from the configuration register. Its value has to be fixed not too close to the baseline in order to avoid picking up the noise, and not too far from the baseline in order to be able to detect small values of charge. When the preamplifier output crosses the threshold, the comparator switches to 1 and the timestamp value is loaded in the leading edge register. Then the integrating capacitor is discharged and when the analog output goes below the threshold, the comparator switches to 0. The timestamp value is now loaded into the trailing edge register. In this way the leading edge register records the time, while the difference between trailing and leading edge register records gives the signal width. This last is proportional to the amplitude of the signal and finally to the particle energy loss inside the silicon sensor.

The registers contained in each pixel readout cells are:

- the *Configuration Register*: it is a 8 bit register. It has 5 bit for the comparator threshold DAC, 1 bit to enable the comparator output, 1 bit to enable the internal test charge injection and 1 bit to mask the comparator output (for a noisy pixel).
- the *Leading Edge Register*: it is a 12 bit register. It stores the timestamp value when the comparator switches from 0 V to 1.2 V (from 0 to 1 logic).
- the *Trailing Edge Register*: it is a 12 bit register. When the comparator switches from 1.2 V to 0 V, it stores the timestamp bus value.

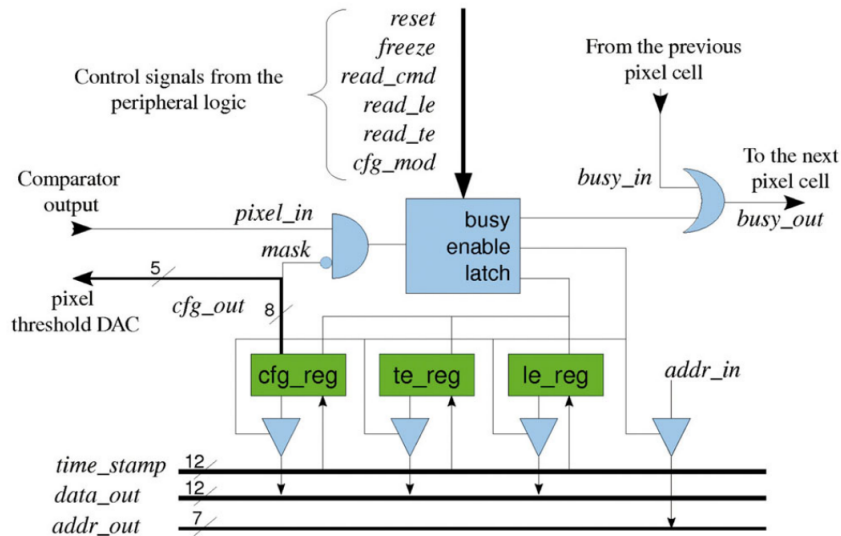


Figure 4.6: Pixel control logic [5]. *cfg_reg*: configuration register; *te_reg*: trailing edge register; *le_reg*: leading edge register.

An upset in any bit causes an incorrect storage of value in all the registers. To prevent this, in all register the Single Event Upset tolerance is implemented by the Triple Modular Redundancy (TMR) with 3 latches circuits.

ToPix Architecture As mentioned before the pixel cells are organised in double columns which share the same timestamp and the readout buses. For each double column there are, in addition to the 2×128 and 2×32 cells, a 12-bit timestamp bus, a 7-bit address bus and a 12-bit data bus. The architecture is based on a timestamp which is generated by a counter synchronous to the clock signal, Gray-encoded [24] and distributed over the pixel matrix.

The column readout scheme is performed in the following way (Fig.4.7). The pixel cell receives

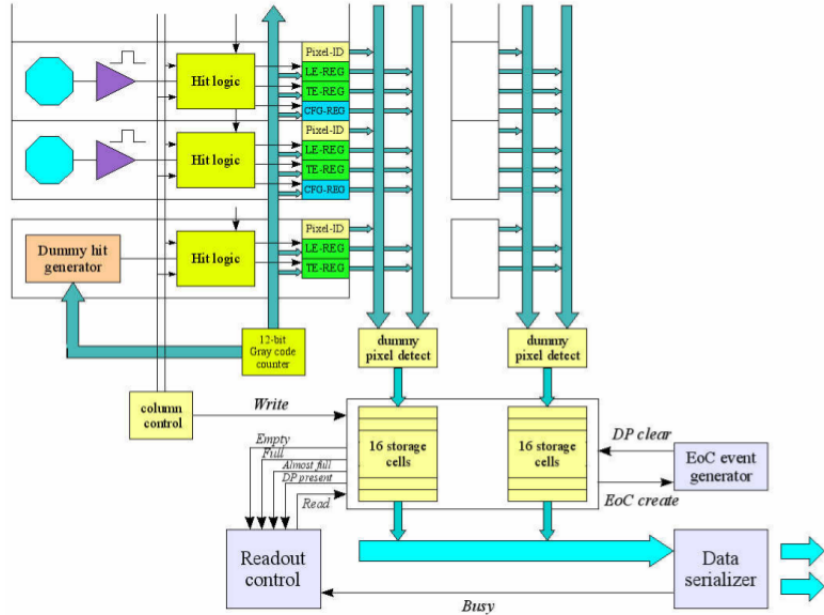


Figure 4.7: Column readout schematic [5]

a hit and it generates a busy signal. This signal is put in logical OR with the previous cell and it is sent to the next one. In this way, if at least one pixel receives a hit, the busy signal at the end of column is high (1). Now a read command is sent to all the pixel cells. The first pixel cell that sends its data and address to the output bus is the one with the busy input signal at zero. During the readout a freeze signal is used to block the generation of a new busy signal.

This same scheme is used also for the configuration data. The configuration mode signal puts all the pixels in a busy state. Then a command addresses the pixel from the one with highest priority to the one with the lowest.

The double columns are controlled by a Column Readout Control Unit (CRCU) that contains four different components:

- a bank of differential drivers for the timestamp propagation;
- a bank of sense amplifiers for the data readout;
- a 32 cells output FIFO;
- the control logic.

In the 32 cells output FIFO the Single Event Upset tolerance is implemented by 37 D-type Flip-Flops in order to obtain a single error correction Hamming encoding.

Data are finally transmitted in frames that contain all the data received by the chip during a single timestamp counter cycle. Frames are composed of 40-bit words with a 2-bit header to be able to distinguish a data word, a header word or a trailer word (Fig. 4.8).

- the *header word* contains 12 bits for the chip address, 8 bits for the frame counter, 12 bits are not used and 6 bits for the Error Correction Code.
- the *data word* contains 14 bits for the pixel address, 12 bits for the leading edge time information and 12 bits for the trailing edge ones.
- the *trailer word* contains 16 bits for the number of events, 16 bits for the Cyclic Redundant Check and 6 bits for the Error Correction Code.

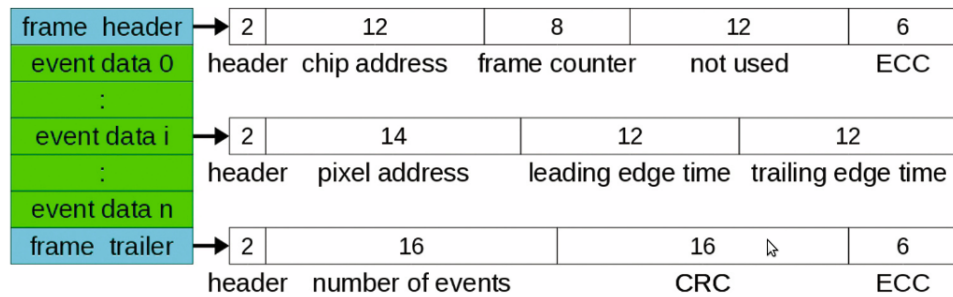


Figure 4.8: Frame structure [5]

4.2.2 ToPix 2.0

This version presents almost the same features of the version presented before (3.0). It has the same technology but different metal stack, presented in table 4.2. For each pixel there are two 12-bits data registers for leading and trailing edge time measurement (as ToPix 3.0) and a 12-bits configuration register (instead of 8-bits). The end of column control logic is composed by a synchronous counter for the timestamp distribution and a shift register for configuration upload. The pixel registers are made of latches designed with the Dual Interlocked Cell (DICE) technique in order to have a radiation tolerant prototype.

It is not used in the test for this work, but just to make some comparison with the results.

4.2.3 GBLD v4

It is included in the GBT chip set and it is a laser driver [21]. Its block diagram is an ASIC composed of nMOS differential pairs for laser modulation and of a current sink for laser bias. It is developed in $0.13\text{ }\mu\text{m}$ CMOS technology and it has the metal layers placed as shown in the first column of the Table 4.2. The laser modulation and the bias current are programmable. There is also a programmable pre-emphasis to optimize the system response. The ASIC is programmable via hardwired pins or via an I²C interface. Serial programmed settings are

Layer	Density [g/cm ³]	Depth [μm]	Layer	Density [g/cm ³]	Depth [μm]
<i>Polymid</i>	1.43	2.50	<i>Polymid</i>	1.43	5.20
<i>Si₃N₄</i>	3.44	0.40	<i>Si₃N₄</i>	3.44	0.40
<i>SiO₂</i>	2.32	1.35	<i>Al</i>	2.70	1.27
<i>Al</i>	2.70	4.00	<i>SiO₂</i>	2.32	0.45
<i>SiO₂</i>	2.32	4.00	<i>Si₃N₄</i>	3.44	0.07
<i>Cu</i>	8.92	3.00	<i>Cu</i>	8.92	0.55
<i>SiO₂</i>	2.32	4.00	<i>SiO₂</i>	2.32	0.65
<i>Al</i>	2.70	0.46	<i>Cu</i>	8.92	0.55
<i>SiO₂</i>	2.32	1.40	<i>SiO₂</i>	2.32	0.65
<i>Cu</i>	8.92	0.55	<i>Cu</i>	8.92	0.32
<i>SiO₂</i>	2.32	0.65	<i>SiO₂</i>	2.32	0.35
<i>Cu</i>	8.92	0.55	<i>Cu</i>	8.92	0.31
<i>SiO₂</i>	2.32	0.65	<i>SiO₂</i>	2.32	0.35
<i>Cu</i>	8.92	0.32	<i>Cu</i>	8.92	0.32
<i>SiO₂</i>	2.32	0.35	<i>SiO₂</i>	2.32	0.35
<i>Cu</i>	8.92	0.32	<i>Cu</i>	8.92	0.32
<i>SiO₂</i>	2.32	0.35	<i>SiO₂</i>	2.32	0.35
<i>Cu</i>	8.92	0.29	<i>Cu</i>	8.92	0.32
<i>SiO₂</i>	2.32	0.35	<i>SiO₂</i>	2.32	0.35
			<i>Cu</i>	8.92	0.29

Table 4.2: Left: Scheme of the metal layers used in ToPix_v3 and GBLD_v4 (1st technology). Right: Scheme of the metal layers used in ToPix_v2 and GBLD_v5 (2nd technology)

stored in the configuration register. It contains a "configuration select" bit in order to choose if the configuration needs to be taken from the pins or from the configuration register. The GBLD contains an I₂C slave with fixed slave address 1111110(bin). It contains 8-bit configuration register each defined by an individual internal address:

- *Control Register*: it is the one that enables the laser diode bias and the modulation current and also if the settings are taken from the internal registers or from the external pins;
- *Modulation Current Register*: it controls the modulation current and the pre/de-emphasis pulse time via a 6 or 2 bits DAC respectively;
- *Bias Current Register*: it controls the laser bias current by an 8-bits DAC;
- *Pre-emphasis Register*: it controls the rising and the falling edge emphasis current with two 4-bits DAC;
- *Modulation Mask Register*: it protects the laser diode against the excessive modulation current;
- *Bias Mask Register*: it protects the laser diode against the excessive bias current;
- *Predriver Register*: It controls the bias current of the predriver stage.

The radiation tolerance structure in these registers is made by a Triple Modular Redundancy protection with D-type Flip-Flops.

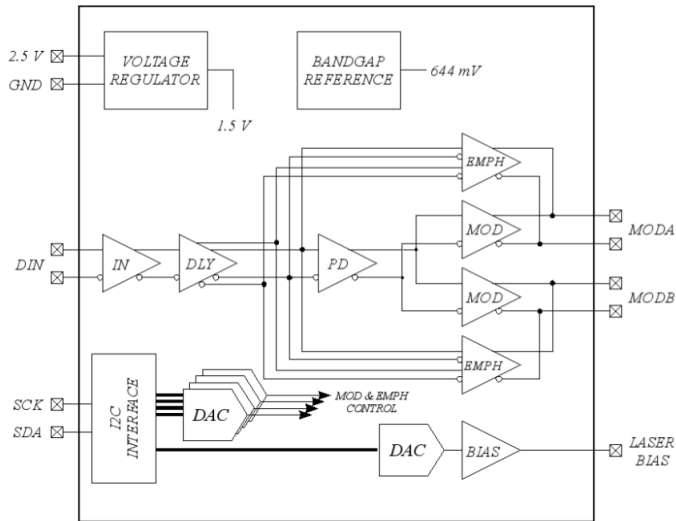


Figure 4.9: GBLD simplified block diagram

4.2.4 GBLD v5

It presents the same functionality of the version 4 [22]. It is composed by six main blocks: modulator, laser bias current generator, control DACs, bandgap reference circuit, voltage regulator, I₂C control logic circuit.

The main difference, relevant for this work, is represented by the material stack used in this technology. It is shown in table 4.2. The I2C control logic presents the same seven 8-bit configuration register shown before and the tolerance to SEU is the same TMR.

4.2.5 SEU tolerance architecture

Triple Modular Redundancy (TMR) It is implemented both with latches (ToPix) and with D-type Flip-Flops (GBLD) followed by a majority vote in the 12-bits of the pixel register (data bus) and in the 8-bits of the pixel configuration register. In this last register it is together with an error detection and correction asynchronous circuit, which allows to re-load the correct value in all the latches when an error is detected.

In this system there are three identical logic circuits performing the same process. Their result is then processed by a majority vote to produce a single output. If one of the system fails, the other two can mask the problem. It is a simple AND-OR circuit. If the inputs are x, y, z , the majority gate is $xy + yz + xz$. The output of the majority gate is 0 if two or more input are 0 and is 1, in the same way, if two or more input are 1.

The data registers are readout very often (few μs) and this implies that the probability of a double error in the same data bit is low.

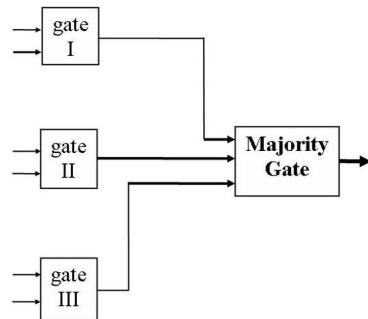


Figure 4.10: Triple Modular Redundancy [19].

Hamming encoding It is used in the column readout logic with 32 cells FIFOs. Every state is defined by a specific bit sequence with error-correcting bits included. They are defined "parity bits". They are introduced choosing to have 3 as minimum Hamming distance between two valid codes. Because two next codes are the same, a failure of the system can occur only when three bit are flipped. If all parity bit are correct there is no error. Otherwise, the sum of the position of the wrong parity bit identifies the error bit. The correction of the SEU is done, in this way, without waiting the next transition of the clock cycle.

DICE It is used in the radiation tolerance architecture for the ToPix 2.0 prototype. The DICE design is an excellent SEU hardness and it is not dependent on optimal transistor sizing. It occupies a smaller space than the triple modular redundancy. Instead of the two inverters that are used in the standard electronics memories, in this architecture the latches are composed

of four inverters. In this way to have a bit upset two circuit nodes must change their value [18]. It has four nodes (A, B, C, D; Fig. 4.11) that store data as two pairs of complementary values [17]. In write and read operations, they are accessed simultaneously through four transistors pass gates. Simultaneous changes of both values in this pair will upset the cell's state and the immunity is lost.

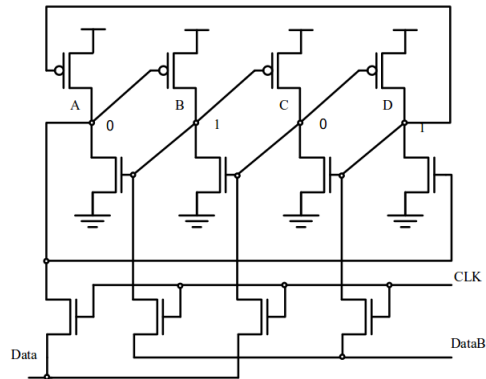


Figure 4.11: The DICE storage cell [17]

4.3 Data Acquisition

During the test beam several ions featuring different energies and at different incident angle of the beam have been used to study the device, as shown in Table 4.3 and 4.4. In this way a wide range of deposited energies can be tested. In order to have a beam aligned with the prototype the quartz is used. In order to have a uniform beam, the eight diodes system is used. Before every run, in case of change of position or ion, a dosimetry run is made to control the flux and the fluence on each diode. After this preparation, the device under study is moved under the beam. ToPix is connected to a Xilinx evaluation board equipped with an FPGA outside from the irradiation chamber, that provides all the controls on the chip. This board is connected to a computer where is controlled by a program developed with the LabView software. Also the GBLD prototypes are tested using a LabView program. All the programs have been developed by Richard Whealon, INFN of Turin.

November		
ToPix_v3		
Ion	Beam Angle	E_inc
	[°]	[MeV]
Br	0 20 30	264.00
Cl	0	196.79
Cl	0 20 30	159.41
F	0 20 30	110.66
O	0	100.91
Ni	0	246.00
Si	0 20 30	146.41

November		
GBLD_v4		
Ion	Beam Angle	E_inc
	[°]	[MeV]
Br	0 20 30	264.00
Cl	0	196.79
Cl	0 20 30	159.41
F	0 20 30	110.66
Ni	0	246.00
Si	0 20 30	146.41

Table 4.3: Ions used in the November's beam test with the corresponding kinetic energy and incident beam angle.

February		
GBLD_v4 GBLD_v5		
Ion	Beam Angle	E_inc
	[°]	[MeV]
Br	0 20	264.00
Cl	0	159.41
F	0 20	110.66
O	0 20	100.91
Ni	0 20	246.00
Si	0 20	146.41

Table 4.4: Ions used in the February's beam test with the corresponding kinetic energy and incident beam angle.

4.3.1 Dosimetry

The dosimetry analysis is necessary in order to know the fluence per cm^2 on the device. The acquisition program is used when all the eight diodes, fixed and mobile, are positioned to be on the beam and also during every run done to test the device. Everytime that the ions are changed or the device under tested has been moved from its position, this program is used in order to know the internal fluence at which the device will be exposed.

In Fig. 4.12 is shown an example of the output file. Every few seconds is reported for each of the eight diodes the flux and the fluence. The diodes are represented by the eight columns:

- the first four represent the external and fixed diodes. They stay in the same position all the time and surround the device under test.
- the second four columns register the mobile diodes. They exchange the place with the device.

During the run when the device is tested also this program runs. It registers only the fixed diodes information and the last columns do not count.

SIRAD Session Manager (RREACT) 0.6.9 Counter logfile							
Flux	Fluence	External Diodes				Internal Diodes	
		Flux	Fluence	Flux	Fluence	Flux	Fluence
21:05:54	Flux: 1.8251e+03	1.6601e+03	2.5201e+03	2.8201e+03	1.5051e+03	1.6951e+03	2.1551e+03
21:05:55	Flux: 1.4900e+03	1.2731e+03	2.1900e+03	2.3250e+03	1.3870e+03	1.5250e+03	1.6820e+03
21:05:56	Flux: 1.8190e+03	1.2081e+03	2.1190e+03	2.1190e+03	1.1890e+03	1.7700e+03	1.8200e+03
21:06:00	Flux: 1.0871e+04	9.1170e+03	1.4376e+04	1.6713e+04	9.9630e+03	1.0762e+04	1.6521e+04
21:06:05	Flux: 1.9649e+03	1.3499e+03	2.3149e+03	2.8049e+03	1.6349e+03	1.8149e+03	2.1499e+03
21:06:05	Flux: 2.0554e+04	1.7072e+04	2.6766e+04	3.1126e+04	1.8922e+04	2.0332e+04	2.3469e+04
21:06:10	Flux: 1.7700e+03	1.3750e+03	2.1550e+03	2.5550e+03	1.5200e+03	1.4250e+03	1.9500e+03
21:06:10	Flux: 3.1103e+04	2.5669e+04	4.0416e+04	4.7047e+04	2.8266e+04	3.0785e+04	3.5440e+04
21:06:16	Flux: 1.8950e+03	1.6100e+03	2.1600e+03	2.1250e+03	1.6850e+03	1.8250e+03	2.2800e+03
21:06:16	Flux: 4.1314e+04	3.4086e+04	5.3468e+04	6.2575e+04	3.7620e+04	4.0691e+04	4.7425e+04
21:06:21	Flux: 2.1250e+03	1.6651e+03	2.9600e+03	3.2250e+03	1.8350e+03	1.9600e+03	2.3350e+03
21:06:21	Flux: 5.1381e+04	4.1200e+04	6.1000e+04	7.0700e+04	5.1000e+04	5.1900e+04	5.8100e+04
21:06:26	Flux: 1.9201e+03	1.5051e+03	2.4351e+03	2.9751e+03	1.7751e+03	2.0051e+03	2.2301e+03
21:06:26	Flux: 6.1936e+04	5.1109e+04	8.0394e+04	9.4058e+04	5.6656e+04	6.0816e+04	7.1498e+04
21:06:32	Flux: 1.6250e+03	1.5100e+03	2.3200e+03	2.7950e+03	1.8600e+03	1.7900e+03	2.0650e+03
21:06:32	Flux: 7.1853e+04	5.9532e+04	9.3574e+04	1.0946e+05	6.6100e+04	7.0830e+04	8.3431e+04
21:06:37	Flux: 2.0450e+03	1.7800e+03	2.9100e+03	3.2550e+03	1.9400e+03	2.0500e+03	2.3550e+03
21:06:37	Flux: 8.2811e+04	6.8775e+04	1.0799e+05	1.2636e+05	7.6084e+04	8.1761e+04	9.6276e+04
21:06:42	Flux: 1.8649e+03	1.4899e+03	2.5799e+03	3.0749e+03	1.7749e+03	2.0499e+03	2.1199e+03
21:06:42	Flux: 9.2077e+04	7.6540e+04	1.2026e+05	1.4065e+05	8.4584e+04	9.1064e+04	1.0708e+05
21:06:48	Flux: 1.5100e+03	1.8699e+03	2.3000e+03	2.7000e+03	2.0000e+03	2.1600e+03	2.1600e+03
21:06:48	Flux: 1.0248e+05	8.1317e+04	1.3417e+05	1.5556e+05	9.4355e+04	1.0447e+05	1.1935e+05
21:06:53	Flux: 1.9350e+03	1.6750e+03	2.5000e+03	2.9800e+03	1.7050e+03	2.1100e+03	2.2350e+03
21:06:53	Flux: 1.1314e+05	9.4411e+04	1.4830e+05	1.7295e+05	1.0423e+05	1.1229e+05	1.3197e+05
21:06:58	Flux: 1.9999e+03	1.5999e+03	2.1349e+03	3.1149e+03	1.9099e+03	1.8899e+03	2.3699e+03
21:06:58	Flux: 1.2303e+05	1.0271e+05	1.6145e+05	1.8815e+05	1.1352e+05	1.2225e+05	1.4371e+05
21:07:04	Flux: 2.0800e+03	1.7250e+03	2.6500e+03	3.1100e+03	1.8600e+03	2.0150e+03	2.4550e+03
21:07:04	Flux: 1.3330e+05	1.1121e+05	1.7478e+05	2.0387e+05	1.2281e+05	1.3242e+05	1.5569e+05
21:07:09	Flux: 1.7450e+03	1.4850e+03	2.5400e+03	2.7700e+03	1.7400e+03	1.9500e+03	2.1300e+03
21:07:09	Flux: 1.4330e+05	1.1900e+05	1.8600e+05	2.1400e+05	1.4700e+05	1.6700e+05	1.9400e+05
21:07:14	Flux: 1.9959e+03	1.6899e+03	2.6499e+03	2.7649e+03	1.9799e+03	2.1399e+03	2.3949e+03
21:07:14	Flux: 1.5332e+05	1.2795e+05	2.0135e+05	2.3462e+05	1.4144e+05	1.5254e+05	1.7919e+05
21:07:20	Flux: 1.8300e+03	1.6500e+03	2.4800e+03	2.8300e+03	1.7800e+03	1.9500e+03	2.4350e+03
21:07:20	Flux: 1.6377e+05	1.3680e+05	2.1493e+05	2.5065e+05	1.5124e+05	1.6299e+05	1.9139e+05
21:07:25	Flux: 1.9200e+03	1.6850e+03	2.6550e+03	2.9900e+03	1.7350e+03	1.9200e+03	2.3250e+03
21:07:25	Flux: 1.7470e+05	1.4570e+05	2.2894e+05	2.6696e+05	1.6115e+05	1.7371e+05	2.0380e+05
21:07:30	Flux: 1.9951e+03	1.8451e+03	2.7151e+03	2.9401e+03	1.8451e+03	2.3301e+03	2.5501e+03
21:07:30	Flux: 1.8559e+05	1.5463e+05	2.4342e+05	2.8345e+05	1.7093e+05	1.8477e+05	2.1661e+05
21:07:36	Flux: 2.0000e+03	1.7300e+03	2.6400e+03	2.9800e+03	1.8850e+03	2.1400e+03	2.4750e+03
21:07:36	Flux: 1.8581e+05	1.6332e+05	2.5600e+05	2.9934e+05	1.8062e+05	1.9152e+05	2.2864e+05
21:07:41	Flux: 1.8849e+03	1.6899e+03	2.4999e+03	2.7299e+03	1.8999e+03	1.7749e+03	2.1399e+03
21:07:41	Flux: 2.0644e+05	1.7226e+05	2.7104e+05	3.1568e+05	1.9053e+05	2.0576e+05	2.4146e+05
21:07:43	Counter: counter stopped						
21:07:43	Counter: elapsed time: 110s						
21:07:43	Counter: estimated central fluence: 244.02500kcts						

Figure 4.12: Example of the output file of the dosimetry program.

4.3.2 ToPix

The acquisition program used to test ToPix is **ToPix_SEU.vi**. The typical output file is presented in Fig.4.13. It is composed of three main parts:

- an *initial part* where are reported the start time of the run and the main parameters setted as the reference event and the clock (set, during the test, at 50.0 MHz).

- an *intermediate part* where are registered and written the information extracted from the comparison of each event with the value stored at the beginning on the run. There are stored:
 - the timing information of the event;
 - the number of error that occurs in the configuration register (*Pixreg errors*);
 - the number of clock cycle when the SEU line was at '1' and the number of times that the same line pass from '0' to '1';
 - the number of transmit event and the number of error that occur in that transmit events for each columns;
 - the transmit event for the four columns;
 - the contents of the data register read for each event (*SEU FIFO counter*).
 - a *final part* where are resumed the errors that occur. At the end, the stop time

- a *final part* where are resumed the errors that occur. At the end, the stop time.

Figure 4.13: Example of the output file of the ToPix acquisition program.

From this file are extracted for this analysis:

- the number presented as the *Pixreg error* as shown in Fig.4.14 in the final part. It refers to the pixel configuration register. As explained before it is readout periodically. If an

error occurs and the event is different from the reference event, it is recorded and the correct value is re-written in the register. The number has been used in order to calculate the cross section directly.

```
-----
Run end
21:10:45.733 02/11/2012
Measurement cycles
1581
Pixreg errors
13663
SEU counter
47159646
SEU edge counter
3628
FIFO bit errors
30794
Average cycle time
2390.7
-----
```

Figure 4.14: Example of the final part of the output file of the ToPix acquisition program.

- the sequences of '1' presented in the intermediate part with the name of *SEU FIFO counter*. This is the register dedicated to the FIFO output with the Hamming decoders. It stores the value of a test signal sent periodically to four pixel at the same time with respect to the internal time stamp counter and with the same input charge. When a wrong code is detected an error signal is generated. These signals are in logical OR and they are sent out by a dedicated output pin. At the end, this acquisition program counts the number of times that the error line goes to 1 and it allows to know the number of errors that occur. In order to calculate the SEU cross section for the data register only the sequences of exactly fourty '1' (Fig. 4.15) have been chosen corresponding to a clock cycle.

Figure 4.15: Example of the *SEU FIFO counter* from the intermediate part of the output file of the ToPix acquisition program.

4.3.3 GBLD

The acquisition system for this prototype is composed of two programs. For the analysis only one has been used. It is the one that gives information on SEU errors on the I2C register. On the top of the output file shown in Fig. 4.16 there are indicated the run start time and the reference value of each 8-bits configuration register. The register has some default value setted, but during the run there is a specific 8-bits sequence to compare with the event ones. Every time that the sequence of one register in a specific event is different from the initial one, an error occurs in that register. The time and the value of each register are written and reported as shown. To calculate the SEU cross section just the final number of total error is considered. It is the sum of time that an error occurs.

In the February test a further analysis has been made. A specific analysis on the errors on each bit is made for all the registers. Every sequence of bit has been compared with the initial one setted at the start of the run and also with the default sequence, corresponding to a reset of the register. This reset circuit, connected with the three Flip-Flops, is not SEU tolerant and an error involves each register separately.

```

Log start 12:51 05/11/2012
Registers written: 10000100 00011111 10101010 10101010 10101010 10101010 00000101
-----
Error 12:52 05/11/2012
Registers read: 10000100 00011111 10101010 10101010 00101010 10101010 00000101
Error 12:55 05/11/2012
Registers read: 00000000 00000000 00000000 00000000 00000000 00000000 00000000
Error 13:11 05/11/2012
Registers read: 11000100 00011111 10101010 10101010 10101010 10101010 00000101
Error 13:12 05/11/2012
Registers read: 10000100 00011111 10101000 10101010 10101010 10101010 00000101
Error 13:19 05/11/2012
Registers read: 10000100 00011111 00101010 10101010 10101010 10101010 00000101
Error 13:24 05/11/2012
Registers read: 10000111 00011111 10101010 10101010 11101010 10101010 00000101
Error 13:25 05/11/2012
Registers read: 10000100 00011111 10101010 10101010 00101010 10101010 00000101
Error 13:25 05/11/2012
Registers read: 10000100 00011111 10101010 00101010 10101010 10101010 00000101
Error 13:30 05/11/2012
Registers read: 10000100 10011111 10101010 10101010 10101010 10101010 00000101
Error 13:30 05/11/2012
Registers read: 10000100 00011111 10111010 10101010 10101010 10101010 00000101
Error 13:38 05/11/2012
Registers read: 00000000 00000000 00000000 00000000 00000000 00000000 00000000
Error 13:38 05/11/2012
Registers read: 10000100 00011111 10101000 10101010 10101010 10101010 00000101
Error 13:40 05/11/2012
Registers read: 10000100 00011111 00101010 10101010 10101010 10101010 00000101
Error 13:41 05/11/2012
Registers read: 10000100 00011111 10101010 10101010 10101010 10100010 00000101
Error 13:43 05/11/2012
Registers read: 10000100 00011111 10101010 10101010 10101010 10101011 00000101
Error 13:45 05/11/2012
Registers read: 10000100 00011111 10101010 00101010 10101010 10101010 00000101
Log end 13:51 05/11/2012
Total errors 16

```

Figure 4.16: Example of the output file of the GBLD acquisition program.

4.3.4 SRIM (Stopping and Range of Ions in Materials)



Figure 4.17: Example of the SRIM interface.

The software package SRIM, provided from the SIRAD staff, has been used to know the ions features of their transport in matter. It is a Monte Carlo simulation code that allows the calculation of ion deposition profiles in materials exposed to energetic ions beam. In Fig.4.17 is

shown the program interface and in Fig.4.18 an example of the output file where information on the energy deposited or the range can be extracted.

```
=====
Calculation using SRIM-2006
SRIM version ---> SRIM-2008.04
Calc. date ---> October 29, 2013
=====

Disk File Name = SRIM outputs\chlorine in silicon
Ion = Chlorine [17] , Mass = 34.969 amu
Target Density = 2.3212E+00 g/cm3 = 4.9770E+22 atoms/cm3
===== Target Composition =====
Atom Atom Atomic Mass
Name Numb Percent Percent
Si 14 100.00 100.00 |
=====

Bragg Correction = 0.00%
Stopping Units = Mev / (mg/cm2)
See bottom of Table for other stopping units



| Ion Energy | dE/dx<br>Elec. | dE/dx<br>Nuclear | Projected Range | Longitudinal straggling | Lateral straggling |
|------------|----------------|------------------|-----------------|-------------------------|--------------------|
| 159.00 Mev | 1.308E+01      | 9.858E-03        | 45.70 um        | 1.39 um                 | 7268 A             |



Multiply stopping by for stopping units
-----
2.3211E+01 ev / Angstrom
2.3211E+02 kev / micron
2.3211E+02 Mev / mm
1.0000E+00 kev / (ug/cm2)
1.0000E+00 Mev / (mg/cm2)
1.0000E+03 kev / (mg/cm2)
4.6637E+01 ev / (1E15 atoms/cm2)
1.4717E-01 L.S.S. reduced units
=====

(C) 1984,1989,1992,1998,2008 by J.P. Biersack and J.F. Ziegler
```

Figure 4.18: Example of the SRIM output file.

4.4 Analysis

4.4.1 Energy deposition

As mentioned before ToPix_3.0 and GBLD_v4 have a different technology from ToPix_2.0 and GBLD_v5 (Table 4.2). This difference makes necessary some analysis on the ions range in the silicon after passing through all the listed materials. In Table 4.5 there are shown:

1. The ions range in ToPix_2.0 during its test;
2. The ions range in ToPix_3.0 and GBLD_v4 with the new energies used in the test;
3. The new ions range in ToPix_2.0 and GBLD_v5 with the new energies.

They have been calculated considering the worst case when the incident particle crosses all the layers.

1_ ToPix_v2		
Ion	E_inc	Range in Si
	[MeV]	[μm]
Br	214.66	11.61
Ni	229.9	20.63
Cl	159.41	27.92
F	110.66	65.34
Si	146.41	38.18
O	100.91	78.42

2_ ToPix_v3		
Ion	E_inc	Range in Si
	[MeV]	[μm]
Br	264.00	0.52
Ni	246.00	5.79
Cl	159.41	11.13
F	110.66	48.26
Si	146.41	21.37
O	100.91	61.23

3_ ToPix_v2		
Ion	E_inc	Range in Si
	[MeV]	[μm]
Br	264.00	16.9
Ni	246.00	23.04
Cl	159.41	27.92
F	110.66	65.34
Si	146.41	38.18
O	100.91	78.42

Table 4.5: Range for several ions in different technologies

As it is shown, in particular for Br and Ni, the energy should be higher in order to have an higher range in Si. It is calculated that, in order to equal the range in Si of the ToPix 2.0 tests, the energy should be 385 MeV for Br and 350 for Ni. Unfortunately the limited voltage of the Tandem (15 MV) together with the necessity to have an high probable charge state (q_1 and q_2) do not allow to reach the needed energy.

4.4.2 Dosimetry

For each run are calculated considering all the correction numbers:

- the *internal fluence*. From the dosimetry file, written with all the eight diodes on the beam, it is calculated the ratio between the fluence of the external diodes and the internal ones.

$$F_{internal} = \frac{\sum F_{internal\ diodes}}{\sum F_{external\ diodes}}$$

- the *fluence of the run*. It is considered only the fluence calculated on the run time.

$$F_{run} = F_{stop} - F_{start}$$

- the *angle correction*. It is calculated as $\cos \theta$ where θ is the incident angle of the beam.

$$\cos \theta$$

- the *diodes correction*. It is a correction factor necessary because during the test of November diodes of different dimensions have been used.

$$C_{diodes}$$

For each run of the same ion at the same incident angle the fluence per cm^2 is calculated as:

$$Fluence = F_{internal} \cdot F_{run} \cdot \cos(\theta) \cdot C_{diodes}$$

4.4.3 SEU

SEU error is estimated by its probability to occur on the device.

The *SEU cross section* is defined as:

$$\sigma_{SEU} = \frac{N_{errors}}{\Phi \cdot N_{bit}}$$

- N_{errors} is the number of SEU that occur in the device.
- Φ is the total incident particle fluence per cm^2 .
- N_{bit} is the number of bits where the SEU error can occur.

The same kind of analysis was made:

- during the November test:
 - ToPix Configuration Register;
 - ToPix Data Register;
 - GBLD_v4 I2C Register;
- during the February test:
 - GBLD_v4 I2C Register;

- GBLD_v5 I2C Register;

For a specific device, all the runs featuring the same ion and incident beam angle are considered to obtain the final *number of errors*. The same sum is made with the *fluence* value. The errors are calculated with the Poisson formula and then summed in quadrature.

The *number of bit* change for each register considered:

- the ToPix Configuration Register: 640 cells for the 8 bits register;
- the ToPix Data Register: 32 cells for 38 bits register for 4 column;
- the GBLD_v4 and the GBLD_v5 I2C Register: 7 bins for 8 bits.

The SEU Cross Section calculated for each ion is shown in Table 4.6, 4.7, 4.8, 4.9 and 4.10.

These points are fit by the Weibull function with respect to the LET (Linear Energy Transfer):

$$\sigma = \sigma_0 \left[1 - e^{-\left(\frac{LET - LET_{th}}{W} \right)^s} \right]$$

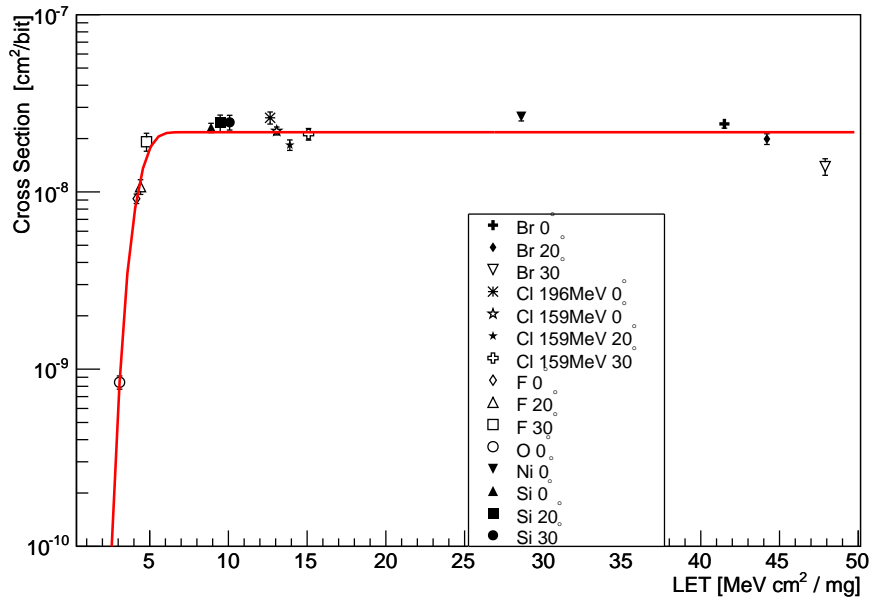
- W is a scale parameter;
- s is a shape parameter. It is called *Weibull modulus* and indicates the strength of the material. It is fixed at 3 to allow the fit to follow the increasing of the cross section with the LET;
- σ_0 is the maximum probability to have a SEU;
- LET_{th} is the threshold of the energy transferred that can cause an upset.

The fits are shown separately for each prototype tested.

November's test

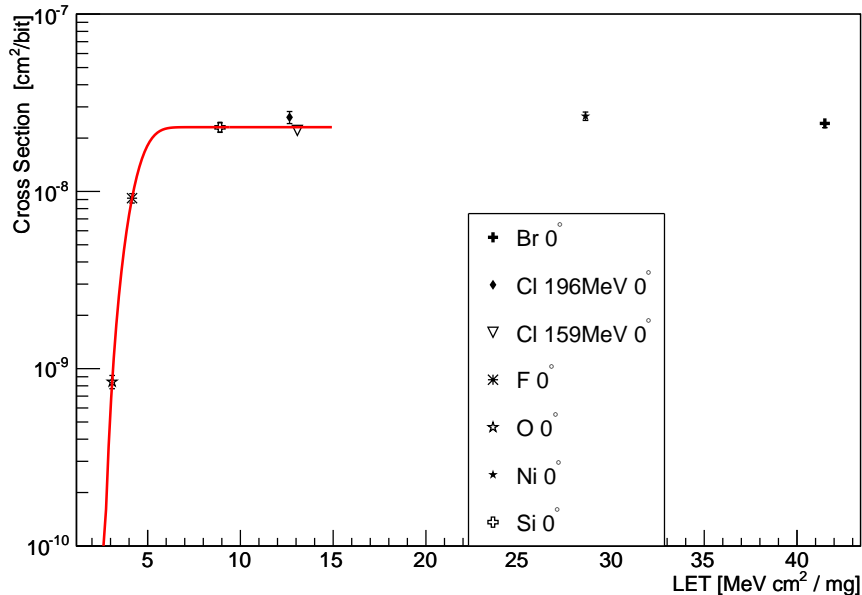
ToPix Configuration Register The fit with all the data collected is shown in of Fig.4.19a.

It can be highlighted that the cross section for the *Br* ion decreases as a function of the incident angle. This trend indicates that the ion's energy is not sufficient to reach the Silicon layer. Then a second fit was done limiting to zero the beam incident angle of all ions and excluding also the data of *Br* and *Ni*, the ions with less range in *Si* as presented before (Fig.4.19b). In this case, the data are well fitted by this Weibull function.



(a)

$$\begin{aligned}
 LET_{th} &= (2.31 \pm 0.05) \text{ MeV cm}^2 / \text{mg} \\
 \sigma_0 &= (2.173 \cdot 10^{-8} \pm 4.5 \cdot 10^{-10}) \text{ cm}^2 / \text{bit} \\
 W &= (2.27 \pm 0.09) \text{ MeV} \\
 \chi/\text{dof} &= 63.60/12
 \end{aligned}$$



(b)

$$\begin{aligned}
 LET_{th} &= (2.32 \pm 0.05) \text{ MeV cm}^2 / \text{mg} \\
 \sigma_0 &= (2.305 \cdot 10^{-8} \pm 8.1 \cdot 10^{-10}) \text{ cm}^2 / \text{bit} \\
 W &= (2.31 \pm 0.12) \text{ MeV} \\
 \chi/\text{dof} &= 3.05/4
 \end{aligned}$$

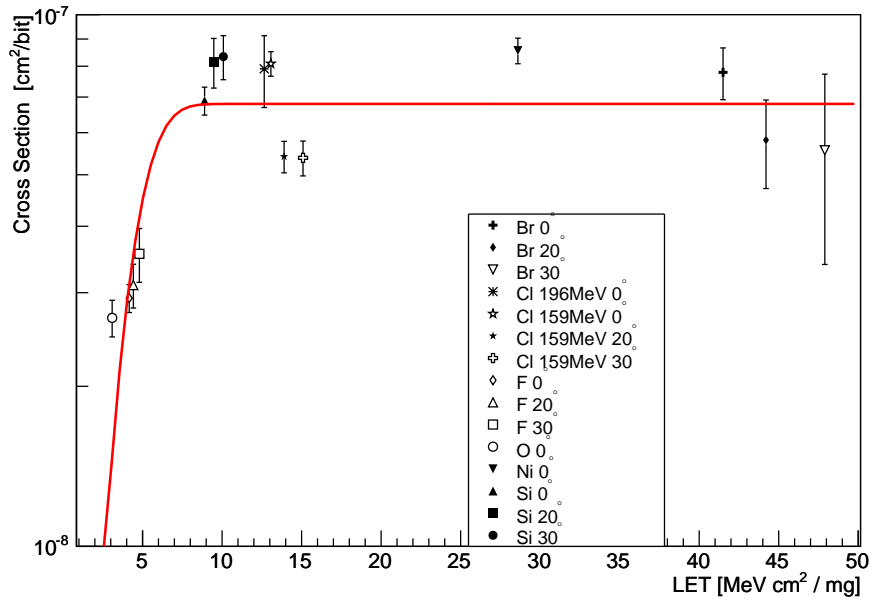
Figure 4.19: ToPix 3.0 Configuration Register. (a): Fit of all the experimental data. (b): Fit of the experimental data with beam incident angle 0° , excluding the Br and Ni .

November				
ToPix Configuration Register				
Ion	Beam Angle °	LET [MeV cm ² / mg]	σ_{SEU} [cm ² /bit]	$\delta\sigma_{SEU}$ [cm ² /bit]
Br (264.00 MeV)	0	41.5	$2.42 \cdot 10^{-8}$	$1.30 \cdot 10^{-9}$
	20	44.2	$1.99 \cdot 10^{-8}$	$1.38 \cdot 10^{-9}$
	30	47.9	$1.39 \cdot 10^{-8}$	$1.49 \cdot 10^{-9}$
Cl (196.79 MeV)	0	12.65	$2.62 \cdot 10^{-8}$	$2.05 \cdot 10^{-9}$
Cl (159.41 MeV)	0	13.89	$2.21 \cdot 10^{-8}$	$1.14 \cdot 10^{-9}$
	20	14.78	$1.84 \cdot 10^{-8}$	$1.25 \cdot 10^{-9}$
	30	16.04	$2.12 \cdot 10^{-8}$	$1.60 \cdot 10^{-9}$
F (110.66 MeV)	0	4.16	$9.16 \cdot 10^{-9}$	$5.58 \cdot 10^{-10}$
	20	4.42	$1.07 \cdot 10^{-8}$	$1.02 \cdot 10^{-9}$
	30	4.80	$1.92 \cdot 10^{-8}$	$2.23 \cdot 10^{-9}$
O (100.91 MeV)	0	3.09	$8.43 \cdot 10^{-10}$	$7.23 \cdot 10^{-11}$
Ni (246.00 MeV)	0	28.6	$2.66 \cdot 10^{-8}$	$1.45 \cdot 10^{-9}$
Si (146.41 Mev)	0	8.90	$2.30 \cdot 10^{-8}$	$1.39 \cdot 10^{-9}$
	20	9.48	$2.45 \cdot 10^{-8}$	$2.63 \cdot 10^{-9}$
	30	10.08	$2.47 \cdot 10^{-8}$	$2.35 \cdot 10^{-9}$

Table 4.6: SEU Cross Section of ToPix 3.0 Configuration Register on November's test

ToPix Data Register The fit with all the data collected is shown in Fig.4.20a. Also in this case, the data are not satisfactorily fitted. The same problem occurs: some ions do not have enough energy to reach the *Si*.

The same scheme of before is used: a new fit is done choosing the data with the beam incident angle at zero, excluding the data of *Br* and *Ni* (Fig.4.20b). An imposition on the fit program for the positive threshold is included.



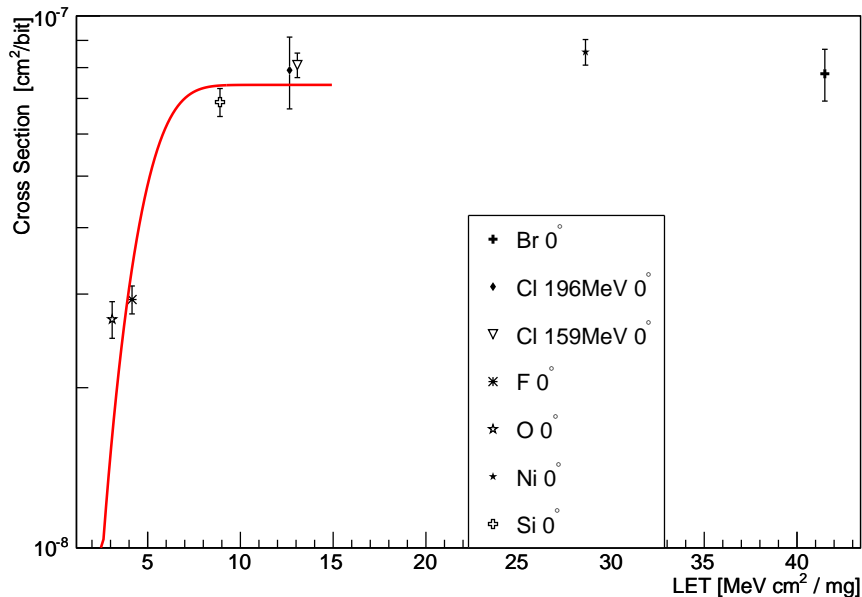
(a)

$$LET_{th} = (0.1 \pm 0.046) \text{ MeV cm}^2 / \text{mg}$$

$$\sigma_0 = (6.79 \cdot 10^{-8} \pm 1.7 \cdot 10^{-9}) \text{ cm}^2/\text{bit}$$

$$W = (4.8 \pm 0.1) \text{ MeV}$$

$$\chi/\text{dof} = 97.15/12$$



(b)

$$LET_{th} = (1.6 \cdot 10^{-9} \pm 0.06) \text{ MeV cm}^2 / \text{mg}$$

$$\sigma_0 = (7.42 \cdot 10^{-8} \pm 2.9 \cdot 10^{-9}) \text{ cm}^2/\text{bit}$$

$$W = (4.9 \pm 0.1) \text{ MeV}$$

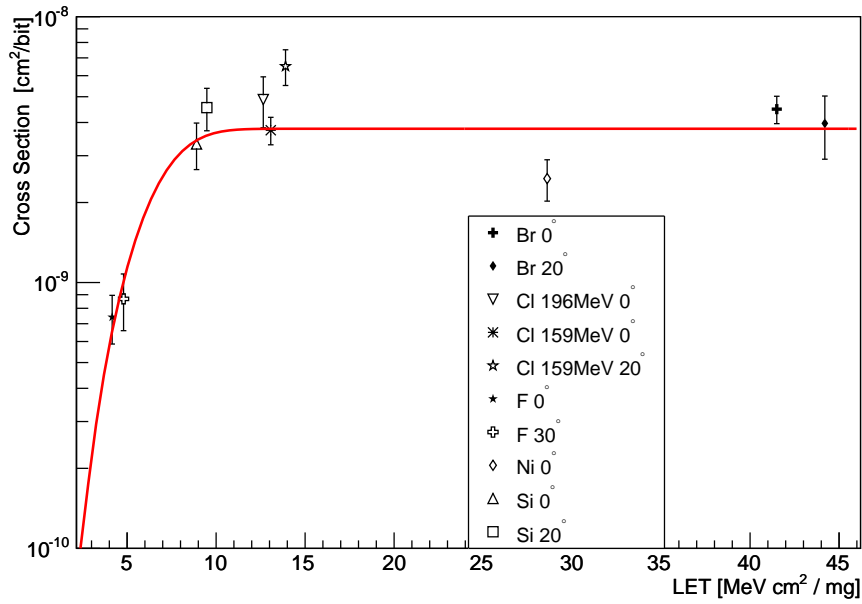
$$\chi/\text{dof} = 35.07/4$$

Figure 4.20: ToPix 3.0 Data Register. a): Fit of all the experimental data. (b): Fit of the experimental data with beam incident angle 0°, excluding the Br and Ni.

November				
ToPix Data Register				
Ion	Beam Angle °	LET [MeV cm ² / mg]	σ_{SEU} [cm ² /bit]	$\delta\sigma_{SEU}$ [cm ² /bit]
Br (264.00 MeV)	0	41.5	$7.79 \cdot 10^{-8}$	$8.70 \cdot 10^{-9}$
	20	44.2	$5.81 \cdot 10^{-8}$	$1.09 \cdot 10^{-8}$
	30	47.9	$5.56 \cdot 10^{-8}$	$2.17 \cdot 10^{-8}$
Cl (196.79 MeV)	0	12.65	$7.91 \cdot 10^{-8}$	$1.22 \cdot 10^{-8}$
Cl (159.41 MeV)	0	13.89	$8.09 \cdot 10^{-8}$	$4.29 \cdot 10^{-9}$
	20	14.78	$5.41 \cdot 10^{-8}$	$3.67 \cdot 10^{-9}$
	30	16.04	$5.38 \cdot 10^{-8}$	$4.05 \cdot 10^{-9}$
F (110.66 MeV)	0	4.16	$2.93 \cdot 10^{-8}$	$1.77 \cdot 10^{-9}$
	20	4.42	$3.10 \cdot 10^{-8}$	$2.93 \cdot 10^{-9}$
	30	4.80	$3.55 \cdot 10^{-8}$	$4.12 \cdot 10^{-9}$
O (100.91 MeV)	0	3.09	$2.69 \cdot 10^{-8}$	$2.13 \cdot 10^{-9}$
Ni (246.00 MeV)	0	28.6	$8.56 \cdot 10^{-8}$	$4.74 \cdot 10^{-9}$
Si (146.41 Mev)	0	8.90	$6.89 \cdot 10^{-8}$	$4.17 \cdot 10^{-9}$
	20	9.48	$8.14 \cdot 10^{-8}$	$8.73 \cdot 10^{-9}$
	30	10.08	$8.34 \cdot 10^{-8}$	$7.94 \cdot 10^{-9}$

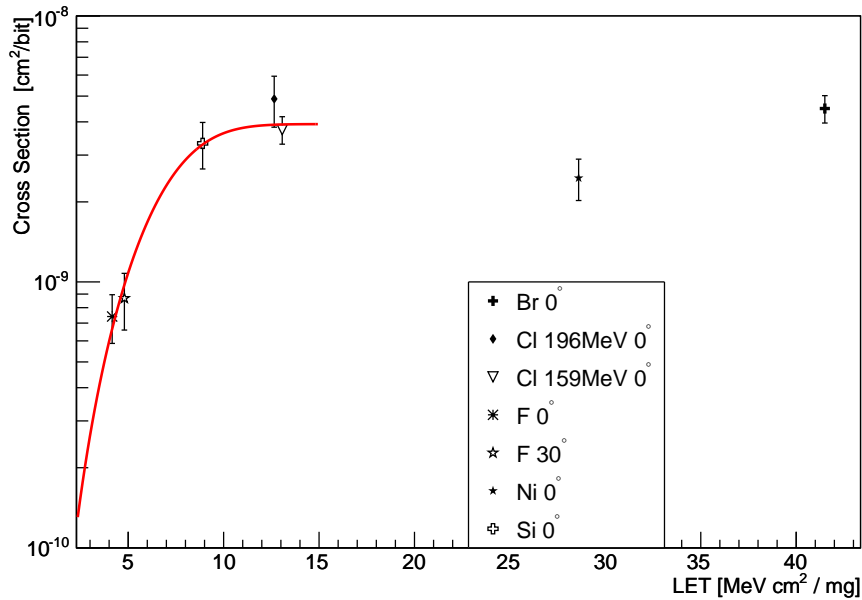
Table 4.7: SEU Cross Section of ToPix 3.0 Data Register on November's test

GBLD I2C Register All the data collected are fitted in Fig. 4.21a. As before, a second fit was done limiting data with incident angle at zero, excluding the data of *Br* and *Ni* and including the *F* at 30° (Fig. 4.21b). The same imposition on the LET_{th} parameter is done.



(a)

$$\begin{aligned}LET_{th} &= (0.5 \pm 2.2) \text{ MeV cm}^2/\text{mg} \\ \sigma_0 &= (3.79 \cdot 10^{-9} \pm 2.3 \cdot 10^{-10}) \text{ cm}^2/\text{bit} \\ W &= (6.3 \pm 1.7) \text{ MeV} \\ \chi/\text{dof} &= 21.75/7\end{aligned}$$



(b)

$$\begin{aligned}LET_{th} &= (5.4 \cdot 10^{-7} \pm 2.6) \text{ MeV cm}^2/\text{mg} \\ \sigma_0 &= (3.92 \cdot 10^{-9} \pm 4.0 \cdot 10^{-10}) \text{ cm}^2/\text{bit} \\ W &= (7.3 \pm 0.5) \text{ MeV} \\ \chi/\text{dof} &= 1.50/4\end{aligned}$$

Figure 4.21: GBLD I2C Register. (a): Fit to all the experimental data. (b): Fit to the experimental data with beam incident angle 0° , excluding the Br and Ni and including $\text{F}(30^\circ)$.

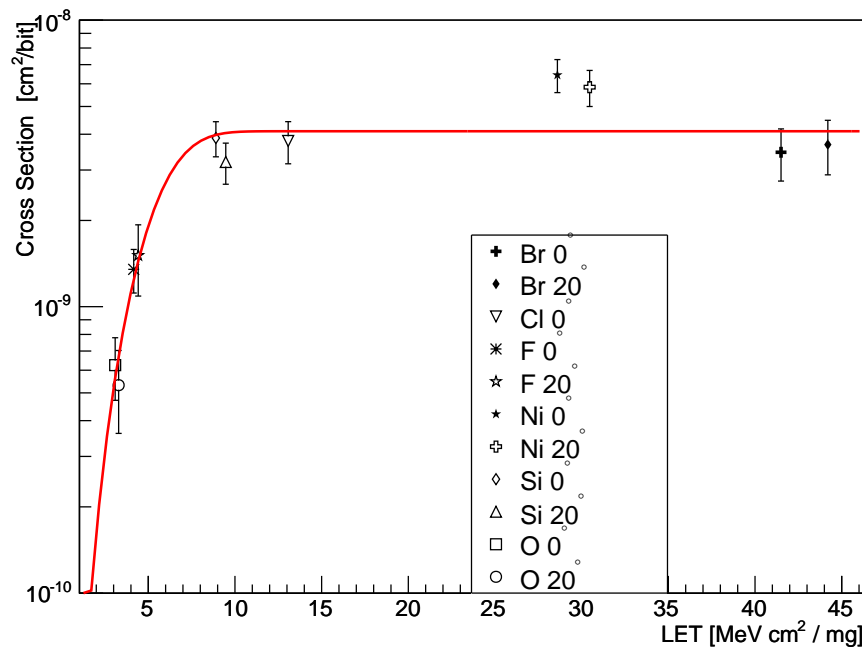
November				
GBLD I2C Register				
Ion	Beam Angle °	LET [MeV cm ² / mg]	σ_{SEU} [cm ² /bit]	$\delta\sigma_{SEU}$ [cm ² /bit]
Br (264.00 MeV)	0	41.5	$4.49 \cdot 10^{-9}$	$5.30 \cdot 10^{-10}$
	20	44.2	$3.97 \cdot 10^{-9}$	$1.06 \cdot 10^{-9}$
Cl (196.79 MeV)	0	12.65	$4.88 \cdot 10^{-9}$	$1.06 \cdot 10^{-9}$
Cl (159.41 MeV)	0	13.89	$3.74 \cdot 10^{-9}$	$4.43 \cdot 10^{-10}$
	20	14.78	$6.51 \cdot 10^{-9}$	$9.99 \cdot 10^{-10}$
F (110.66 MeV)	0	4.16	$7.41 \cdot 10^{-10}$	$1.54 \cdot 10^{-10}$
	20	4.42	$2.20 \cdot 10^{-10}$	$2.22 \cdot 10^{-10}$
	30	4.80	$8.68 \cdot 10^{-10}$	$2.09 \cdot 10^{-10}$
Ni (246.00 MeV)	0	28.6	$2.46 \cdot 10^{-9}$	$4.36 \cdot 10^{-10}$
Si (146.41 Mev)	0	8.90	$3.32 \cdot 10^{-9}$	$6.60 \cdot 10^{-10}$
	20	9.48	$4.55 \cdot 10^{-9}$	$8.27 \cdot 10^{-10}$

Table 4.8: SEU Cross Section of GBLD I2C Register on November's test

February's test

GBLD_v4 I2C Register Two different fits are made for this register 56-bits long (made of 7 bins of 8 bits), like in the other analyses. A first fit is made with all the data. A second fit is made only with the data corresponding 0° and excluding the data of *Br* and *Ni*. They are represented in Fig. 4.22.

In addition, the SEU cross section corresponding to the bit errors of each bin is calculated. It was observed that sometimes the bit values of one or more bins (each of 8-bits) go back to the default information. This fact corresponds to a reset of these bins (the reset signal controls the 3 Flip-Flops of the TMR circuits of each bins). It has been considered because the reset circuit is not protected from SEU. The number of errors was evaluated to be the 50% of the total observed bit upsets.



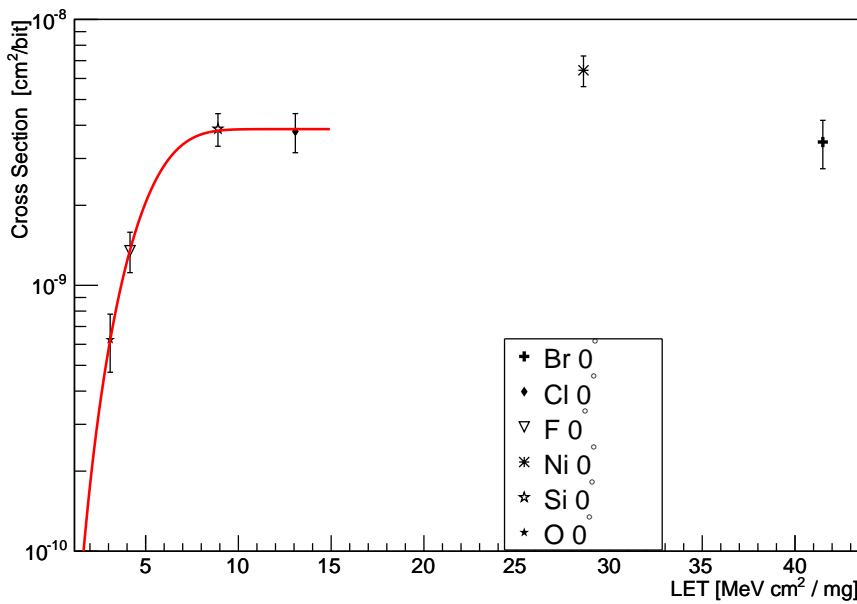
(a)

$$LET_{th} = (9.06 \cdot 10^{-7} \pm 2.7) \text{ MeV cm}^2/\text{mg}$$

$$\sigma_0 = (4.09 \cdot 10^{-9} \pm 2.7 \cdot 10^{-10}) \text{ cm}^2/\text{bit}$$

$$W = (5.8 \pm 0.8) \text{ MeV}$$

$$\chi/\text{dof} = 16.84/8$$



(b)

$$LET_{th} = (0.04 \pm 2.8) \text{ MeV cm}^2/\text{mg}$$

$$\sigma_0 = (3.9 \cdot 10^{-9} \pm 4.4 \cdot 10^{-10}) \text{ cm}^2/\text{bit}$$

$$W = (5.5 \pm 1.9) \text{ MeV}$$

$$\chi/\text{dof} = 0.03/1$$

Figure 4.22: GBLD_v4 I2C Register. (a): Fit of all the experimental data. (b): Fit of the experimental data with beam incident angle 0° and excluding the Br and Ni.

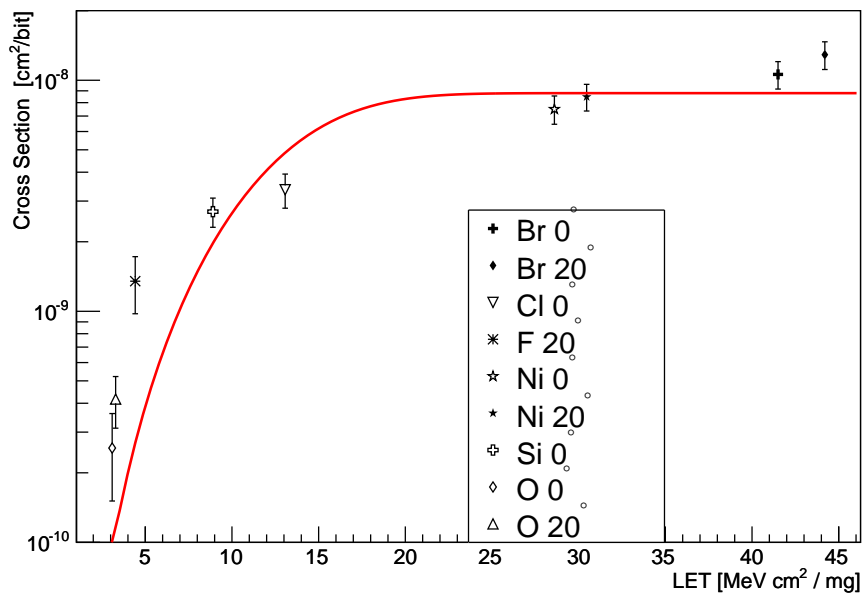
February				
GBLD_v4 I2C Register				
Ion	Beam Angle	LET	σ_{SEU}	$\delta\sigma_{SEU}$
	°	[MeV cm ² / mg]	[cm ² /bit]	[cm ² /bit]
Br (264.00 MeV)	0	41.5	$3.46 \cdot 10^{-9}$	$7.15 \cdot 10^{-10}$
	20	44.2	$3.68 \cdot 10^{-9}$	$7.94 \cdot 10^{-10}$
Cl (159.41 MeV)	0	13.89	$3.79 \cdot 10^{-9}$	$6.36 \cdot 10^{-10}$
F (110.66 MeV)	0	4.16	$1.35 \cdot 10^{-9}$	$2.34 \cdot 10^{-10}$
	20	4.42	$1.51 \cdot 10^{-9}$	$4.21 \cdot 10^{-10}$
Ni (246.00 MeV)	0	28.6	$6.44 \cdot 10^{-9}$	$8.50 \cdot 10^{-10}$
	20	30.46	$5.84 \cdot 10^{-9}$	$8.41 \cdot 10^{-10}$
Si (146.41 Mev)	0	8.90	$3.88 \cdot 10^{-9}$	$5.44 \cdot 10^{-10}$
	20	9.48	$3.20 \cdot 10^{-9}$	$5.24 \cdot 10^{-10}$
O (100.91 Mev)	0	3.09	$6.25 \cdot 10^{-10}$	$1.54 \cdot 10^{-10}$
	20	3.29	$5.32 \cdot 10^{-10}$	$1.71 \cdot 10^{-10}$

Table 4.9: SEU Cross Section of GBLD_v4 I2C Register on February's test

February				
GBLD_v5 I2C Register				
Ion	Beam Angle	LET	σ_{SEU}	$\delta\sigma_{SEU}$
	°	[MeV cm ² / mg]	[cm ² /bit]	[cm ² /bit]
Br (264.00 MeV)	0	41.5	$1.06 \cdot 10^{-8}$	$1.44 \cdot 10^{-9}$
	20	44.2	$1.29 \cdot 10^{-8}$	$1.77 \cdot 10^{-9}$
Cl (159.41 MeV)	0	13.89	$3.36 \cdot 10^{-9}$	$5.66 \cdot 10^{-10}$
F (110.66 MeV)	20	4.42	$1.35 \cdot 10^{-9}$	$3.74 \cdot 10^{-10}$
Ni (246 MeV)	0	28.6	$7.50 \cdot 10^{-9}$	$1.05 \cdot 10^{-10}$
	20	30.46	$8.48 \cdot 10^{-9}$	$1.12 \cdot 10^{-9}$
Si (146.41 Mev)	0	8.90	$2.70 \cdot 10^{-9}$	$3.90 \cdot 10^{-10}$
O (100.91 MeV)	0	3.09	$2.56 \cdot 10^{-10}$	$1.05 \cdot 10^{-10}$
	20	3.29	$7.42 \cdot 10^{-10}$	$7.57 \cdot 10^{-10}$

Table 4.10: SEU Cross Section of GBLD_v5 I2C Register on February's test

GBLD_v5 I2C Register The two fits, done as in the previous analyses, are reported in Fig. 4.23. The first has all the experimental data included and the second has the experimental points measured with the beam incident angle at 0°. A positive LET_{th} is requested. The Reset analysis is done as the one for the GBLD_v4. In this case the number of upsets is the 75% of the total number. This device is more sensitive.



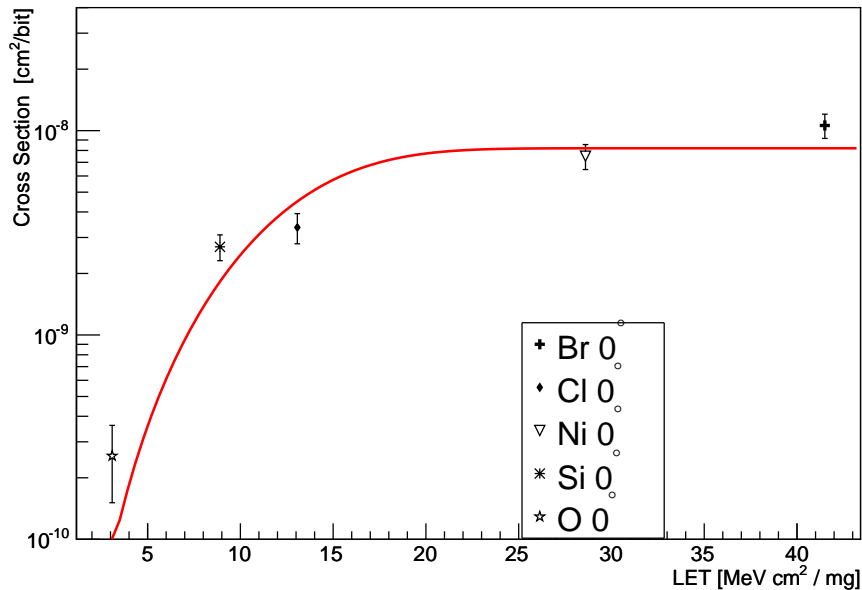
(a)

$$LET_{th} = (1.26 \cdot 10^{-10} \pm 0.1) \text{ MeV cm}^2/\text{mg}$$

$$\sigma_0 = (8.8 \cdot 10^{-9} \pm 6.7 \cdot 10^{-10}) \text{ cm}^2/\text{bit}$$

$$W = (14.1 \pm 0.9) \text{ MeV}$$

$$\chi/\text{dof} = 38.24/6$$



(b)

$$LET_{th} = (3.29 \cdot 10^{-11} \pm 2.5) \text{ MeV cm}^2/\text{mg}$$

$$\sigma_0 = (8.2 \cdot 10^{-9} \pm 9.1 \cdot 10^{-10}) \text{ cm}^2/\text{bit}$$

$$W = (14.1 \pm 1.1) \text{ MeV}$$

$$\chi/\text{dof} = 14.97/1$$

Figure 4.23: GBLD_v5 I2C Register. (a): Fit of all the experimental data. (b): Fit of the experimental data with beam incident angle 0°.

4.4.4 Conclusions

In this work ToPix 3.0, GBLD v4 and GBLD v5 have been tested.

ToPix 3.0 presents, as SEU tolerance architecture, the triple modular redundancy on the configuration register and the Hamming encoding in the data register and has the 1st technology for the metal stack.

The GBLD prototypes present the same triple modular redundancy with D-type Flip-Flops, as architecture to control SEU. The fourth version is made with the same 1st technology of Topix 3.0, instead the fifth have the 2nd metal stack technology.

This 2nd structure is also used in ToPix 2.0, the prototype which has a DICE architecture against SEU. Its test was made in a precedent work and the parameters obtained for the fit shown in Fig. 4.24, are:

- $LET_{th} = 1.87 \pm 0.23$ MeV;
- $\sigma_0 = 1.98 \cdot 10^{-8} \pm 8.9 \cdot 10^{-11}$ cm²/bit;
- $W = 19.25 \pm 0.45$ MeV.

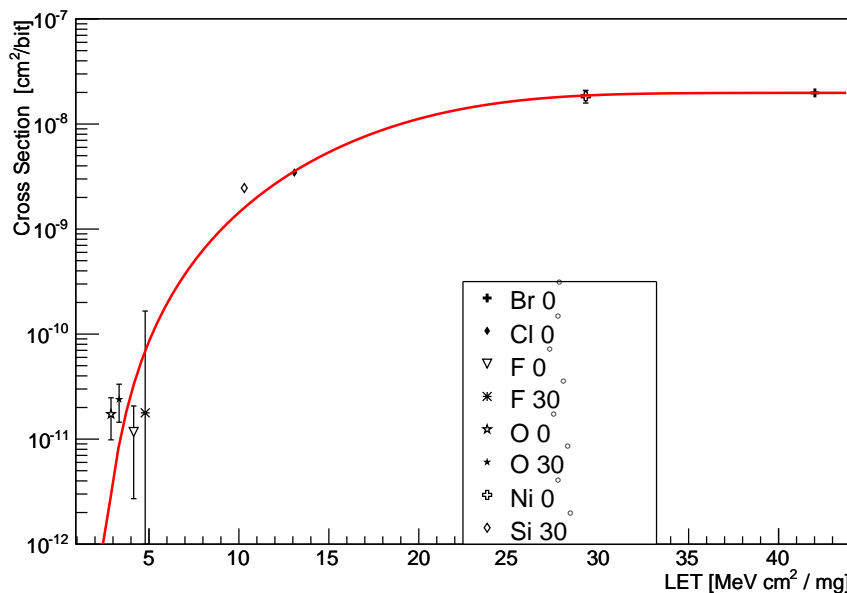


Figure 4.24: Fit of the experimental data of Topix 2.0.

Comparing the two Topix prototypes, it can be observed that the TMR and the DICE cell do not present significant differences in the saturated cross section and in the LET threshold. This can be due to the compact layout imposed by the pixel cells size.

The difference that occurs in these two analyses is in the behaviour when the chip is tilted with respect to the plane orthogonal to the beam line. In Topix 3.0 the cross section of some ions

decreases. This has not been observed in Topix 2.0. The explanation is that there are different metal stack thickness in them. The third version is the one where the thickness is higher. Even if the incident particle can cross any possible combination of the metal layers, in ToPix 3.0 there is the worst situation.

An improvement on the saturated cross section can be observed in the case of the GBLD with respect to the ToPix prototypes, probably due to latches and Flip-Flops circuits.

There is a difference between the two version of the GBLD in the behaviour of the ions but, again, they present different metal layers stacks.

About the threshold of Linear Energy Transfer, the last data taking on the GBLD prototypes, made also with B at 80 MeV and N at 100 MeV (LET 1.13 MeV cm 2 /mg and 2.23 MeV cm 2 /mg respectively), show that no error occurs on the device and the LET threshold is set by the O . This confirms the hypothesis that this parameter need to be set positive. For the ToPix prototype, tests with light ions were not performed due to the limit time of the data taking period. Further analyses could be helpful to understand the correct behaviour of the cross section at low LET.

In the reset analysis for the data from the February's test, for the fifth version, the registers are more sensitive than the fourth version. This reset circuit is now under study.

4.5 SEU rate in the $\bar{\text{P}}\text{ANDA}$ environment

The SEU rate evaluation in the $\bar{\text{P}}\text{ANDA}$ environment is made by combining the results of the analysis of the sensitivity of the circuitry, the simulations, already done [20], for emitted particle distributions in the MVD volume and the expected particle flux. The analysis is made for all the prototypes presented in this work. For the GBLD prototypes this will pose an upper limit to the rate because GBLD will be positioned in the backwards of the MVD volume.

This analysis is divided in two main parts: SEU by hadrons and SEU by leptons.

4.5.1 SEU by hadrons

It is evaluated by:

$$\Sigma = \sum_i P_i \frac{\Delta\sigma_i}{A}$$

- i represents each energy bin;
- $A = 1 \times 1 \mu\text{m}^2$ is the cross-sectional area of the Sensitive Volume (SV);
- P_i is the energy deposition probability. It is shown in Fig. 4.25, for several proton energy, the probability value to deposit a certain amount of energy. The curve of the 200 MeV protons is used for this scope. The hadron in fact can be assimilated to protons and above 200 MeV, the energy deposition probability is independent from the particle energy [14];
- $\Delta\sigma_i$ is the increase of the sensitive area in the energy range $\sigma_{i+1} - \sigma_i$. It is calculated from the Weibull distribution shown in Fig. 4.26 and Fig. 4.27.

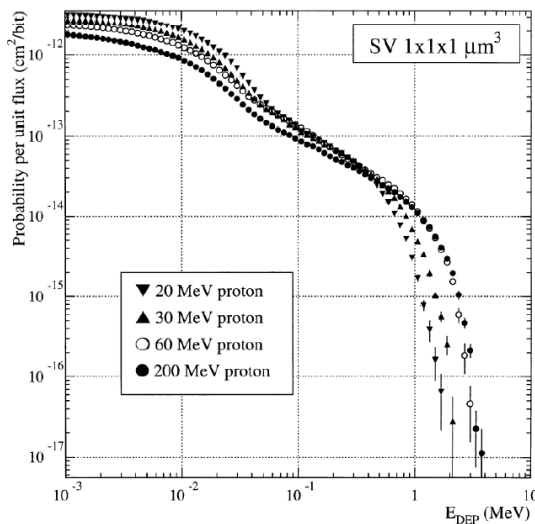


Figure 4.25: Energy deposition probability for protons at different energies. It is shown the probability to have within the SV an ionizing deposition greater or equal to the E_{dep} indicated. [14]

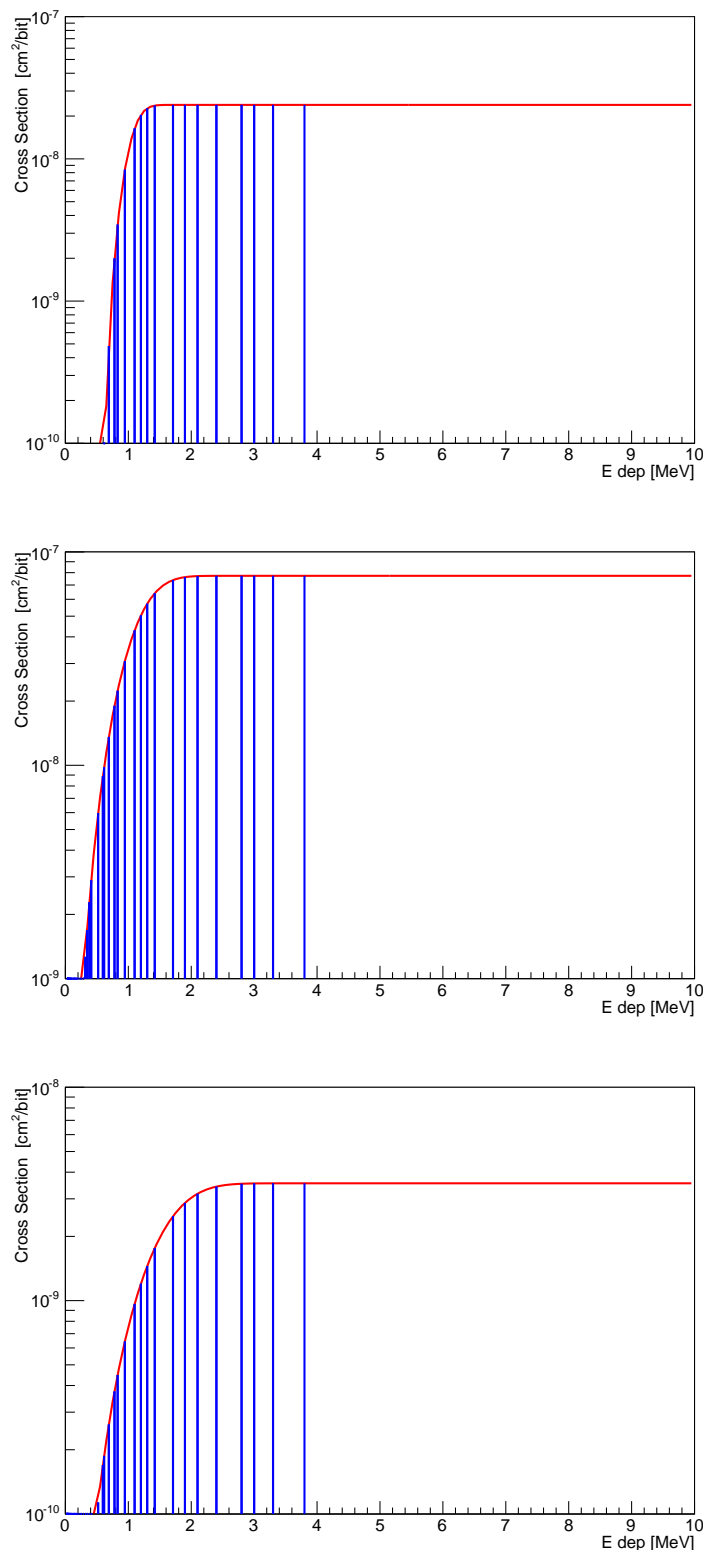


Figure 4.26: Weibull fit and the bins of the convolution values from the November's test. *First:* ToPix 3.0 Configuration Register. *Second:* ToPix 3.0 Data Register. *Third:* GBLD.

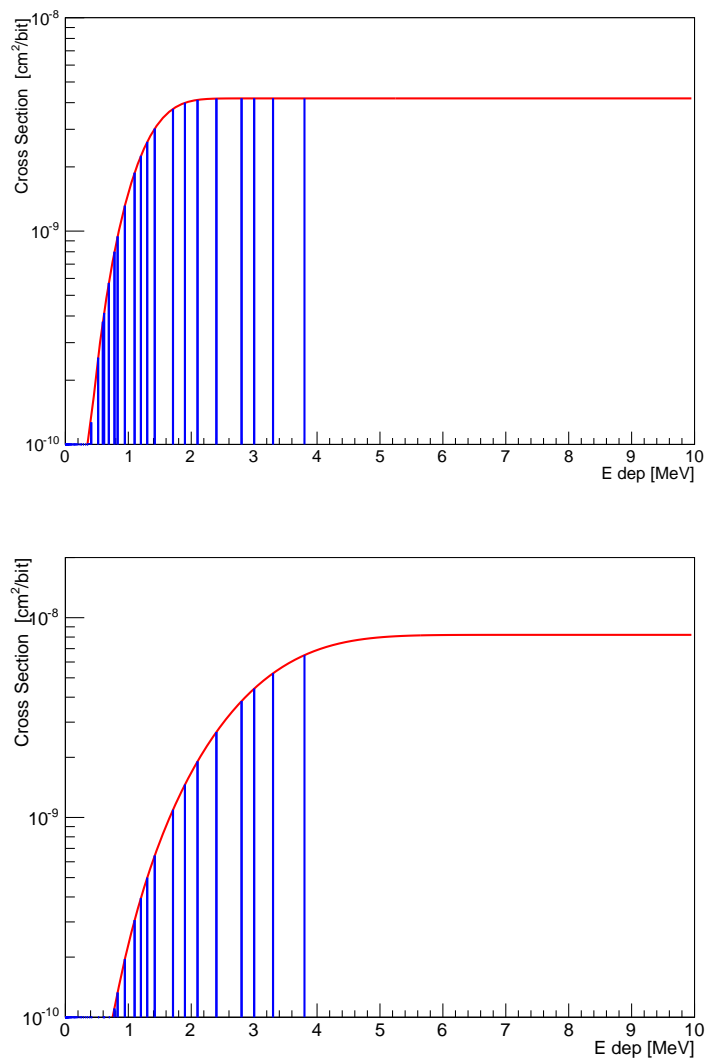


Figure 4.27: Weibull fit of the GBLD in the February's test and the bins of the convolution values. *Left:* GBLD_v4. *Rigth:* GBLD_v5.

November		
ToPix 3.0		GBLD
Configuration Register	Data Register	I2C Register
$4.31 \cdot 10^{-16}$ [cm ² /bit]	$1.51 \cdot 10^{-15}$ [cm ² /bit]	$4.43 \cdot 10^{-17}$ [cm ² /bit]

February		
GBLD_v4	GBLD_v5	
I2C Register	I2C Register	
$7.18 \cdot 10^{-17}$ [cm ² /bit]	$2.33 \cdot 10^{-17}$ [cm ² /bit]	

Table 4.11: Σ in the hadron environment.

The results are summarized in the Table. 4.11. The values are corrected for a 30% factor to take into account the under-estimation of the sensitive volume.

To complete this analysis in Table 4.12 are reported the particle fluxes obtained from simulation of [20].

Hadron [hit/(cm ² s)]	
$\bar{p} - p$	$\bar{p} - Au$
$5 \cdot 10^6$	$16 \cdot 10^6$

Table 4.12: Hadron fluxes foreseen for the $\bar{p} - p$ and the $\bar{p} - Au$ interactions. ($2 \cdot 10^7$ int/sec)

Multiplying the obtained cross section with this value the rate for the $\bar{p} - p$ and the $\bar{p} - Au$ interactions is obtained and shown in Table 4.13.

November		
	ToPix 3.0	GBLD
Interaction	Configuration Register	Data Register
$\bar{p} - p$	$2.16 \cdot 10^{-09}$	$7.55 \cdot 10^{-09}$

February		
	GBLD_v4	GBLD_v5
Interaction	I2C Register	I2C Register
$\bar{p} - p$	$3.59 \cdot 10^{-10}$	$1.16 \cdot 10^{-10}$
$\bar{p} - Au$	$1.15 \cdot 10^{-09}$	$3.72 \cdot 10^{-10}$

Table 4.13: SEU [bit⁻¹ s⁻¹]. *Top*: ToPix and GBLD prototypes from November's test. *Bottom*: GBLD prototypes from February's test.

At the end, for the final ToPix, there are presented in Table 4.14 the results for the SEU rate per hour in each chip. There will be 12760 readout cells with an 8-bits configuration register and 12-bits data register.

November		
ToPix 3.0		
Interaction	Configuration Register	Data Register
$\bar{p} - p$	0.79	13.2
$\bar{p} - Au$	2.54	42.1

Table 4.14: SEU [chip $^{-1}$ h $^{-1}$] for the \bar{p} ANDA environment in the ToPix.

Taking into account the 810 readout chip equipping the pixel part of the MVD the number of compromised readout cells for the configuration register are of the order of $6 \cdot 10^{-5}$ of the total pixel number. The data will be compromised at a $5.79 \cdot 10^{-10}$ level.

4.5.2 SEU by leptons

In this case only the elastic scattering with the silicon atoms has to be considered. The steps to follow in this analysis [20] are:

- considering the deposited energy of electrons in Silicon (Fig. 3.6), it is calculated the lepton energy that deposits a certain energy in the sensitive volume;
- with that energy it is calculated the relativistic electron Rutherford cross-section (Fig. 4.28);
- it is made the convolution of the relativistic Rutherford cross-section with the Weibull fit from the analysis.

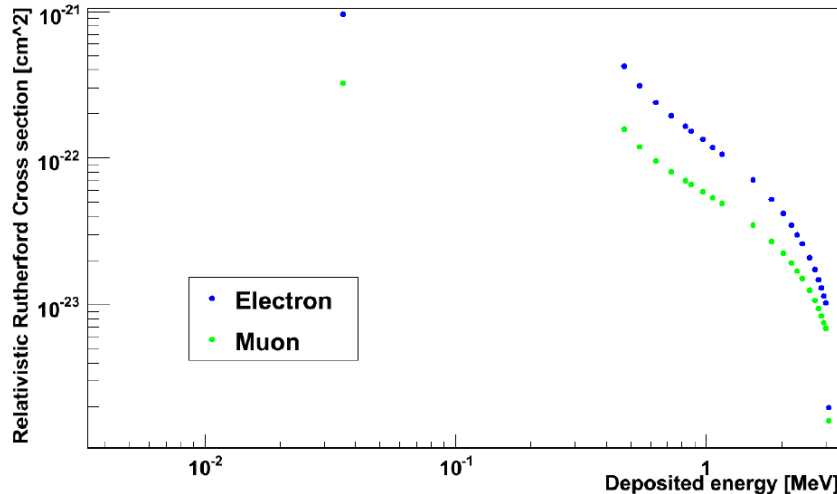


Figure 4.28: Relativistic Rutherford cross section for electrons and muons as a function of the deposited energy in $1 \mu\text{m}^3$ of Silicon. [20]

In Table 4.15 are reported the lepton fluxes obtained from simulation of [20].

Lepton [hit/(cm ² s)]	
$\bar{p} - p$	$\bar{p} - Au$
$4 \cdot 10^4$	$4 \cdot 10^5$

Table 4.15: Lepton fluxes foreseen for the $\bar{p} - p$ and the $\bar{p} - Au$ interactions ($2 \cdot 10^7$ int/sec)

As before, the estimated SEU rate are reported in Table 4.16 for the two interaction. They are negligible with respect to the hadron contributions.

November			
	ToPix 3.0		GBLD
Interaction	Configuration Register	Data Register	I2C Register
$\bar{p} - p$	$1.19 \cdot 10^{-15}$	$2.15 \cdot 10^{-16}$	$3.62 \cdot 10^{-18}$
$\bar{p} - Au$	$1.19 \cdot 10^{-14}$	$2.15 \cdot 10^{-15}$	$3.62 \cdot 10^{-17}$

February		
	GBLD_v4	GBLD_v5
Interaction	I2C Register	I2C Register
$\bar{p} - p$	$2.64 \cdot 10^{-17}$	$3.46 \cdot 10^{-18}$
$\bar{p} - Au$	$2.64 \cdot 10^{-16}$	$3.46 \cdot 10^{-17}$

Table 4.16: SEU [cm² bit⁻¹]. *Top*: ToPix and GBLD prototypes from November's test. *Bottom*: GBLD prototypes form February's test.

Chapter 5

Neutron Irradiation

In a high luminosity environment like PANDA, the radiation damage is one of the main problems that can cause a worsening of the detector performance. In this chapter the attention will be focused on its effects on the silicon bulk.

5.1 Radiation Damage in Silicon

5.1.1 Basic processes

Hadrons and energetic leptons can create in the silicon bulk a Frenkel pair composed by a silicon interstitial and a vacancy in the crystal lattice. These effects are single displacements that can be generated by neutrons and electrons with energy above 175 eV and 260 keV respectively. The energy recoil, above this energy threshold, will create point defects and defect clusters (dense agglomerations of defects). Depending on their concentration, on the energy level and on the electron and hole capture cross-section, they can cause several effects on the detector performance involving problems like an increased leakage current, the change of the effective doping concentration and the bias sensor voltage variation.

5.1.2 NIEL hypothesis

Analysis in the semiconductor device exposed to high radiation levels can be performed using the Non-Ionizing Energy Loss (NIEL) hypothesis. According to it the non-ionizing component of the total energy deposit contributes to create permanent damages.

The displacement damage cross section D is analyzed as evaluation of the non-ionizing component. For a given flux of particles Φ :

$$D \text{ [MeV mb]} = \frac{\int_E \frac{d\Phi(E)}{dE} D(E) dE}{\int_E \frac{d\Phi(E)}{dE} dE} = \frac{\int_E \frac{d\Phi(E)}{dE} D(E) dE}{\Phi_{tot}}$$

where $D(E)$ is the damage function (macroscopic interaction cross-section):

$$D(E) = \sum_k \sigma_k(E) \int f_k(E, E_r) P(E_r) dE_r$$

- E , energy of the incident particle;
- $\sigma_k(E)$, the cross-section for the k reaction;
- $f_k(E, E_r)$, the probability for an incident particle with energy E to produce a recoil of energy E_r in the k reaction;
- $P(E_r)$, the part of the recoil energy E_r deposited in displacement.

The displacement damage function for neutrons in silicon is shown in Fig. 5.1.

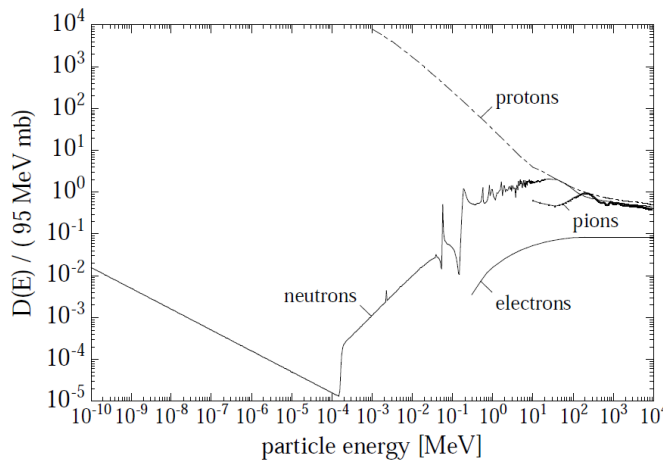


Figure 5.1: Displacement damage functions for neutrons, protons, pions and electrons [23]

The D value depends on the particle type and energy. The displacement damage cross-section for 1 MeV neutrons is set, as normalizing value, to be 95 MeV mb. The *hardness factor* K is introduced in order to describe the damage efficiency of any particle with a given kinetic energy:

$$K = \frac{D}{95[\text{MeV mb}]} = \frac{\int_E \frac{d\Phi(E)}{dE} K(E) dE}{\Phi_{tot}} \quad \text{with} \quad K(E) = \frac{D(E)}{95[\text{MeV mb}]}$$

It allows to compare and add fluencies of different particle types and energies. At the end, a 1 MeV neutron equivalent fluence can replace a real particle fluence:

$$\Phi_{1\text{MeV eq}} = K \cdot \Phi_{\text{real fluence}}$$

5.1.3 Effects on detector's properties

The main mechanisms of the defect effects are (Fig.5.2):

- a *Generation*, they act as generation centers for e-h pairs;

- b *Recombination*, they capture an e-h pairs;
- c *Compensation*, they compensate the doping effect acting as acceptors or donors;
- d *Trapping*, they catch charge carriers to re-emit them a short time later.

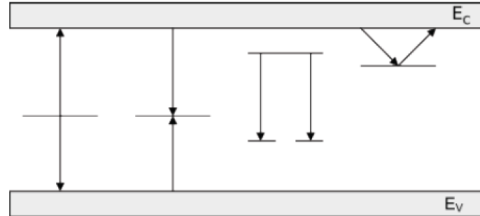


Figure 5.2: Defect effects in the band gap on electrical properties. From the left: *Generation, Recombination, Compensation and Trapping*

The changes that these processes induce in the detector's macroscopic properties are:

- a **leakage current**, the reverse current is involved if the generation centers occur in the middle of the energy gap; the change of the reverse current ΔI , normalised on the sensitive volume V , is proportional to the equivalent fluence Φ_{eq} .

$$\Delta I = \alpha \Phi_{eq} V$$

where α is the current damage parameter.

- b **depletion voltage**, the recombination can cause the dopants removal or can ionize donors (acceptors) and create positive (negative) space charge. Since the depletion voltage is proportional to the doping concentration, a change of them can cause a change on the full depletion voltage.
- c **doping type**, the phenomenon of the type inversion can occur. There is a transition from n-doped material to p-doped material. It depends on the material and the irradiation type.
- d **charge collection efficiency**, it can be reduced when it is not possible to deplete the detector and there is a loss in sensitive volume.

The second and the third properties have been investigated by the collaboration group with studies on several diodes. The last is now under study by the collaboration through test under beam. The first, the *leakage current* property is the one investigated in this work.

5.2 Displacement Damage Analysis

The neutron equivalent fluence to the radiation expected for a pixel sensors in $\bar{\text{P}}\text{ANDA}$ in one year of exposure is $\sim 8 \cdot 10^{12} \text{ n}_{1\text{MeV eq}}$ considering $\bar{p}p$ interactions with antiprotons at 15 GeV/c momentum (duty cycle 50%) [5].

The simulation of this exposure is made by neutrons from the reactor Triga Mark II, installed at the LENA laboratory, in Pavia. Considering the ToPix prototype, two different single chip assemblies and one alone chip were irradiated in order to study the displacement damage effects:

- *Assembly F* it is composed both of the sensor and the chip. The sensor is $120\ \mu\text{m}$ thick, $100\ \mu\text{m}$ of Si and $20\ \mu\text{m}$ of Czochralski substrate. It includes the 600 pixels of $100 \times 100\ \mu\text{m}^2$ size and the 40 pixels of $300 \times 100\ \mu\text{m}^2$ size. This last specific dimension is studied for the region where two readout ASICs will be arranged side by side [5].
- *Assembly E* it is composed, as the F, of the sensor and the chip. The sensor has the same dimension as before and all the 640 pixels have the $100 \times 100\ \mu\text{m}^2$ size;
- *Chip 15* it is composed only of the chip part featuring a read-out matrix of 640 cells of $100 \times 100\ \mu\text{m}^2$.

Following the expected fluence for the environment:

- *Assembly F* was irradiated with $\sim 1.5 \cdot 10^{14}\ \text{n}_{1\text{MeV eq}}$. This can simulate ~ 19 years of activity of $\bar{\text{p}}\text{p}$ interactions;
- *Assembly E* and *Chip 15* were irradiated with $\sim 1.5 \cdot 10^{13}\ \text{n}_{1\text{MeV eq}}$, to simulate ~ 2 years of activity of $\bar{\text{p}}\text{p}$ interactions.

5.2.1 Baseline calibration

The measurement involving these single chip assemblies (*F* and *E*) and the chip (15) is the baseline calibration. The analysis is made with the s-curve method. As shown in the previous chapter the signal from the detector is sent to a discriminator. There, it is compared with a voltage threshold. If the signal is bigger than the threshold, the discriminator output is '1', otherwise, it is '0' (Fig.5.3).

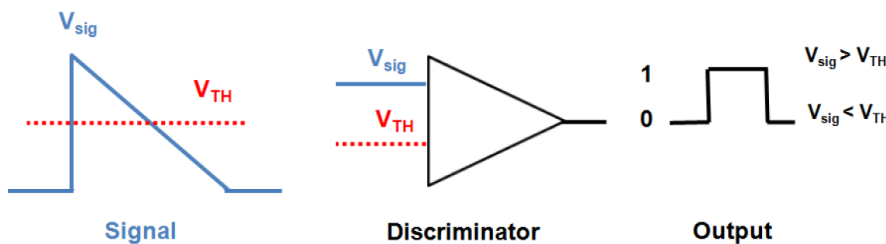


Figure 5.3: Example of a signal with a threshold, a discriminator and the output signal.

The s-curve method considers the ratio between the number of the discriminator's outputs N_C and the total number of signals feeding it N_T . Until the input signal voltage is higher than the threshold, the function is equal to 1, when it becomes lower, the function drops to zero. In a real situation it is not a step function but has a s-shaped curve (Fig. 5.4).

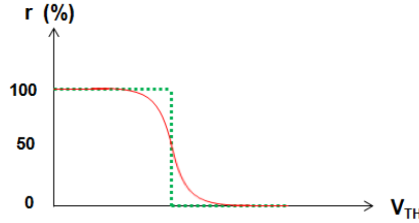


Figure 5.4: Example of $r = N_C/N_T$ with respect to the threshold.

In each pixel there is a 5-bit DAC in order to allow a fine tuning of the threshold separately. All the voltages used are negative, in this work is considered the absolute nominal value of the baseline: 700 mV. Each pixel undergoes to fluctuations of this value and it needs a correction. This can be performed with the LabView software developed by R. Wheadeon, INFN of Turin (Fig.5.5).

The threshold scan around the nominal value is performed in the voltage range from 650 mV

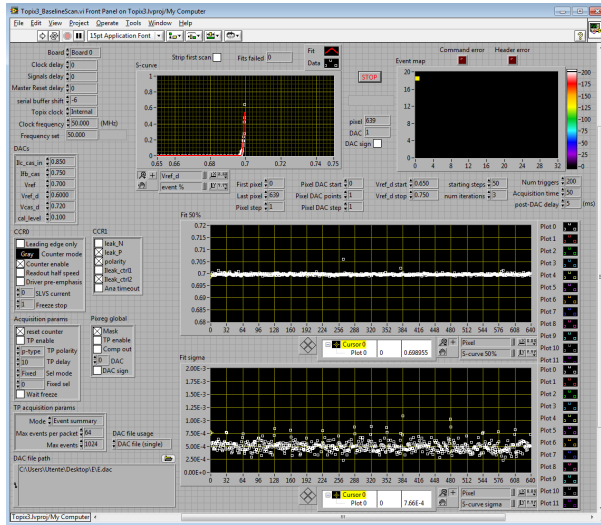


Figure 5.5: Example of the user interface for the baseline scan.

to 750 mv. The 5-bits DAC allows a 31 values selection and, then, 31 s-curves measurements for each pixel. For all the 640 pixels it is chosen the best correction. For a specific pixel it corresponds to the 50% of the tailslope of the s-curve that is closer to 700 mV and defines the best value of the DAC to be used. This test has been made for all the available assemblies, irradiated and not, with 10 V of bias voltage applied to the sensor. In Fig.5.6 the baseline distribution before (left) and after (right) the calibration are reported. The measurements concern three assemblies not previously irradiated.

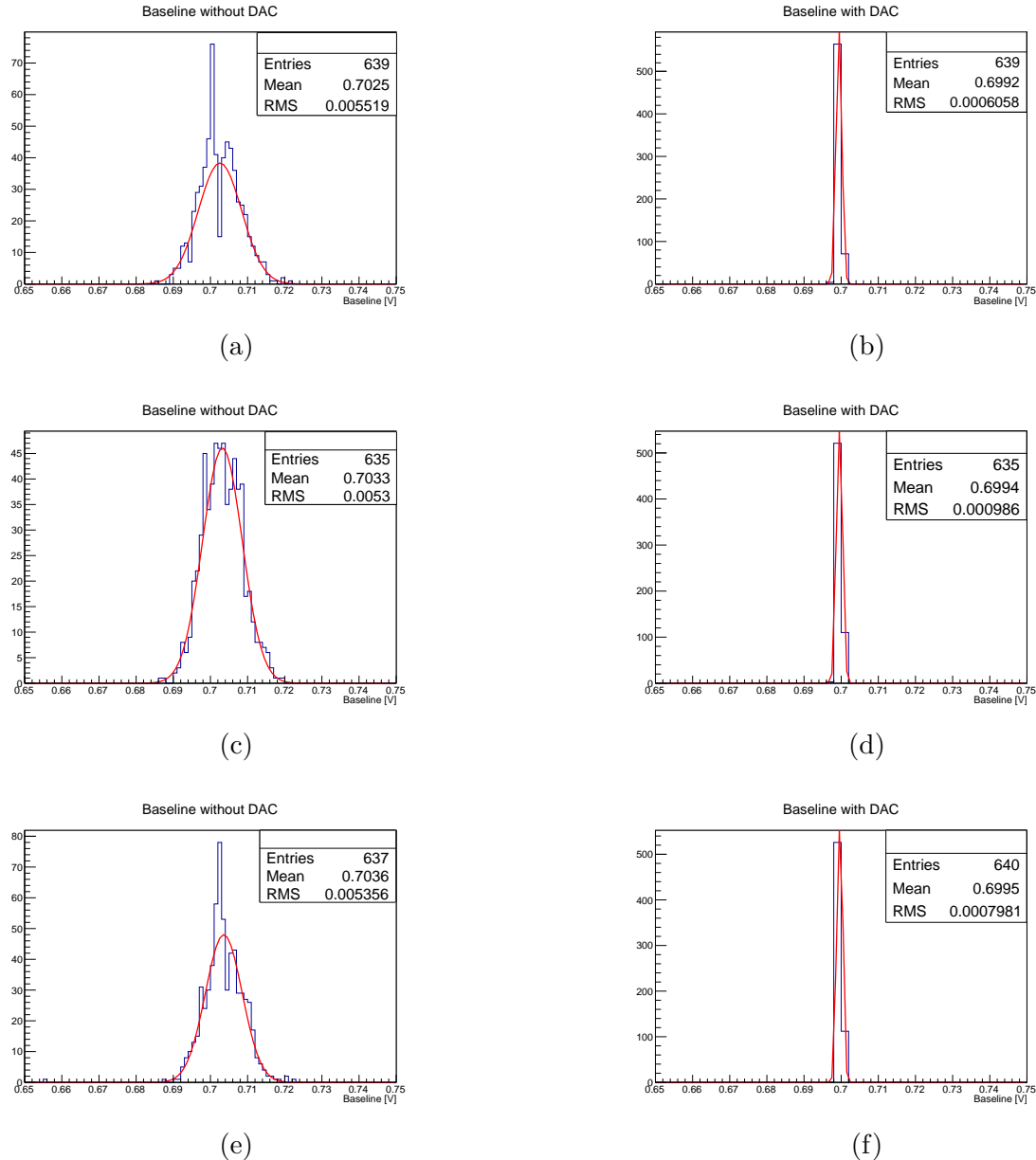


Figure 5.6: Baseline distribution for three different assemblies: **A**, (a) and (b); **H**, (c) and (d); **G**, (e) and (f). *Left:* Distribution without DAC correction; *Right:* Distribution with DAC correction.

The evaluation of the mean and the sigma of these distributions confirms the effectiveness of the correction DAC and reduces the threshold dispersion (the sigma corresponds to an equivalent charge dispersion lower than 60 e^-). In the Fig.5.7 are shown the baseline distributions for the irradiated single chip assembly F and E and for the chip (Table 5.1).

The distributions of the corrected baseline are still acceptable being the worst RMS obtained in the case of the assembly previously irradiate at ~ 19 years of PANDA experiment. The baseline correction of the chip is perfectly compatible with the results obtained for the chip not irradiated.

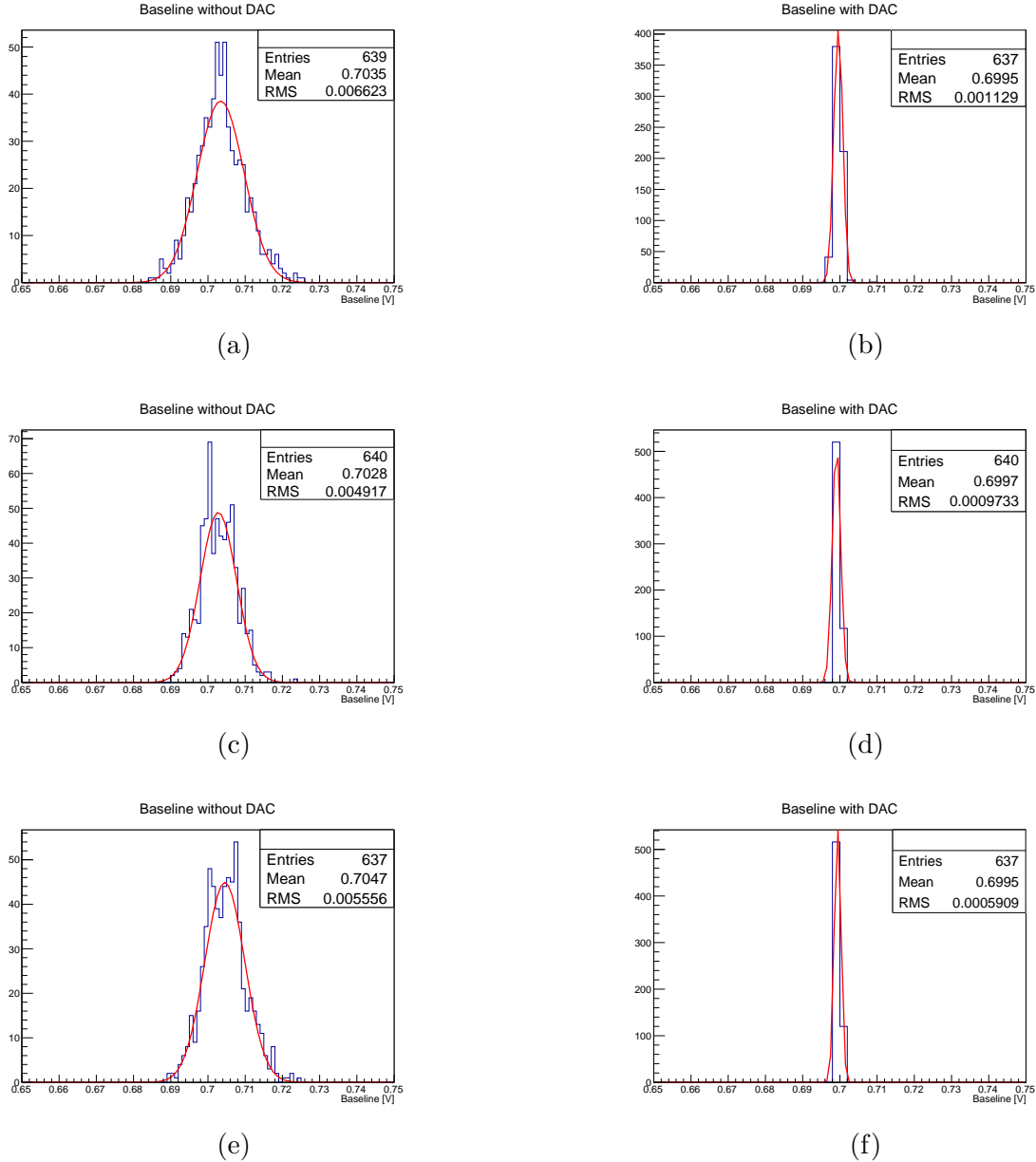
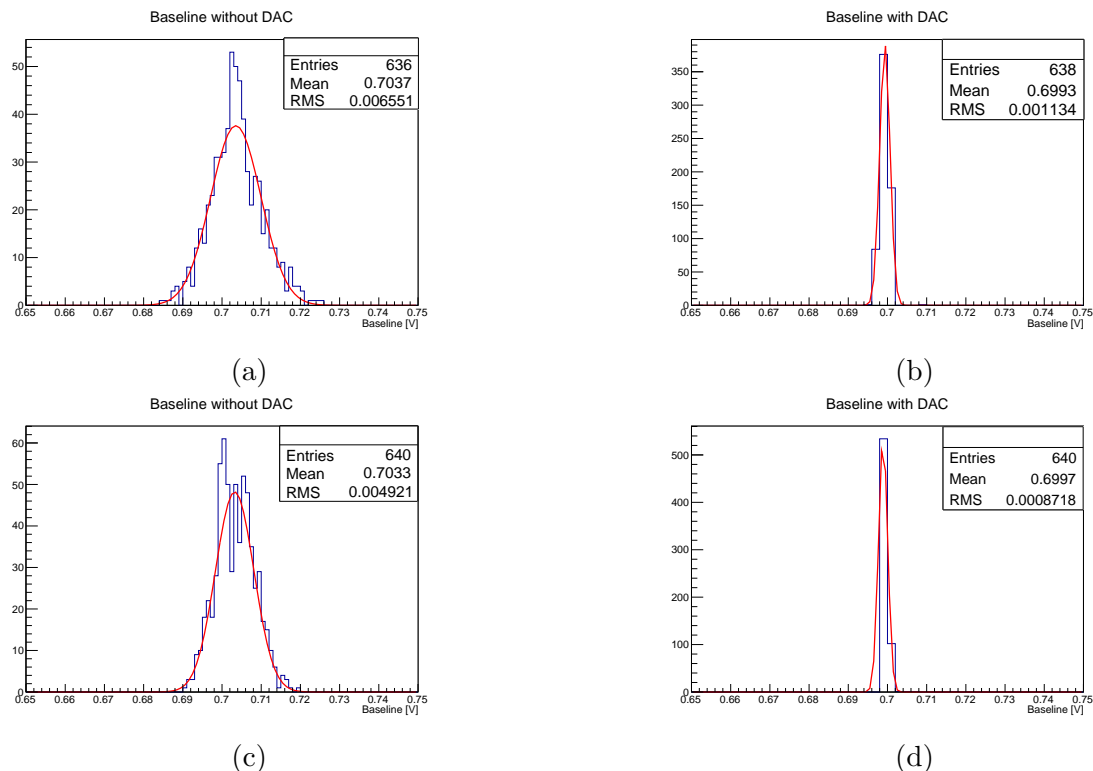


Figure 5.7: Baseline distribution for the irradiated assemblies and chip: **F**, (a) and (b); **E**, (c) and (d); **chip**, (e) and (f). *Left:* Distribution without DAC correction; *Right:* Distribution with DAC correction.

In addition, a new baseline correction analysis is made for the *F assembly* at 350 V bias voltage applied to the sensor. This is a voltage at which the full depletion is made as previously evaluated with diodes. Fig.5.8a and Fig.5.8b show the new baseline distribution. The obtained values shown in the Table 5.2 are equal to the previous evaluated values. The new baseline correction for the *E assembly* is made with a bias voltage of 250 V (Fig.5.8c, Fig.5.8d and Table 5.2), which is larger than the full depletion voltage, already evaluated with diodes. No difference occurs with respect to the previous analysis at 10 V.

Device	Baseline Distribution			
	Without DAC correction		With DAC correction	
Not irradiated	Mean [V]	Sigma [V]	Mean [V]	Sigma [V]
A	0.703	0.006	0.6992	0.0006
H	0.703	0.005	0.6994	0.0009
G	0.704	0.005	0.6995	0.0008
Irradiated	Mean [V]	Sigma [V]	Mean [V]	Sigma [V]
F	0.704	0.007	0.699	0.001
E	0.703	0.005	0.6997	0.0009
chip	0.702	0.006	0.6995	0.0006

Table 5.1: Summary of the mean and sigma value.

Figure 5.8: New Baseline distribution for board **F**, (a) and (b), and **E**, (c) and (d). *Left:* Distribution without DAC correction; *Rigth:* Distribution with DAC correction.

Device	Baseline Distribution			
	Without DAC correction		With DAC correction	
Irradiated	Mean [V]	Sigma [V]	Mean [V]	Sigma [V]
F	0.704	0.007	0.699	0.001
E	0.703	0.005	0.6997	0.0008

Table 5.2: New mean and sigma value for the baseline correction of the boards **E** and **F**.

5.2.2 Leakage currents

The bulk properties are the mostly affected characteristics such as the leakage current and the full depletion voltage. In this paragraph a first investigation of the leakage current variation for the irradiated assemblies is done.

Board F The measurement of the leakage current as a function of the bias voltage is reported in Fig.5.9. The error on the current measurement is due to the instrumental resolution: $0.01 \mu\text{A}$.

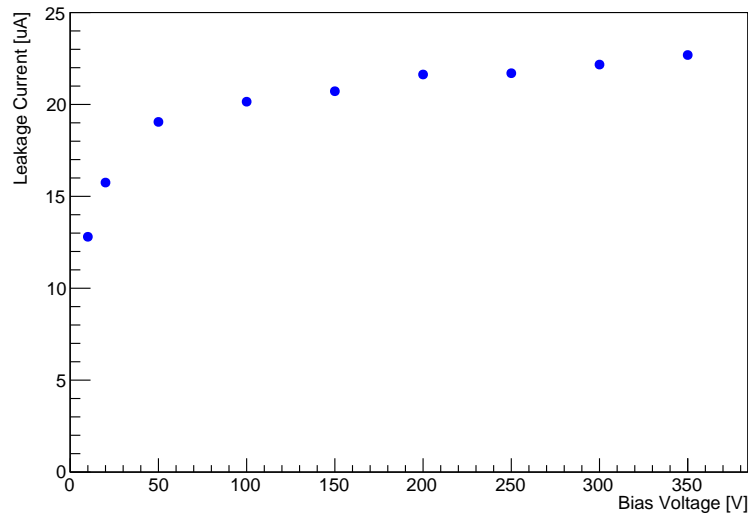


Figure 5.9: Leakage current with respect to bias voltage applied to the sensor F

The explanation to this behaviour concerns the leakage current circuit.

As explained, the readout cell of each pixel includes a circuit to compensate the leakage current of the sensor. In particular ToPix 3.0 is able to compensate a maximum of 50 nA . Taking into account the leakage current measured for the sensor of the *F assembly* at a bias voltage of 350V (higher than the full depletion voltage) it is possible to evaluate the currents for each pixel. Since the device has the composition of the $100 \cdot 100 \mu\text{m}^2$ and the $300 \cdot 100 \mu\text{m}^2$ pixels, the absorbed current for each of them will be calculated. For a total absorbed current of $22.69 \mu\text{A}$, for the $100 \cdot 100 \mu\text{m}^2$ pixels the current is $\sim 32 \text{ nA}$, but for the larger area pixel, the current absorbed is more: $\sim 95 \text{ nA}$. In the first case, the leakage current circuit is able to sustain the value. In the second one, the current overcomes the capability of this circuit to handle with a finally increased noise.

Board E A measurement of the leakage current as a function of the bias sensor has been done also for the *assembly E*. A depletion voltage scan is made also for this single chip assembly. In Fig.5.10 is shown the absorbed current with respect to the sensor applied voltage. Also in this case, the error on the current measurement is due to the instrumental resolution: $0.01 \mu\text{A}$.

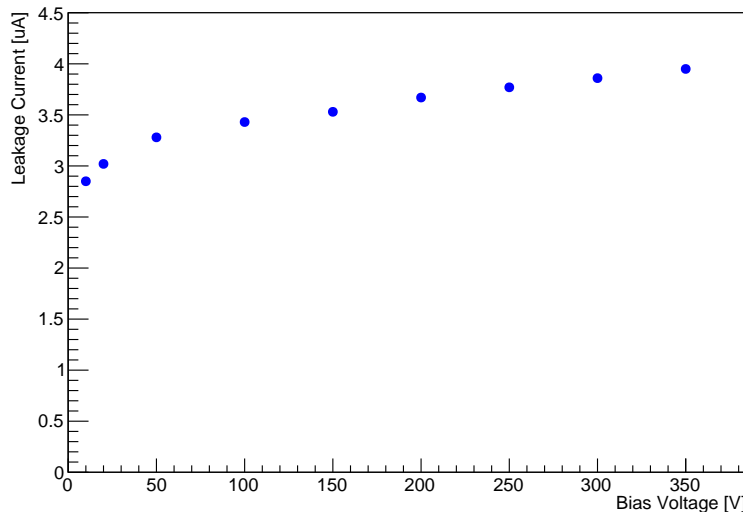


Figure 5.10: Leakage current with respect to bias voltage of sensor E

The variation of the leakage current is not significative as before. In the voltage range studied there is a difference of only one μA . In the previous analysis, instead, the current changes of about ten μA .

The total leakage current at 250 V of bias voltage is $3.77 \mu\text{A}$. Since the device is composed of 640 pixels of the same size ($100 \cdot 100 \mu\text{m}^2$) the leakage current is 5.9 nA each, completely controlled by the leakage current circuit of the readout ASIC.

5.3 Conclusions

The results of the leakage current circuit analyses with device irradiated with neutrons show that the dimension of the pixels are relevant. Until the sensor is made by the $100 \times 100 \mu\text{m}^2$ pixels, the leakage current circuit of each chip controls the current up to ~ 19 years of PANDA lifetime. The $300 \times 100 \mu\text{m}^2$ pixels start to create some problems because of the high leakage current as evaluated in the case of the *F assembly*. Dimensions lower than $300 \mu\text{m}$ will be investigated. Additional tests at lower neutron fluence value corresponding to realistic MVD lifetime are planned.

Chapter 6

Conclusions

In the $\bar{\text{P}}\text{ANDA}$ experiment the digital circuitry needs to be protected from radiation effects. *Single Event Upset* and *neutron irradiation* have been investigated in this work. Concerning the first, the tests performed at the SIRAD irradiation facility allow to know that all the registers with a tolerant architecture to SEU are able to identify the majority of errors and correct them. The obtained SEU cross section for the ToPix prototype allows to evaluate the expected SEU for the configuration and the data registers of the final ToPix. In particular, this ASIC will be placed in the sensitive region of the MVD where the higher radiation level is foreseen. The expected SEU rate by hadrons is of the order of 10^{-5} and 10^{-10} for the configuration and data registers respectively, while the leptons contribution is negligible.

The neutron irradiation has been performed on chip prototype and on single chip assemblies. Baseline measurements and their corrections are similar to the ones for the chip not irradiated. Measurements of the leakage circuits of the single chip assemblies previously irradiated at two different neutron's fluences were performed. The leakage currents calculated for the $100 \times 100 \mu\text{m}^2$ cells are lower than the maximum value accepted by the leakage current circuit of ToPix. In the case of the periferal cells the leakage current is too high to be handled by the readout cell, in the case of the higher neutron fluence, even if the irradiation value corresponding to ~ 19 years of $\bar{\text{P}}\text{ANDA}$ lifetime is much longer than the MVD lifetime.

A fourth version of ToPix has already been developed and will be tested in the next months. It presents the following SEU tolerance architecture: in the *configuration register* there are the triple modular redundancy and the Hamming encoding with self correction with D-type Flip-Flops; in the *data register* there is the DICE scheme with latches.

A new prototype for the GBLD laser driver will be studied in the next months, in particular, for what concerns the reset circuit.

At the end, the single chip assemblies presented in this work have also been tested under beam and further studies will be done in the near future.

Bibliography

- [1] *PANDA* Collaboration, *Letter of Intent for: PANDA - Strong Interaction Studies with Antiprotons*, 2004; <http://www-panda.gsi.de>
- [2] *PANDA* Collaboration, *Technical Progress Report*, 2005; <http://www-panda.gsi.de>
- [3] G.Rosner, *The FAIR facility*, Contibution to the LEAP13 Conference, this volume
- [4] *PANDA* Collaboration, *Physics Performance Report for: PANDA - Strong Interaction Studies with Antiprotons*, 2009; arXiv:0903.3905v1
- [5] *PANDA* Collaboration, *Technical Design Report for the PANDA Micro Vertex Detector: Strong Interaction Studies with Antiprotons*, 2011; <http://www-panda.gsi.de>
- [6] *PANDA* Web Site: <http://www-panda.gsi.de/>, 2013.
- [7] R.W.Novotny, *The Electromagnetic Calorimetry of the PANDA detector at FAIR*, CALOR2012, IOP Publishing, Journal of Physics: Conference Series, 404 (2012), 012063, doi: 10.1088/1742-6596/160/1/012021
- [8] A. Sanchez Lorente et al., *Detector developments for the hypernuclear programme at PANDA*, 2011, arXiv:1105.0199v1
- [9] <http://portal.kph.uni-mainz.de/panda-paluma/index.php/luminostiy-monitor.html>
- [10] <http://pdg.lbl.gov/2009/reviews/rpp2009-rev-passage-particles-matter.pdf>
- [11] National Institute of Standards and Technology (NIST),
<http://physics.nist.gov/PhysRefData/Star/Text/contents.html>
- [12] http://en.wikipedia.org/wiki/Bragg_peak
- [13] M. Dentan, *Radiation Effects on Electronic Components and Circuits*, CERN Training April 11, 2000
- [14] M. Huhtinen, F. Faccio, *Computational method to estimate Single Event Upset rates in an accelerator enviroment*, Nucl. Intrum. Methos A 450 (2000) 155-172
- [15] Ziegler et al, *The stopping and range of ions in matter*, New York Pergamon 1996,
www.SRIM.org

- [16] A. Candelori et al., *The SIRAD irradiation facility for bulk damage and Single Event Effects studies*, Proceeding of the 2ND SIRAD Workshop, LNL-INFN (REP) - 203/2004
- [17] M. Haghi and J. Draper, *The 90 nm Double-DICE storage element to reduce Single-Event upsets*, 2009.
- [18] G Mazza et al, *Single-event upset tests on the readout electronics for the pixel detectors of the PANDA experiment*, 2014. JINST 9 C01042. doi:10.1088/1748-0221/9/01/C01042
- [19] http://en.wikipedia.org/wiki/Triple_modular_redundancy
- [20] L. Zotti, *Radiation effects on the \bar{P} ANDA MVD*, 2008/2009
- [21] G. Mazza, *GBT Project; GBLD SPECIFICATIONS. Draft Release 4.0*, 2012
- [22] G. Mazza, *GBLD v5. Draft Release 1.0*, 2013
- [23] G. Lindström, M. Moll, E. Fretwurst, *Radiation hardness of silicon detectors – A challenge from high-energy physics*, Nuclear Instruments and Methods in Physics Research Section A: Accelerators, Spectrometers, Detectors and Associated Equipment Volume 426, Issue 1, 21 April 1999, pp. 1.
- [24] http://en.wikipedia.org/wiki/Gray_code

Ringraziamenti

Il primo ringraziamento, più importante, al mio papà. Grazie per esserci sempre stato e per averlo fatto con le parole giuste in ogni situazione.

Un mega ringraziamento a mia sorella. Hai fatto la tua parte anche dall'estero.

Un ringraziamento speciale a tutti gli altri famigliari. Grazie per esservi presi cura di me in questi anni.

Un ringraziamento particolare a Giulio. Sempre presente, ti sei sempre preoccupato di farmi stare tranquilla. Grazie.

Un ringraziamento sentito alla Prof.ssa Michela Greco. Con il suo sostegno e la sua pazienza mi ha permesso di raggiungere entrambi i traguardi universitari. Percorsi difficili ma entrambi soddisfacenti.

Un ringraziamento sincero alla Dott.ssa Daniela Calvo. Grazie per avermi sempre seguito nel lavoro e soprattutto grazie per tutte le opportunità che mi ha concesso.

Un ringraziamento anche al Laboratorio di Elettronica dell'INFN e a Gianni Mazza per la pazienza dimostrata nei miei confronti.

Un ringraziamento non trascurabile a Laura, Alberto e Valentino. Per aver condiviso questi momenti di lavoro e preparazione della tesi.

Un super ringraziamento, ultimo solo perchè siete tanti, a tutti i miei amici. Ai "fisici" per aver condiviso con me mattine, pomeriggi e serate, di studio e ansia, ma anche di divertimento. Ai "fuoristradisti" per avermi permesso di distrarmi dall'ansia degli esami e della tesi. A tutti gli altri, per esserci stati e avermi fatto passare bellissimi momenti. Tra tutti questi un particolare ringraziamento a tutti quelli che ho costretto a farmi da babysitter, primi tra tutti, la Sara e Frank: mi avete davvero aiutato.

Un super mega importante ringraziamento ai miei coinvilini, Palbi, la Ceci e Veso. Per avermi sempre permesso, alla fine di ogni giornata, di tornare a Casa, con la C maiuscola.